

Fuel Cells and Solid State Chemistry Division  
Risø National Laboratory of Sustainable Energy  
Technical University of Denmark - DTU  
February 2010

---

# NO Conversion Electrocatalysts

Ph.D. Thesis

---

Rebecka Maria Larsen Werchmeister



## Abstract

The objective of this study is to locate new selective electrode materials for the reduction of NO, and to gain a better understanding of the processes involved in reduction and oxidation of NO. A variety of electrodes based on mixed conducting perovskites and oxide ion conducting electrolytes of doped ceria ( $\text{CeO}_2$ ) was tested as electrode materials.

Symmetrical cells and three electrode cells with composite electrodes of  $(\text{La}_{1-x}\text{Sr}_x)_s\text{-MnO}_3$  (LSM) ( $x=0.15, 0.5$  and  $s = 0.9, 0.99$ ),  $\text{La}_{1-y}\text{Sr}_y\text{Co}_{1-z}\text{Fe}_z\text{O}_3$  ( $y = 0.25, 0.4$  and  $z = 1$  (LSF),  $0.8$  (LSCF)) and ceria doped with Gd or Pr were prepared.

Using three electrode cells with composite electrodes it was possible to observe NO reduction at  $600^\circ\text{C}$  when the electrodes were polarised to  $-0.6\text{ V}$  vs Pt/air or lower. The electrode with LSM15 and  $\text{Ce}_{0.9}\text{Gd}_{0.1}\text{O}_2$  (CGO10) had the highest activity, while the LSM50 and  $\text{Ce}_{0.8}\text{Pr}_{0.2}\text{O}_2$  (CPO20) electrode had the highest current efficiency (CE). Cyclic voltammetry measurements showed that the LSM50/CPO20 had the best selectivity for NO in the temperature range  $300$  to  $400^\circ\text{C}$ .

Technological investigations were performed using porous cell stacks with 13 layers (= 6 cells) made from laminated tapes of electrolyte (CGO10) and LSM and doped ceria based composite electrodes. The electrodes were infiltrated with pure ceria, CGO10 or CPO20. Gas conversion was observed when the cell stack was polarised with  $4.5\text{ V}$ . The infiltration with pure ceria gave the highest activity, while the highest CE was seen for infiltration with CGO10. NO conversion could be detected at temperatures as low as  $250^\circ\text{C}$  for the best cell stack. For each infiltration approximately  $8\text{ mg/cm}^2$  ceria was infiltrated, and multiple infiltrations increased the activity. The cell stacks with LSM50/CPO10 electrodes had the highest activity, while the LSM15/CGO10 electrodes had the highest CE. Thus the results did not correspond well with the measurements on three electrode cells and symmetrical cells, apparently the infiltration changed the surface chemistry of the electrodes.  $\text{N}_2$  and  $\text{O}_2$  was formed in stoichiometric amounts at polarisation at  $400^\circ\text{C}$ , but at lower temperatures too small amounts were formed, especially  $\text{O}_2$ , indicating formation  $\text{NO}_2$  instead of reduction of NO.

The symmetrical cells were characterised with electrochemical impedance spectroscopy (EIS). Generally the electrodes had higher polarisation resistance ( $R_p$ ) in an NO containing atmosphere than in air at high temperature ( $600^\circ\text{C}$ ), while at lower temperature ( $300$  to  $400^\circ\text{C}$ ) the  $R_p$  was largest for electrodes in air, i.e. the activation energy being lower for electrodes in  $1\%$  NO in Ar than in air.

For the series of electrodes with LSM, the electrodes with LSM50/CPO20 had the lowest  $R_p$  values, but still all the electrodes based on LSF and LSCF were better oxygen electrodes, especially at  $600^\circ\text{C}$ .

The impedance spectra of electrodes in NO at open circuit voltage (OCV) were dominated by a large low frequency arc, especially at high temperatures. This arc was a type of conversion arc. The arc appeared because the electrodes did not react directly electrochemically with NO around OCV, but with an intermediate (likely  $\text{NO}_2$ ) present in low concentration. This intermediate was formed catalytically by the electrodes.

EIS measurements of the polarised three electrode cells showed that the kinetics in

NO containing atmosphere changes at polarisation of -0.6 V vs air/Pt or lower.

## Resume

Formålet med dette studie var at finde nye selektive elektrode materialer til reduktion af NO og at få større indsigt i processerne involveret i reduktion og oxidation af NO. Et udvalg af elektroder baseret på blandede ledere med perovskitstruktur og ionledende elektrolytter af dopet ceria ( $\text{CeO}_2$ ) blev testet som elektrode materialer. Symmetriske celler og tre elektrode celler med komposit elektroder af  $(\text{La}_{1-x}\text{Sr}_x)_s\text{MnO}_3$  (LSM) ( $x=0,15, 0,5$  og  $s = 0,9, 0,99$ ),  $\text{La}_{1-y}\text{Sr}_y\text{Co}_{1-z}\text{Fe}_z\text{O}_3$  ( $y = 0,25, 0,4$  og  $z = 1$  (LSF),  $0,8$  (LSCF)) og ceria dopet med Gd eller Pr blev fremstillet.

Ved brug af tre-elektrode celler med komposit elektroder var det muligt at detektere reduktion af NO ved  $600^\circ\text{C}$ , når elektroderne var polariseret med  $-0,6\text{ V}$  vs Pt/luft eller lavere. Elektroden med LSM15 og  $\text{Ce}_{0,9}\text{Gd}_{0,1}\text{O}_2$  (CGO10) var den mest aktive, mens elektroden med LSM50 og  $\text{Ce}_{0,8}\text{Pr}_{0,2}\text{O}_2$  (CPO20) havde det højeste strømudbytte. Målinger med cyklisk voltammetri viste at elektroden med LSM50/CPO20 havde den højeste selektivitet for NO i temperaturområdet  $300$  til  $400^\circ\text{C}$ .

En porøs cellestak med 13 laminerede lag (= 6 celler) af elektrolyt (CGO10) og elektrode (LSM + dopet ceria) blev brugt til teknologiske eksperimenter. Elektroderne var infiltrerede med rent ceria, CGO10 og CPO20. Gas konversion blev set, når cellestakken var polariseret med  $4,5\text{ V}$ . Den bedste aktivitet fandt sted med rent ceria infiltrering, mens CGO10 infiltrering gav det højeste strømudbytte. NO konversion kunne måles helt ned til  $250^\circ\text{C}$  for den bedste cellestak. Ca.  $8\text{ mg/cm}^{-2}$  ceria blev infiltreret per infiltrering, og cellestakke der var blevet infiltreret flere gange havde en højere aktivitet. Cellestakke med LSM50/CPO10 elektroder havde den højeste aktivitet, imens cellestakke med LSM15/CGO10 elektroder havde det højeste strømudbytte. Så disse resultater svarede ikke til resultaterne fra målinger på tre-elektrode cellerne, tilsyneladende påvirkede infiltreringerne overfladekemi for elektroderne i de porøse cellestakke.  $\text{N}_2$  og  $\text{O}_2$  blev dannet i støkiometriske mængder ved polarisation ved  $400^\circ\text{C}$ , men ved lavere temperaturer blev der dannet for små mængder af disse specier, specielt  $\text{O}_2$ , hvilket indikerede at  $\text{NO}_2$  blev dannet i stedet for  $\text{N}_2$ .

De symmetriske celler blev karakteriseret med elektrokemisk impedans spektroskopi (EIS). Generelt havde elektroderne en højere polarisations modstand ( $R_p$ ) i en atmosfære indeholdende NO, end de havde i luft ved de høje temperaturer ( $500$ - $600^\circ\text{C}$ ). Ved de lavere temperaturer ( $300$ - $400^\circ\text{C}$ ) var  $R_p$  størst for elektroder i luft, dette skyldes at aktiverings energien for  $R_p$  er betydeligt højere for elektroder i luft end i  $1\%$  NO i Ar.

LSM50/CPO20 elektroder havde de laveste  $R_p$  værdier for elektroder baseret på LSM, men elektroderne baseret på LSF og LSCF var bedre ilt elektroder, specielt ved  $600^\circ\text{C}$ .

Impedans spektre for elektroder i NO ved åben spænding var domineret af en stor lavfrekvent bue, specielt ved de høje temperaturer. Denne bue blev knyttet til konversion, og opstod fordi elektroderne ikke reagerede elektrokemisk med NO ved åben spænding, men i stedet med en intermediær (højst sandsynligt  $\text{NO}_2$ ) med lav koncentration. Denne intermediær blev dannet katalytisk af elektroderne.

EIS målinger på de polariserede tre-elektrode celler viste, at kinetikken for elektroderne i en atmosfære indeholdende NO ændredes ved  $-0,6\text{ V}$  vs Pt/luft.

## Preface

This thesis is submitted to the Technical University of Denmark to finalise the Ph.D. study *NO conversion electrocatalysts*. The work was carried out in the period 1 of March 2007 to the 28 of February 2010 in the Fuel Cells and Solid State Chemistry Division(ABF), Risø National Laboratory for Sustainable Energy, Technical University of Denmark with Research prof. Mogens Mogensen as main supervisor and scientist Kent Kammer Hansen as secondary supervisor. This work was supported financially by The Programme Commission on Sustainable Energy and Environment, The Danish Council for Strategic Research, via the Strategic Electrochemistry Research Center (SERC) ([www.serc.dk](http://www.serc.dk)), contract no. 2104-06-0011.

## Acknowledgment

I have spent the last three years in the wonderful working environment of the Fuel Cells and Solid State Chemistry Division, and that has been a great time. I have gotten much help from my many work colleagues and enjoyed some good discussions.

I would like to thank my supervisor Mogens Mogensen for his help and our many fruitful discussions during the project, and Kent Kammer Hansen for helping me with the experimental work and always taking time to answer my questions.

Finally I thank the people in the Exhaust Gas Cleaning work group. I have enjoyed the company of my office mates Frantz and Marie for our many discussion about electrochemical exhaust gas cleaning and wildlife in Denmark.

# Contents

<b>1</b>	<b>Introduction</b>	<b>1</b>
1.1	Methods for removal of $\text{NO}_x$	3
1.1.1	Direct decomposition	3
1.1.2	Selective catalytic reduction (SCR)	3
1.1.3	Nitrogen storage reduction (NSR)	4
1.1.4	Electrochemical removal of $\text{NO}_x$	4
1.2	Catalysis	7
1.2.1	Zeolites	8
1.2.2	Noble metals	8
1.2.3	Metal oxides	8
1.2.4	Addition of compounds to increase activity	11
1.2.5	Kinetics	11
1.3	Materials	13
1.4	Characterisation of materials	15
1.5	Electrochemical characterisation	17
1.6	Measurement of gas composition	19
<b>2</b>	<b>Experimental</b>	<b>21</b>
2.0.1	Glycine nitrate combustion synthesis	21
2.1	Experimental setups	21
2.1.1	XANES setup	21
2.1.2	Electrochemical setups	22
<b>3</b>	<b>Characterisation of <math>\text{Ce}_{1-x}\text{Pr}_x\text{O}_{2-\delta}</math></b>	<b>27</b>
3.1	Introduction	27
3.2	Experimental	27
3.3	Results	29
3.3.1	Cone measurements	29
3.3.2	XANES	31
3.4	Discussion	33
3.4.1	Surface reactions	33
3.4.2	Selectivity	33
<b>4</b>	<b>LSM and ceria doped symmetrical cells</b>	<b>35</b>
4.1	Introduction	36
4.2	Experimental	37

4.3	Results . . . . .	39
4.3.1	Micro structure . . . . .	39
4.3.2	Data treatment . . . . .	40
4.3.3	Air . . . . .	43
4.3.4	NO . . . . .	44
4.3.5	NO <sub>2</sub> . . . . .	44
4.3.6	N <sub>2</sub> O . . . . .	46
4.3.7	NO + O <sub>2</sub> . . . . .	47
4.4	Discussion . . . . .	48
4.4.1	Matching of arcs to processes . . . . .	48
4.4.2	Temperature dependence . . . . .	51
4.4.3	Addition of oxygen . . . . .	52
4.4.4	Doping with Pr . . . . .	52
4.5	Conclusion . . . . .	53
4.5.1	Acknowledgments . . . . .	54
<b>5</b>	<b>LSM and doped ceria electrodes for NO removal</b>	<b>55</b>
5.1	Introduction . . . . .	55
5.2	Experimental . . . . .	57
5.2.1	Three electrode setup . . . . .	58
5.2.2	Electrochemical techniques . . . . .	59
5.3	Results . . . . .	59
5.3.1	OCV . . . . .	59
5.3.2	EIS and equivalent circuits . . . . .	59
5.3.3	Cyclic voltammetry . . . . .	62
5.3.4	Polarisation of electrodes . . . . .	62
5.3.5	EIS under polarisation . . . . .	65
5.4	Discussion . . . . .	66
5.4.1	Reaction mechanism . . . . .	66
5.4.2	Selectivity . . . . .	68
5.5	Conclusion . . . . .	70
<b>6</b>	<b>LSF and LSCF electrodes</b>	<b>73</b>
6.1	Introduction . . . . .	73
6.2	Experimental . . . . .	73
6.3	Results . . . . .	74
6.3.1	Symmetrical cells . . . . .	74
6.3.2	Three electrode cell . . . . .	77
6.4	Discussion . . . . .	79
6.4.1	Electrode composition . . . . .	79
6.4.2	Selectivity . . . . .	80
6.4.3	Comparison with previous results . . . . .	81



<b>7</b>	<b>Porous cell stacks</b>	<b>83</b>
7.1	Introduction . . . . .	83
7.2	Experimental . . . . .	84
7.3	Results . . . . .	87
7.3.1	Characterisation of porous cell stacks . . . . .	87
7.3.2	Electrochemical results . . . . .	87
7.4	Discussion . . . . .	94
7.5	Conclusion . . . . .	97
<b>8</b>	<b>The special LSM15/CGO10 porous cell stack</b>	<b>99</b>
8.1	Introduction . . . . .	99
8.2	Experimental . . . . .	99
8.3	Results . . . . .	100
8.3.1	Microscopy . . . . .	100
8.3.2	Electrochemical results . . . . .	100
8.4	Discussion . . . . .	103
8.4.1	Comparison with later results . . . . .	103
<b>9</b>	<b>Discussion</b>	<b>105</b>
<b>10</b>	<b>Conclusion and outlook</b>	<b>109</b>
10.1	Conclusion . . . . .	109
10.2	Outlook . . . . .	110

## Objective

The objective of this work is to find new electrode materials for electrochemical removal of  $\text{NO}_x$ . Some criteria should be met for a suitable electrode material:

1. Selectivity towards NO compared to  $\text{O}_2$
2. High electrochemical activity
3. The materials should be active in the temperature range of the diesel exhaust
4. Price. A material less expensive than the noble metals presently used for the three way catalytic converter should be found
5. Chemical stability
6. Mechanical stability. The material should be capable of enduring changes in temperature and the thermal expansion coefficient of the material should be compatible with the electrolyte

Several electrochemical techniques are used for elucidating the properties of the chosen materials. It is sought to test the materials for activity and find a way of predicting the selectivity of the materials. Furthermore it is the aim to obtain a better understanding of the electrode reactions, and of the kinetics of reduction and oxidation of nitrogen oxide.

Electrode materials are characterised electrochemically to find the most promising with respect to selectivity and activity, and gain knowledge about the kinetics of the electrode reactions. The activity of the electrodes are tested by monitoring gas composition during polarisation.

In this study the focus is on point 1-3 of the demands listed above. The electrode materials tested are already known from solid oxide fuel cells (SOFCs), therefore point 4-6 in the list have already been covered.

## Layout of thesis

The thesis is divided into 8 chapters, where the chapter 1 describes the background of  $\text{deNO}_x$ , the choice of materials and theory behind measurements. Chapter 2 contains a description of the synthesis applied and of the experimental setups used. Chapter 3 to 8 describe and discuss the results, while chapter 9 contains a short general discussion of the results from the previous chapters. Finally chapter 10 contains the conclusion on the work together with an outlook.

**Chapter 1** An introduction and a literature study about techniques for removal of  $\text{NO}_x$  and catalyst materials for direct decomposition and electrochemical removal of NO. The theory behind the methods for characterisation is explained.

**Chapter 2** A description of the synthesis method and the experimental setups.

**Chapter 3** This chapter contains the results from the characterisation of  $\text{Ce}_{1-x}\text{Pr}_x\text{O}_{2-\delta}$  with electrochemical measurements and X-ray absorption near edge spectroscopy.

**Chapter 4** The manuscript "Characterisation of  $(\text{La}_{1-x}\text{Sr}_x)_s\text{MnO}_3$  and doped ceria composite electrodes in  $\text{NO}_x$  containing atmosphere with impedance spectroscopy", which has been accepted for publishing in Journal of Electrochemical Society.

**Chapter 5** The manuscript "Electrochemical testing of composite electrodes of  $(\text{La}_{1-x}\text{Sr}_x)_s\text{MnO}_3$  and doped ceria in NO containing atmosphere", which has been submitted to Journal of Electrochemical Society.

**Chapter 6** An account of the results from electrochemical measurements on cells with  $\text{La}_{1-x}\text{Sr}_x\text{FeO}_{3-\delta}$  and  $\text{La}_{1-x}\text{Sr}_x\text{Co}_{1-y}\text{F}_y\text{O}_{3-\delta}$ .

**Chapter 7** The manuscript "Electrochemical removal of  $\text{NO}_x$  with porous cell stacks" for submission in Applied Chemistry B: Environmental.

**Chapter 8** A summation of the results from the measurements on the special porous cell stack.

**Chapter 9** A short discussion of the results from the previous chapters.

**Chapter 10** Conclusion and outlook.

The ordering of the chapters is not chronological with respect to the experiments, the results in chapter 8 was obtained before the ones in chapter 7. Since the results in chapter 8 could not be reproduced, but only serves as a standard for what is possible with the technique, the data is represented after the newer reproducible results.

Chapter 2 only describes the experimental setups briefly, whereas the details are given in the experimental sections in chapter 3 to 8. Further chapter 3 to 8 also contains discussions of the results, and the chapters based on submitted or to be submitted manuscripts also have small conclusions.



# List of Figures

1.1	Sketch of a solid oxide electrochemical cell for removal of $\text{NO}_x$ .	5
1.2	The perovskite structure	9
1.3	The fluorite unit cell	10
1.4	Diffraction of X-rays from crystal planes.	15
1.5	Diffraction pattern of CPO20.	16
1.6	Normalised absorption energy as a function of energy for the Ce L3 peak.	17
2.1	The setup for the XANES measurements.	22
2.2	Sketch of the cone setup.	22
2.3	Sketch of the three electrode test cell.	23
2.4	Sketch of the three electrode setup.	24
3.1	Equivalents diagram used to fit the impedance data from the cone measurements.	28
3.2	OCV for the CPO10 and CPO20 cone in 1 % NO in Ar	29
3.3	Cyclic voltammogram for the CPO10 cone in air and 1 % NO in Ar	30
3.4	Ratio between $i_{\text{NO}}$ and $i_{\text{air}}$	30
3.5	Ratio between $i_{\text{NO}}$ and $i_{\text{air}}$ for the second series of measurements on the CPO20 cone	31
3.6	Cyclic voltammograms recorded after polarisation with +0.4, 0 and -0.4 V	32
3.7	XANES spectra of Pr L <sub>3</sub> edge in different atmospheres for CPO20.	32
4.1	A sketch of the symmetrical cell setup.	38
4.2	FIB-SEM image of the LSM50/CPO20 electrode and part of CGO electrolyte	40
4.3	Sketch of impedance plot of symmetrical cell with $R_p$ and $R_s$ and the corresponding equivalent circuit.	40
4.4	The impedance spectra for LSM50/CPO10 electrodes in 1% NO at 600 °C.	41
4.5	High frequency close up of impedance spectra of symmetrical cell with LSM50/CPO10 electrodes in 1 % NO in Ar at 600 °C	42
4.6	Impedance plot for LSM50/CPO10 electrodes in air at 600 °C.	42
4.7	Impedance plot for LSM15/CGO10 electrodes in 1% NO <sub>2</sub> in Ar at 600 °C.	43

4.8	The $R_{HF}$ , $R_{MF}$ and $R_{LF}$ for the LSM15/CGO10 electrodes in 1 % NO in Ar . . . . .	45
4.9	Impedance plots for LSM50/CPO20 cells in 1 % NO at 600 °C with a gas flow of 10 mL/min and 100 mL/min. . . . .	46
4.10	The impedance spectra for LSM15/CGO10 electrodes in 1% NO <sub>2</sub> in Ar at 500 °C. . . . .	46
4.11	The $R_p$ for the LSM50/CPO10 electrodes in 1 % NO in Ar, air and 0.75 % NO and 5 % O <sub>2</sub> in Ar. . . . .	47
4.12	The $R_p$ for the LSM50/CPO20 electrodes in 1 % NO in Ar, air and 0.75 % NO and 5 % O <sub>2</sub> in Ar. . . . .	48
4.13	Impedance plots for LSM50/CPO10 electrodes in 1% NO in argon at 500 °C and 600 °C with a flow of 10 mL/min. . . . .	49
4.14	The impedance plots for LSM50/CPO10 electrodes in 1 % NO in Ar at 600 °C with a flow rate of 10 mL/min. . . . .	51
4.15	Impedance spectrum for LSM50/CPO20 cells in Air, 1 % NO in Ar and 0.75 % NO + 5 % O <sub>2</sub> in Ar at 400 °C. . . . .	52
5.1	A sketch of a solid oxide electrochemical cell for removal of NO <sub>x</sub> . . . . .	56
5.2	Sketch of the three electrode setup . . . . .	58
5.3	OCV as a function of flow rate for the LSM50/CPO10 electrode in 0.1% NO in Ar at 600 °C. . . . .	60
5.4	Impedance plot for symmetrical cells with LSM15/CGO10, LSM50/CPO10 and LSM50/CPO20 electrodes in 1% NO in Ar 600 °C. . . . .	60
5.5	Impedance spectra for LSM15/CGO10 electrodes in air at 300 °C . . . . .	61
5.6	Cyclic voltammogram for LSM50/CPO10 electrodes cells in 0.1% NO in Ar at 600 °C. . . . .	62
5.7	Cyclic voltammogram for LSM50/CPO20 electrodes in air, 0.1% NO + 5% O <sub>2</sub> in Ar and 0.1% NO in Ar. . . . .	63
5.8	$i_{NO}$ as a function of temperature for electrodes of LSM15/CGO10, LSM50/CPO10 and LSM50/CPO20 in 0.1% NO in Ar at -0.6 V vs Pt/air. . . . .	63
5.9	NO conversion and CE as a function of polarisation for LSM15/CGO10 electrodes in 0.1% NO in Ar at 600 °C. . . . .	64
5.10	$R_p$ for LSM50/CPO20 electrode in 5 mL/min 0.1% NO in Ar at 600 °C. . . . .	65
5.11	$R_{LF}$ and $EC_{LF}$ for LSM50/CPO20 electrode in 5 mL/min 0.1% NO in Ar at 600 °C. . . . .	65
5.12	$R_{LF}$ and $EC_{LF}$ for LSM50/CPO20 electrode in 10 mL/min 0.1% NO in Ar at 600 °C. . . . .	66
5.13	Potential equivalent circuit diagram for impedance of cells with electrodes of LSM/CPO at 600 °C in 1% NO in Ar. . . . .	67
5.14	The ratio between $i_{NO}$ and $i_{Air}$ . . . . .	69
5.15	The ratio between $i_{NO+O_2}$ and $i_{Air}$ . . . . .	69
6.1	SEM picture of LSF40/CGO10 composite electrode on symmetrical cell. . . . .	75

6.2	Impedance spectra of LSF25/CGO10 electrode in air and 1 % NO in Ar at 600 °C . . . . .	75
6.3	Impedance spectra of LSCF40/CPO20 cell in 1 % NO in Ar at 300 °C	76
6.4	Impedance spectra of LSCF40/CGO10 cell in 1 % NO in Ar at 600 °C	77
6.5	Arrhenius plots of $R_p$ -values for electrodes in air . . . . .	77
6.6	Arrhenius plots of $R_p$ -values for electrodes in 1 % NO in Ar . . . . .	78
6.7	Cyclic voltammogram for LSCF40/CGO10 electrodes cells in 0.1% NO in Ar, 0.1% NO + 5 % $O_2$ in Ar and air at 600 °C. . . . .	78
6.8	The ratio between $R_p(\text{NO})$ and $R_p(\text{air})$ as a function of temperature for all the composite electrodes. . . . .	81
6.9	$R_p$ for composite electrodes in air . . . . .	82
7.1	Sketch of a porous cell stack. . . . .	85
7.2	Sketch of the setup for porous cell stacks. . . . .	86
7.3	SEM picture of the PCS1 cell stack with 13 layers and LSM15/CGO10 electrodes. . . . .	87
7.4	Cyclic voltammogram of a 13 layer PCS3b cell stack with and without infiltration in 0.1 % NO in Ar at 400 °C. . . . .	88
7.5	Change in NO concentration and current density during polarisation with 4.5 V on a 13 layer PCS3b cell stack infiltrated with CPO20, at 400 °C. . . . .	90
7.6	Decrease in NO concentration in percentage as a function of polarisation over a PCS3b cell stack . . . . .	91
7.7	Decrease in NO concentration in percentage and CE as a function of gas flow over a PCS3b cell stack. . . . .	92
7.8	Percentage of NO removed and CE as a function of polarisation of a PCS3b cell stack infiltrated with CPO20 five times. . . . .	92
7.9	NO concentration during three sequential polarisations with 9 V over a PCS3b cell stack. . . . .	93
7.10	Change in NO concentration during polarisation with 3 V on a PCS3b cell stack at 400 °C. . . . .	93
7.11	$t_{\frac{1}{2}}$ as a function of temperature for PCS3b cell stack. . . . .	94
8.1	Setup of porous cell in 3 electrode rig. . . . .	100
8.2	SEM micrograph of an 11-layer porous cell stack with remains of gold paste left on the sides. . . . .	101
8.3	Cyclic voltammograms with different scan rates at 400 °C in Ar with 1000 ppm NO. . . . .	101
8.4	Percentage of NO removed and CE for a cell stack polarised with 3.5 V at 400 °C in Ar with 1000 ppm NO. . . . .	102
8.5	Percentage of NO present and current density for a cell stack polarised with 3.5 V at 450 °C in Ar with 1000 ppm NO. . . . .	102
8.6	Percentage of NO removed and CE for a cell stack polarised with 3.5 V at 400 °C in Ar with 1000 ppm NO and 4 % $O_2$ . . . . .	103





# List of Tables

1.1	EU emission standards for passenger cars. . . . .	2
1.2	Elements in equivalent circuits . . . . .	18
4.1	$E_a$ for electrodes in air, 1 % NO in Ar, 1 % NO <sub>2</sub> in Ar and 0.75 % NO + 5 % O <sub>2</sub> in Ar . . . . .	44
4.2	$E_a$ values together with the corresponding $R^2$ values for the fit, EC values, $R_{MF}$ and $R_{LF}$ values at 600 °C for MF and LF arcs in 1 % NO in Ar . . . . .	45
4.3	$E_a$ values, EC and $R_{MF}$ (600 °C) for 1 % NO <sub>2</sub> in Ar . . . . .	47
5.1	The composition of the screen printed electrodes. . . . .	57
5.2	Degree of NO conversion and CE for polarisation with -0.8 V vs Pt/Air for electrodes in 0.1 % NO in Ar, 5 mL/min flow and at 600 °C. . . . .	64
6.1	The composition of the screen printed electrodes. . . . .	73
6.2	$E_a$ values for impedance arcs for electrodes in air and 1 % NO in Ar .	77
6.3	Degree of NO conversion and CE for polarisation with -0.7 and -0.9 V vs Pt/Air for LSCF40/CGO10 electrodes . . . . .	79
7.1	List of the investigated types of porous cell stacks composition and BET surface. . . . .	85
7.2	Percentage of NO removed and CE for 13 layer porous cell stacks infiltrated with pure ceria. . . . .	89
7.3	N <sub>2</sub> and O <sub>2</sub> formed and NO removed at steady state for PCS3b cell stacks. . . . .	89
7.4	Percentage of NO removed and CE for for PCS3b cell. . . . .	90

## Acronym

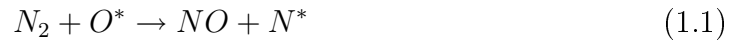
AC = Alternating Current  
ASR = Area Specific Resistance  
BET = Brunauer Emmett Teller  
CE = Current Efficiency  
CV = Cyclic Voltammetry  
EC = Equivalent Capacitance  
EIS = Electrochemical Impedance Spectroscopy  
EXAFS = Extended X-ray Absorption Fine Structure  
FCC = Face Centret Cubic  
IT-SOFC = Intermediate Temperature Solide Oxide Fuel Cells  
LNT = Lean NO<sub>x</sub> Trap  
MEIC = Mixed Ionic Electronic Conductor  
NSR = Nitrogen Storage Reduction  
OCV = Open Circuit Voltage  
RDS = Rate Determining Step  
SCR = Selective Catalytic Reduction  
SEM = Scanning Electron Microscopy  
SOFC = Solid Oxide Fuel Cell  
TWCC = Three Way Catalytic Converter  
TPB = Triple Phase Boundary  
YSZ = Yttria Stabilised Zirconia  
XANES = X-ray Adsorption Near Edge Spectroscopy  
XRD = X-ray diffraction  
ZSM = Zeolite Socony Mobil

# Chapter 1

## Introduction

Nitrogen oxides ( $\text{NO}_x$ ,  $x = 1, 2$ ) are formed from  $\text{O}_2$  and  $\text{N}_2$  in combustion engines at high temperatures. The term nitrogen oxide covers many different molecules consisting of nitrogen and oxygen atoms, as nitrogen can have several different oxidation states in these compounds, +1, +2, +3 and +4. Nitrogen can also have the oxidation state of +5 in the ionic compound  $\text{NO}_3^-$ . The most common nitrogen oxide compounds are NO (nitric oxide),  $\text{NO}_2$  (nitrogen dioxide) and  $\text{N}_2\text{O}$  (nitrous oxide). NO is a colorless toxic gas, and when exposed to oxygen it rapidly forms  $\text{NO}_2$ . The NO molecule is special in that sense, that it has an unpaired electron in an anti bonding orbital and usually such molecules are unstable. NO is the smallest odd electron molecule which is stable.  $\text{NO}_2$  is a brown gas with a characteristic smell and is also highly toxic.

The Zeldovich mechanism [1] describes how NO is formed in a series of chain reactions, with activated  $\text{N}^*$  and  $\text{O}^*$  as intermediates. Reaction (1.1) is the rate determining step, and the process is thermally activated with increased formation of NO at higher temperatures.

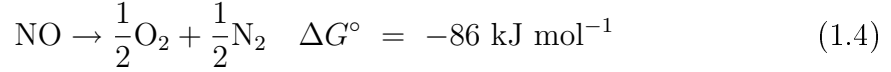


NO can also be formed from oxidation of nitrogen present in fuel and from hydrocarbons in the fuel reacting with nitrogen in the air followed by oxidation [2]. The Zeldovich chain reaction is responsible for the majority of NO formed [3]. Diesel engines run at lower temperatures than traditional engines, and therefore produce less  $\text{NO}_x$  [3].  $\text{NO}_2$  can be formed from NO reacting with  $\text{O}_2$  as in equation (1.3).



The term  $\text{NO}_x$  covers both NO and  $\text{NO}_2$ , but the  $\text{NO}_x$  in a diesel engines exhaust is typically composed of 95 % NO and 5 %  $\text{NO}_2$  [2], therefore the focus in de $\text{NO}_x$  is mostly on removal of NO.

NO is thermodynamically unstable at room temperatures, see equation (1.4), but the activation energy for the decomposition reaction is very high,  $364 \text{ kJ mol}^{-1}$  [4], so a catalyst is necessary.



$\text{NO}_x$  is dangerous both for the environment and for the health of human beings. Inhalation of  $\text{NO}_x$  can cause damage to the respiratory system (lung edema) [5].  $\text{NO}_x$  is also involved in the formation of acid rain [5], smog [6] and depletion of the ozone layer [7]. Ozone is formed by reactions between  $\text{O}_2$  and  $\text{NO}$  in the troposphere [8]. The destruction of ozone in the ozone layer in the stratosphere by  $\text{NO}$  follows the reactions shown in equation (1.5) and (1.6) [2].



The main source of  $\text{NO}_x$  emissions in Europe is traffic [9]. The first regulations on  $\text{NO}_x$  emissions was issued in 1982 for spark ignition vehicles, and in 1988 regulations was also issued for diesel engines [10].  $\text{NO}_x$  can be removed from an oxygen free exhaust stream with a three way catalytic converter (TWCC). The TWCC removes both  $\text{CO}$ ,  $\text{NO}$  and hydrocarbons ( $\text{HC}$ ), but the active catalysts  $\text{Pt}$ ,  $\text{Rh}$  and  $\text{Pd}$  are not active when excess  $\text{O}_2$  are present [11]. Fuel prices are increasing and fuel efficient engines for small vehicles become increasingly popular. Diesel and lean-burn engines operate with a surplus of oxygen. The diesel exhaust contains between 100 and 1000 ppm  $\text{NO}$  and 3 to 15 %  $\text{O}_2$  [12]. Filters can remove particulate matter ( $\text{PM}$ ), and adjustment of the engine can to some extent lower  $\text{NO}_x$  emission. Emission regulations become more and more stringent. From September 2009 the EU emission standard Euro 5 became effective, and the new standards Euro 6 is planned to September 2014, see table 1.1 for the standards for diesel passenger cars[13]. So the necessity of finding new methods for removal of  $\text{NO}_x$  from the

Table 1.1: EU emission standards for passenger cars.

	Date	CO g/km	HC + $\text{NO}_x$ g/km	$\text{NO}_x$ g/km	PM g/km
Euro 5	2009.09 <sup>a</sup>	0.5	0.23	0.18	0.005
Euro 6	2014.09	0.5	0.17	0.08	0.005

<sup>a</sup> 2011.01 for all models

exhaust of diesel engines becomes ever more crucial.

Several methods have all ready been proposed and some commercialised. Selective catalytic reduction (SCR) uses a reducing agent to remove  $\text{NO}_x$  in the presence of oxygen. The principle of nitrogen storage removal (NSR) is to transform  $\text{NO}_x$  into nitrates during lean operation, and then reducing the nitrates to  $\text{N}_2$  under short cycles of fuel rich operation of the engine. Direct decomposition is a simple and desirable way of removing  $\text{NO}_x$  as no reducing agents or changes in driving cycles are required. This work is based on another option: electrochemical removal of  $\text{NO}_x$ .

## 1.1 Methods for removal of NO<sub>x</sub>

### 1.1.1 Direct decomposition

The most advantageous way to remove of NO<sub>x</sub> would be direct decomposition as reducing agents are not required and no power consumption takes place. Both NO and NO<sub>2</sub> are thermodynamically unstable at low temperatures, and should decompose into N<sub>2</sub> and O<sub>2</sub>, but the kinetics for this reaction are very slow. A catalyst can however increase the rate. Several materials are known to catalyse the break down of NO<sub>x</sub>. But none have so far achieved high enough rates of conversion to be applicable to commercial use.

A selective catalyst with a high rate of conversion would present the most advantageous solution to the problem with removal of NO<sub>x</sub>.

### 1.1.2 Selective catalytic reduction (SCR)

The NO<sub>x</sub> is removed from the exhaust stream by reduction over a catalyst with reducing agents. High selectivity and efficiency can be achieved and the technique is applied commercially, mostly for stationary engines. It is a disadvantage for the SCR method that a reducing agent must be applied. Thereby requiring storage and careful dosage.

There are two main types of SCR: urea/ammonia SCR and hydrocarbon SCR (HC-SCR).

#### HC-SCR

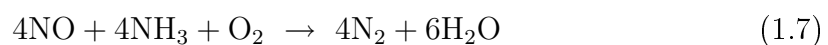
Hydrocarbons, alkanes or alkenes, are used as reducing agent to reduce NO into N<sub>2</sub> in the presence of O<sub>2</sub>. The hydrocarbons are either present in the exhaust (unburned fuel) or added in front of the converter.

Many catalysts have been examined for activity and the most efficient are: Ag/Alumina [11], SnO<sub>2</sub>, H-mordenite and Cu-ZSM5. A major drawback with the technology is that the most catalysts lack activity below 300 °C, even though high activity can be obtained for Ag/Alumina catalyst when hydrogen is added to the exhaust in combination with hydrocarbons. Hydrogen can be formed from the diesel fuel through reforming.

Efficient catalysts for HC-SCR are still lacking though [14].

#### Urea/Ammonia SCR

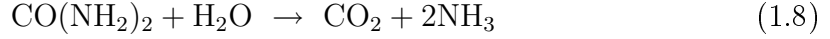
Ammonia can also be used for reducing NO as shown in equation (1.7).



This method is commercialised and widely used to remove NO<sub>x</sub> from the exhaust of stationary sources. For mobile sources it is applied for heavy-duty trucks and

busses, but it is not used for cleaning the exhaust of diesel cars [9]. The reducing agent,  $\text{NH}_3$ , is toxic and a pollutant in the environment just as  $\text{NO}$ , so the addition of  $\text{NH}_3$  to the exhaust must be carefully monitored and adjusted to avoid excess  $\text{NH}_3$ . Furthermore  $\text{NH}_3$  is difficult to store and corrosive.

Urea is used instead of ammonia, because it is safer and easier to store. Then  $\text{NH}_3$  is formed from hydrolysing urea according to reaction (1.8).



The commercial catalyst is  $\text{V}_2\text{O}_5$  supported on titanium and tungsten oxides [15]. This catalyst is also active in oxidising  $\text{SO}_2$  to  $\text{SO}_3$ , which is a disadvantage with Ammonia SCR.

### 1.1.3 Nitrogen storage reduction (NSR)

The NSR method was first presented by Toyota in 1996 [16], and is commercialised in Japan. This method is also known as lean  $\text{NO}_x$  trap (LNT).  $\text{NO}$  molecules are adsorbed and oxidized by a catalyst and stored as  $\text{NO}_3^-$ . The engine is running in cycles, shifting between long periods of lean-burn conditions, where the  $\text{NO}_x$  is stored as nitrates, and short periods with low air to fuel ratio, where the stored nitrates are reduced. Typically an alkaline earth metal oxide such as  $\text{BaO}$  is used for storage, while  $\text{Pt}$  is used for reduction of the stored nitrates [17].

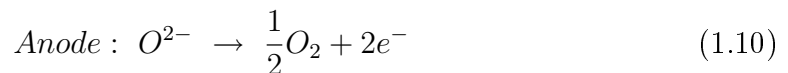
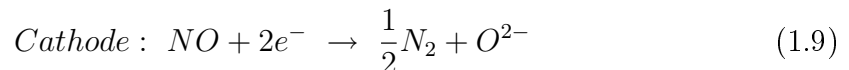
Deactivation by  $\text{SO}_2$  is a challenge of the NSR technique [17], therefore it is only commercialised in Japan, where the natural content of sulphur in oil is very low. The disadvantages with this method is less fuel efficiency as the engine cannot run with high air to fuel ratio all the time, and that careful control with the engine is required.

### 1.1.4 Electrochemical removal of $\text{NO}_x$

The principle for removing  $\text{NO}_x$  with a solid oxide electrochemical cell is the following:

$\text{NO}$  is reduced at the cathode to  $\text{N}_2$ , see equation (1.9), an oxide ions is formed and transported through the electrolyte. Then  $\text{O}_2$  is formed at the anode, see equation (1.10). Figure 1.1 shows a sketch of a solid oxide cell for removal of  $\text{NO}$ .

It is stated in [18], based on thermodynamically calculations, that by careful adjustment of polarisation voltage and choice of cathode material, it should be possible to selectively reduce  $\text{NO}$  instead of  $\text{O}_2$ .



Oxygen is present in the exhaust from an engine running lean, and therefore the reduction of  $\text{O}_2$  (1.11) at the cathode is a competing reaction to the reduction

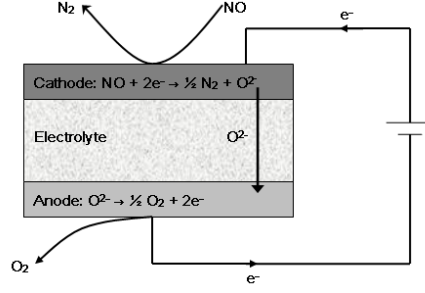
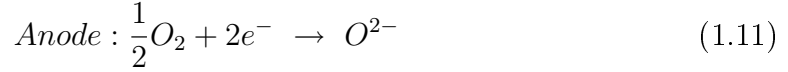


Figure 1.1: Sketch of a solid oxide electrochemical cell for removal of NO<sub>x</sub>.

of NO. If reaction (1.11) is taking place then the cell is functioning as an oxygen pump, and power is being lost. Therefore high selectivity towards nitrogen oxides is required.



Pancharatnam *et al.* [19] introduced the concept of decomposing NO electrocatalytically in 1975. When applying a voltage over a zirconia disc with Pt or Au electrodes, the decomposition of NO increased. As gold is inactive in this process, the reaction had to take place at the zirconia surface. The F-centers ( $V_O^x$ ) were suggested as the active sites, which was confirmed in 1979 by Gür and Huggins [20].

Since then several other studies have been done on the concept of electrochemical removal of nitrogen oxides.

Reduction of NO in an atmosphere containing O<sub>2</sub> was achieved for the first time in 1990 [21] with transition metal oxide electrode on zirconia discs. Up to 91 % NO was removed with 8 % O<sub>2</sub> present for experiments in the temperature range of 650-1050 °C.

La<sub>0.8</sub>Sr<sub>0.2</sub>MnO<sub>3±δ</sub> electrodes were examined by Reinhardt *et al.* [22] for oxygen reduction in the presence of 1000 to 2275 ppm NO in the temperature range of 500 to 900 °C. They proposed that a reactive surface oxygen species were formed from NO<sub>2</sub>, thereby increasing the rate of the oxygen reaction. This was based on electrochemical measurements without any gas analysis.

Hibino *et al.* [23] [24] [25] [26] did a series of experiments concerning electrochemical removal of NO and CH<sub>4</sub> with electrochemical cells with Pd electrodes and ceramic electrolyte in the presence of O<sub>2</sub>, H<sub>2</sub>O and CO<sub>2</sub>. It was proven that it was possible to remove both NO and CH<sub>4</sub> in the presence of oxygen, but that the NO conversion rate decreased with increasing oxygen partial pressure [23]. The NO conversion rate showed no dependence on temperature in the temperature range of 500 to 900 °C. A current efficiency of 1.5 % in the presence of 2 % O<sub>2</sub> was achieved with a Pd|YSZ|Pd cell [24]. These findings suggested that the NO reduction did not take place on the F-centers as suggested in [19] and [20].

By using  $\text{CeO}_2$  and  $\text{Ce}_{0.8}\text{Sm}_{0.2}\text{O}_2$  as electrolytes it was possible to achieve NO conversion down to 400 °C. Likely because of a higher Pd surface coverage of NO at low temperature. The presence of  $\text{H}_2\text{O}$  increased the current efficiency, and it was suggested that NO was reduced by  $\text{H}_2$  formed from electrolysis of  $\text{H}_2\text{O}$ . [25]. When the sintering temperature of the electrodes was increased, the conversion rate of NO increased. Thus the poorer the electrode was at oxygen pumping, the higher NO decomposition. The high sintering temperature decreased the triple phase boundary (TPB) [26].

Wachsman *et al.* [27] used ceramic cells with electrodes of  $\text{La}_{0.8}\text{Sr}_{0.2}\text{Co}_{0.9}\text{Ru}_{0.1}\text{O}_{3-\delta}$  for electrochemical reduction of NO. The electrocatalyst experiments were carried out at 750 °C, and the ratio between NO and  $\text{O}_2$  varied. When  $\text{O}_2$  was added the current necessary for complete reduction of NO increased, because the electrode material was not selective towards NO reduction.

Bredikhin *et al.* [28] [29] [30] [31] [32] [33] did a series of studies on an electrochemical cell with YSZ electrolyte, Pt electrodes and a composite ceramic working electrode covering the Pt electrode. With a  $\text{YSZ}+\text{NiO}|\text{Pt}|\text{YSZ}|\text{Pt}$  cell in the temperature range of 550 to 700 °C in 1000 ppm NO in He with 2 to 4 %  $\text{O}_2$  present. 60 % of NO could be removed at 600 °C with 4 %  $\text{O}_2$  in the atmosphere, with 2 %  $\text{O}_2$  a current efficiency (CE) of 2.5 % could be reached [28]. Working electrodes of YSZ/Pt made it possible to operate the cell at lower current [31]. A theory was proposed that all the gas entering the pores of the working electrode would be reduced, first the  $\text{O}_2$  and later the NO. Therefore the current efficiency could be calculated from the gas concentrations of NO and  $\text{O}_2$ . It was found that higher sintering temperature increased the selectivity and decreased the threshold current, because less  $\text{O}_2$  could reach the YSZ interface through the dense electrode and become reduced [29].

Next step was a  $\text{Pt}+\text{YSZ}|\text{YSZ}|\text{Pt}+\text{YSZ}$  cell with an electro catalytic cathode of NiO/YSZ and a thin YSZ layer on top of the electro catalytic cathode to prevent  $\text{O}_2$  reduction. It was possible to remove 50 % of NO at 600 °C in 1000 ppm NO and 3 %  $\text{O}_2$  with only 1/10 electrical power compared to the cell without the thin YSZ layer [33].

Applying a  $\text{RuO}_2$  layer on top of a Pd electrode can improve the selective for NO compared to  $\text{O}_2$  in the temperature range of 600 to 700 °C as shown by Wang *et al.* [34][35]. The rate determining step (RDS) was suggested to be the transfer of  $\text{O}^{2-}$  into YSZ from the cathode. When Ag was applied instead of Pd the result was the highest NO conversion at 500 °C.

A  $\text{La}_2\text{Sn}_2\text{O}_7$  and YSZ composite electrode was used together with a  $\text{Pt}|\text{YSZ}|\text{Pt}$  cell to remove NO electrochemically by Park *et al.* [36]. A current efficiency of 3 % at 700 °C with 1000 ppm NO was achieved when 2 %  $\text{O}_2$  was present, while it decreased to 1.3 % when the oxygen content was increased to 4 %  $\text{O}_2$ . Again a minimum current density is necessary, before NO decomposition starts, indicating



selectivity towards  $O_2$  compared to NO.

When Pt was added to the  $La_2Sn_2O_7$  and YSZ composite electrode a large increase in the NO conversion was observed [37].

Hansen *et al.* [38] [39] [40] did a series of studies of electrochemical NO decomposition on cone-shaped electrodes. The electrode materials tested was Cu/CuO and perovskites -  $La_{1-x}Sr_xMnO_{3+\delta}$  in the composition range  $0.05 \leq x \leq 0.5$ ,  $La_{0.6}Sr_{0.4}Fe_{0.8}Mn_{0.2}O_{3-\delta}$  and  $La_{0.85}Sr_{0.15}CoO_{3-\delta}$ . The temperature range for the measurements was 300-500 °C and a CGO electrolyte was used. Measurements of current densities indicated that CuO showed selectivity towards NO compared to  $O_2$  [39]. The ability of the metal ion on the B site in the perovskite to change oxidation state and donate an electron to NO for bond breaking seems also to be an important parameter in determining the activity of electrode material; LSM15 seems to have higher activity for NO than LSCo15.

Metal oxides with spinel structure were tested with measurements on cone-shaped electrodes by Simonsen *et al.* [41], and the  $CuFe_2O_4$  spinel showed the highest selectivity for NO. In later work copper and nickel based metal oxide cone shaped electrodes with  $KNiF_4$  structure were examined [42] [43]. The electrodes of  $La_2CuO_4$ ,  $La_2NiO_4$  and  $LaSrCuO_4$  had the best selectivity with the highest current densities for NO reduction compared to  $O_2$  reduction in the temperature scale of 300 to 500 °C. Addition of BaO to LSM15 electrodes seemed to increase the selectivity, while it decreased for the LSCo15 electrodes [41].

Bræstrup *et al.* did further investigations of a series of spinels  $NiFeO_4$ - $MgFeO_4$  for NO reduction with cone-shaped electrodes and the  $MgFeO_4$  electrode shows high activity in NO compared to  $O_2$  [44]. Further studies were made concerning the  $MgMn_xFe_{2-x}O_4$  spinel-type electrodes [45], the tendency was that substitution with Mn tended to decrease the selectivity towards NO.

A multi layered electrochemical cell was used to reduce NO by Hamamoto *et al.* [46]. The application of an  $NO_x$  adsorbent layer of Pt/K/ $Al_2O_3$  on top of the cell increases current efficiency by more than four times. The multilayer cell shows activity from 250 °C, and at 500 °C it is possible to remove up to 90 % of NO with a current efficiency of 10 %. Even with 10 %  $O_2$  present it is possible to remove around 50 % NO with a CE higher than 10 %. This design of the electrochemical reactor seems very promising and shows the best results reported in literature so far, even though the operation temperature needs to be lowered from 500 °C, which is too high compared to the temperature of diesel exhaust.

## 1.2 Catalysis

Many different materials have been shown to catalyse the decomposition or reduction of NO.

### 1.2.1 Zeolites

Aluminosilicate minerals with a micro porous structure are called zeolites. They consist of a framework build from tetrahedral units of  $[\text{SiO}_4]^{-4}$  and  $[\text{AlO}_4]^{-5}$ , where the charge is balanced by the presence of cations in the internal cavities of the structure. Also water and other small molecules can be present in the pores of the aluminosilicate structure .

The type of zeolites used for the direct NO decomposition is Cu-exchanged ZSM-5 (Zeolite Socony Mobil)[47].

### 1.2.2 Noble metals

Pt is known to catalyse the reduction of NO, and are used in TWCC together with Rh, Ir and Pd.

Pt is a good catalyst for the NO decomposition reaction, but unfortunately oxygen acts as an inhibitor and besides that Pt is very expensive.

According to [3] the following metals can catalyse the reduction of NO, Pt being the most active: Ni, Ir, Rh, Pd, Pt, Ru.

### 1.2.3 Metal oxides

#### Simple metal oxides

Simple metal oxides are reported to have activity toward the catalysing the NO reduction, but their activity is not very good compared to the activity observed for zeolites and perovskite type structures. Winter [48] examined 40 different metal oxides for catalytic activity towards NO decomposition in 1971.

$\text{Co}_3\text{O}_4$  doped with alkali metal shows activity for NO decomposition [49].  $\text{MgO}$  doped with Ba is an active catalyst for NO and  $\text{N}_2\text{O}$  decomposition [50].

#### Perovskites

Perovskite is a mineral with the formula  $\text{CaTiO}_3$ , but materials with the formula  $\text{ABX}_3$  are called perovskite type, where A and B are large and small cations respectively and the anion X are  $\text{F}^-$  or  $\text{O}^{2-}$ .

The perovskite type structure can be seen as an array of packet  $\text{BO}_6$  octahedral, shearing oxygen atoms in the corners, and then the A atoms are packed in between. This is illustrated in figure 1.2 at the left, where purple atoms are the A ion and the green octahedral enclose the B ions.

Figure 1.2 shows the unit cell for the perovskite type structure to the right, where the white circles in the corners of the green octahedral around the B ion are oxide ions and the purple are the A ion [51].

It is possible to have many different cations at the sites for A and B, but the joined valence must naturally be +6 to balance the three oxide ions, this leads to three possible valence pairs of +3+3, +2+4 and +1+5. A is usually an alkali, alkaline earth or rare earth metal ion. The B cation is medium to small in size and is

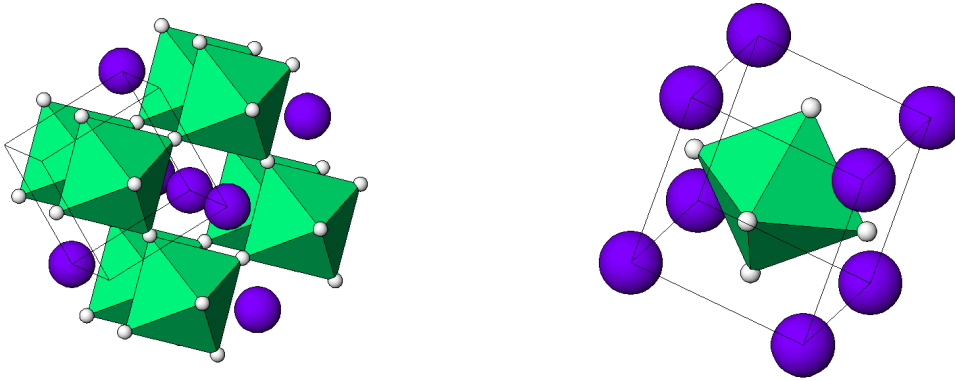


Figure 1.2: At the left: picture of perovskite structure and to the right picture of the perovskite type unit cell.

often a transition metal [51].

Some perovskites conduct oxide ions better than others, and much effort has been put into finding a way to determine the properties with theoretical calculations. The most relevant parameter is the radii of the A and B ions. This results from the geometrical requirements, because the oxide ion needs a path with a certain diameter to travel through the structure [52].

The perovskite structure can be doped, both at the A and B site. If the formula is  $A_{1-x}A'_xB_{1-y}B'_yO_{3\pm\delta}$  and the fractions  $x$  and  $y$  are not too large, then  $A'$  and  $B'$  can have different valence from A and B, and this can alter the perovskite structure abilities to transport oxide ions or conduct electrons.

The catalytic properties of perovskite type structures have been known for long time. Back in 1972 Voorhoeve *et al.* [53] used  $\text{La}_{0.7}\text{Pb}_{0.3}\text{MnO}_3$  for the catalytic reduction of NO. Shin *et al.* [54] showed that  $\text{SrFeO}_{3-x}$  perovskite could adsorb and decompose NO in 1979. Afterward many different perovskite systems have been shown to catalyse the decomposition of nitrogen oxides.

The system of  $\text{La}_x\text{Sr}_{1-x}\text{M}_y\text{M}'_{1-y}\text{O}_{3-\delta}$  has been studied with M and M' equal to Co, Mn, Ni [55], Cu, Fe [56][57], Ru [27].

$\text{La}(\text{Ba})\text{Mn}(\text{In})\text{O}_{3-\delta}$  perovskite showed increasing activity with In at the B site [58]. Another perovskite related structure is the  $\text{K}_2\text{NiF}_4$  structure, which can be expressed as  $\text{A}_2\text{BX}_4$ .  $\text{La}_{2-x}\text{Sr}_x\text{CuO}_4$  and  $\text{La}_{2-x}\text{Sr}_x\text{NiO}_4$  were shown to be electrochemically active towards reduction of NO by Simonsen *et al.* [42] [43].

## Spinel

Spinel is the name of the mineral  $\text{MgAl}_2\text{O}_4$ , and ternary oxides with the general formula  $\text{AB}_2\text{O}_4$  are also called spinels. The cations A and B can have valence between 1 and 6 as long as they can balance the negative valence of the four oxide ions. Generally A and B are transition metal, but also alkali and alkaline earth

metals can participate in the structure [51].

The oxide ions are face-centred cubic (FCC) coordinated, where the cations occupy half of the octahedral sites and 1/8 of the tetrahedral sites. The A and B ions can intermix and the structure can accommodate oxygen vacancies if balanced by shift in oxidation state of cations[51].

Spinel, with the composition  $AB_2O_4$  ( $A = \text{Co, Mn}$  and  $B = \text{Cr, Fe}$ ), have been tested for activity for removal of soot and  $\text{NO}_x$  by Fino *et al.* [59], and the  $\text{CoFe}_2\text{O}_4$  showed the highest activity for  $\text{NO}_x$  reduction.

Bræstrup *et al.* [44] [45] [60] did a series of studies of various spinels as electrode material for electrochemical de $\text{NO}_x$ , and found several spinels which were active for reduction of NO.

### Fluorite

Fluorite is compound with the formula  $\text{CaF}_2$ , while the fluorite structure has the general formula  $\text{MX}_2$ , where M is a tetravalent metal ion and X is oxide or fluoride ions. The cations are usually large and the structure can be described as a FCC packing of metal cations with oxide ions in the tetrahedral holes. This way the cations are fourfold coordinated with respect to oxygen [51]. The fluorite structure can be seen in figure 1.3

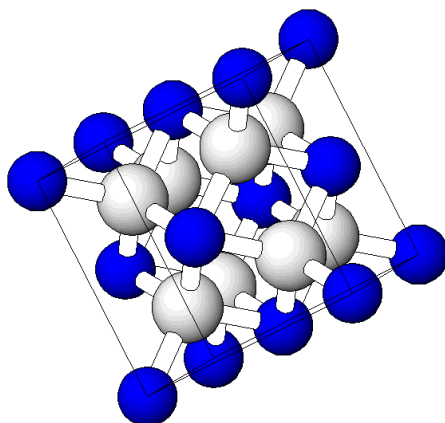


Figure 1.3: The fluorite unit cell, where oxide ions are white and metal ions blue.

When the ratio between cation to anion radius is at least 0.732, then the fluorite structure can be stable for metal oxides of the type  $\text{MO}_2$  [51].

$\text{CeO}_2$  doped with  $\text{Mn}_2\text{O}_3$  and added Ba showed activity for direct decomposition of NO according to [61] also in the presence of  $\text{O}_2$ . The activity was very low, however, in the absence of Ba.

### Pyrochlore

The mineral  $\text{CaNaNb}_2\text{O}_6\text{F}$  has the name pyrochlore, and ternary oxides of the pyrochlore type can given the formula  $\text{A}_2\text{B}_2\text{O}_7$ .

Lanthanum stannate pyrochlore  $\text{La}_2\text{Sn}_2\text{O}_7$  has been used in a composite electrode together with YSZ for electrochemical NO decomposition with success [36].

#### 1.2.4 Addition of compounds to increase activity

The literature provides many examples of active catalysts, which increased their activity when other compounds such as simple oxides or alkaline earth metals were added. In some cases the activity for the  $\text{deNO}_x$  process was very dependent on the dopant.

The addition of Ba has in several cases shown to increase activity. Ce-Mn oxides was only active for NO decomposition when Ba was added [61], and MgO loaded with Ba also shows activity, highest for 4 mol% Ba addition[50]. BaO has also been tested on electrodes of LSM15 and LSCo15 by Simonsen *et al.* [62], where it increased the activity of the LSM15 electrode in NO containing atmosphere.

Haneda *et al.* [49] showed that without alkali metal doping, then  $\text{Co}_3\text{O}_4$  was not active for the direct decomposition of NO.

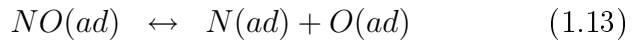
#### 1.2.5 Kinetics

Many different reaction schemes and corresponding rate laws for the NO decomposition process have been proposed in the literature. Some of these are presented in this section

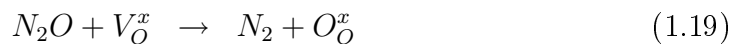
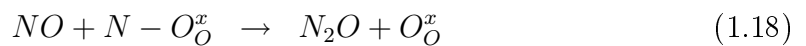
The process of reduction of NO is not simple, many different surface species can participate and the proposed reactions schemes depend on the chosen catalyst material.

To some extent it can be determined what the reaction order is for  $\text{O}_2$  and NO through experiments. Some uncertainty arises from the fact that the decomposition reaction itself produces  $\text{O}_2$ , so more  $\text{O}_2$  will be present, than the amount in the feed stream. This is however not a problem for electrochemical reduction of NO when a nonporous electrolyte is applied, as  $\text{O}_2$  is only formed at the anode.

For electrochemical reduction of NO on perovskites Kammer *et al.* [40] proposed the following simple mechanisms:



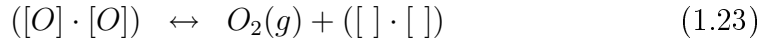
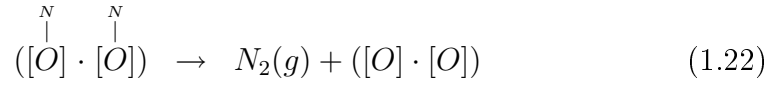
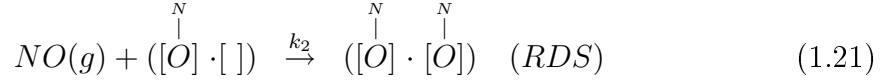
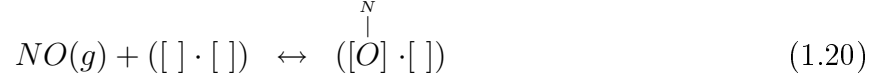
Pancharatnam *et al.* [19] proposed in 1975 a mechanism for electrochemical decomposition of NO, where  $\text{N}_2\text{O}$  is an intermediate, which is presented below.



Teraoka *et al.* [55] studied Co and Mn based perovskites for direct decomposition of  $\text{NO}_x$ . They found that the reaction order with respect to NO is nearly 1 and that  $\text{O}_2$  is an inhibitor with a reaction order between 0 and -1.

The reactive site is proposed to be two adjacent surface oxide ion vacancies ( $[ ] \cdot [ ]$ ) which can adsorb two NO molecules.

The following mechanism was proposed.

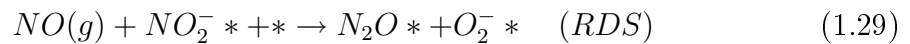


For the decomposition of NO over the perovskite  $\text{La}_{1-x}\text{Ba}_x\text{Mn}_{1-y}\text{In}_y\text{O}_{3-\delta}$  the following mechanism was proposed, where \* denotes a surface adsorption site [58].  $\text{N}_2\text{O}$  is an intermediate in the process.



The study done by Tofan *et al.* [56][57] reveals that for NO decomposition over  $\text{La}_{0.66}\text{Sr}_{0.34}\text{Ti}_{0.66}\text{Cu}_{0.34}\text{O}_{3-\delta}$  only  $\text{NO}_2$  and  $\text{N}_2$  is formed, so in this case no  $\text{O}_2$  is formed.

For NO decomposition on MgO loaded with Ba,  $\text{N}_2\text{O}$  is also assumed to be an intermediate, but Raman spectroscopy also showed  $\text{NO}_2^-$  and  $\text{NO}_3^-$  ions at the surface, so the mechanism with an ionic species as another intermediate was proposed by [50]. The first steps until formation of  $\text{N}_2\text{O}$  are shown in equations (1.28) and (1.29)



### Inhibition by $\text{O}_2$

$\text{O}_2$  is known to inhibit the NO decomposition reaction. The adsorbed oxygen molecules can take up place at the active sites, so there is less room for NO molecules to adsorb. Presence of  $\text{O}_2$  decreases the number of oxygen vacancies, which would inhibit the NO decomposition reaction if the reactive sites are oxygen vacancies.

Beside that the adsorbed oxygen molecules are also reported to participate in competing surface reactions, where the resulting molecules are not  $\text{N}_2$  but rather NO and  $\text{NO}_2$ [57].

Doping with In in  $\text{LaMnO}_3$  on the B site shows a much higher yield of  $\text{O}_2$  in temperature programmed desorption (TPD), which could be interpreted as the In doping makes oxygen adsorption strength weaker [58].

### Active sites

F-centers were first suggested as the reactive site by [19]. Oxide ion vacancies are reported in many places [27] to be the active site for the NO decomposition for perovskites. An oxide ion vacancy with two trapped electrons is called an F-center ( $V_{\text{O}}^x$ ) [63]. The reaction path for NO molecules is often described as being bimolecular in the literature [54], [55]. Two NO molecules should adsorb on two pair wise oxygen vacancies ( $[ \cdot ]$ ), a bond is formed between the two N,  $\text{N}_2$  is released, and afterwards  $\text{O}_2$  is formed. The formation of  $\text{O}_2$  being the rate limiting step.

The active site for NO decomposition in  $\text{LaMnO}_3$  is proposed to be the Mn ion and a Mn-O-Mn site by [64]. The metal ion vacancies play an important role as the substance with the  $\text{LaMnO}_{3.15}$  is more active than  $\text{LaMnO}_{3.01}$ .

Likewise Tofan *et al.* [56] [57] considers the B-site cation in the perovskite structure,  $\text{ABO}_{3-\delta}$  to be the source of the active sites together with oxygen vacancies.

The doping of  $\text{LaSrNiO}_4$  at the A site with Ce should give a new active site,  $\text{Ce}^{3+}(\text{O})-(\text{Ni}^{2+}-[ \cdot ]-\text{Ni}^{3+})$  [65].

Shin *et al.* [54] suggested oxygen deficiencies next to  $\text{Fe}^{+4}$  in  $\text{SrFeO}_3$  as the active site. Two NO molecules should absorb adjacently, and  $\text{Fe}^{+3}$  change oxidation state to +4, thus donating electrons to the forming  $\text{N}_2$  molecule. The  $\text{SrFeO}_3$  lattice can sustain the unusually oxidation state +4 for iron.

NO decomposition over zeolite Cu-ZSM-5 proceeds via  $\text{N}_2\text{O}$  formation, and the  $\text{N}_2\text{O}$  decomposition are proposed to happen at the bis( $\mu$ -oxo)dicopper cores. The rate determining step, the oxygen recombination happens fast when two oxygen atoms are in near distance [47].

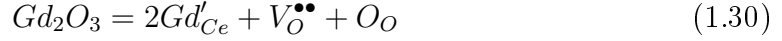
## 1.3 Materials

The electrodes investigated in this work are sets of composite electrodes of metal oxides. It appears from the text above that there is a vast field of different possible compositions of solid oxide composite electrodes, and the ones chosen here are just a few of the many. These few were closely examined with various electrochemical techniques.

The materials for the composite electrodes are perovskites-type ( $\text{A}_{1-x}\text{A}'_x\text{B}_{1-y}\text{B}'_y\text{O}_{3\pm\delta}$ ) and fluorite-type ( $\text{M}_{1-z}\text{M}'_z\text{O}_{2-\delta}$ ). The perovskite-type materials chosen are:  $\text{La}_{1-x}\text{Sr}_x\text{MnO}_3$  ( $x = 0.15, 0.5$ ) and  $\text{La}_{1-x}\text{Sr}_x\text{Co}_{1-y}\text{Fe}_y\text{O}_{3-\delta}$  ( $x = 0.25, 0.4$  and  $y = 0.8$  and  $1$ ). The fluorite-type structures are based on ceria:  $\text{Ce}_{0.9}\text{Gd}_{0.1}\text{O}_{1.95}$  (CGO10) and  $\text{Ce}_{1-z}\text{Pr}_z\text{O}_{2-\delta}$  ( $z = 0.1, 0.2$ ).

## Ceria

$\text{CeO}_2$  has fluorite structure and mixed ionic and n-type electronic conductivity. The electronic conductivity is dominating in pure reduced ceria,  $\text{CeO}_{2-x}$  and takes place with a small polaron ( $\text{Ce}^{+3}$ ) transport [66]. Ceria can be doped with other metal oxides such as gadolinia or praseodymium oxide, which gives higher ionic conductivity. Some of the  $\text{Ce}^{+4}$  ions has been exchanged with  $\text{Gd}^{+3}$  in CGO10, and thereby some oxygen vacancies are created,  $V_O^{\bullet\bullet}$ , see equation (1.30) [66].



Ionic conductivity is dominating for CGO in air. CGO is used as an electrolyte in SOFCs, and has much better ionic conductivity at low temperatures than YSZ.

Doping ceria with praseodymium introduced p-type conductivity ( $\sigma_e$  for CPO20 is around  $1.6 \cdot 10^{-2} \text{ S cm}^{-1}$  at  $600^\circ\text{C}$  [67]). CPO is used for many different applications such as SOFC electrodes [68], gas sensors [69] and soot oxidation [70]. The Pr ions can easily change oxidation state between +4 and +3, therefore CPO might have some catalytic properties.

## LSM

Lanthanum manganite doped with strontium, LSM, is used as a SOFC cathode material. It has perovskite structure and high electronic conductivity (p-type). LSM is a poor ionic conductor, but its conductivity increases when reduced. LSM is often used in SOFC electrodes, as it is a good oxygen electrode. LSM has also been tested for activity for electrochemical reduction of NO [22][27]. Hansen *et al.* [38] found that electrodes of LSM15 had the highest activity in NO, when testing electrodes with compositions in the range  $\text{La}_{1-x}\text{Sr}_x\text{MnO}_3$  with  $0.05 \leq x \leq 0.5$ . When studying the same range of perovskites as catalysts for SCR the maximum conversion of NO was seen for LSM50 [71] and it was concluded that increasing the Sr content made LSM more active towards oxidation of NO to  $\text{NO}_2$ .

## LSCF

Electrodes of  $\text{La}_{1-x}\text{Sr}_x\text{Co}_y\text{Fe}_{1-y}\text{O}_{3-\delta}$  has been suggested for intermediate temperature solid oxide fuel cells (IT-SOFC) because of limited performance of LSM electrodes at temperatures below  $800^\circ\text{C}$  [72] [73]. LSCF is a mixed ionic electronic conductor (MIEC), and the ionic conductivity for  $\text{La}_{0.8}\text{Sr}_{0.2}\text{Co}_{0.2}\text{Fe}_{0.8}\text{O}_{3-\delta}$  (LSCF20) at  $600^\circ\text{C}$  is around  $10^{-2} \text{ S cm}^{-1}$  [74]. The electrical conductivity is of p-type.  $\text{La}_{0.6}\text{Sr}_{0.4}\text{Co}_{0.2}\text{Fe}_{0.8}\text{O}_{3-\delta}$  (LSCF40) has higher electrical conductivity than  $\text{La}_{0.75}\text{Sr}_{0.25}\text{Co}_{0.2}\text{Fe}_{0.8}\text{O}_{3-\delta}$  (LSCF25), at  $600^\circ\text{C}$   $340 \text{ S cm}^{-1}$  compared to 230 and  $170 \text{ S cm}^{-1}$  for LSCF30 and LSCF20 [75].

There are many examples in the literature of LSCF being used as electrode material in electrochemical cells for NO removal [76] [27] [32].

## Composite electrodes

There are three different paths for the oxygen reduction in SOFC cathodes [77]:



1. The electrode surface path. Oxygen is adsorbed on the surface of the cathode and diffuses along the surface to the TPB, where charge transfer takes place.
2. The bulk path. The oxygen is reduced at the surface of the electrode, and the oxide ions transported through the electrode to the electrolyte.
3. The electrolyte surface path. The oxygen is adsorbed on the surface of the electrolyte and diffuses to the TPB, where charge transfer takes place.

The area where the oxygen can be reduced is very limited both for path no. 1 and 3, while for path no. 2 the reduction reaction can take place all over the cathode, but ionic conductivity is required for the electrode. A material such as LSM which is often used for SOFC electrodes have good electronic conductivity, but lacks ionic conductivity, while LSCF on the other hand has some ionic conductivity. By mixing a material, which is a good electronic conductor, with a material which is a good ionic conductor, the electrodes become more active.

Electrons are required for NO reduction and oxide ions are formed, so the composite electrodes can also be applied for these types of electrodes.

## 1.4 Characterisation of materials

### X-ray powder diffraction

X-ray powder diffraction can be used to identify phases in powder and to confirm if the powder is single phased. Electrons are emitted from a heated filament and accelerated by a potential difference. The electrons hit a metal target, which emits X-ray radiation. A spectrum of X-rays is emitted with two strong peaks ( $K_\alpha$  and  $K_\beta$ ), the frequencies of these two peaks depends on the metal target, usually copper or molybdenum. Normally the  $K_\alpha$  line is selected and all other frequencies are filtered out.

X-rays can be reflected from crystal planes, when the conditions set in Braggs equation (1.31) are meet.  $\lambda$  is the wavelength,  $d$  is the spacing between crystal planes and  $\theta$  is the incident angle between the crystal planes and the X-ray beam, see figure 1.4.

$$n\lambda = 2d \sin \theta \quad (1.31)$$

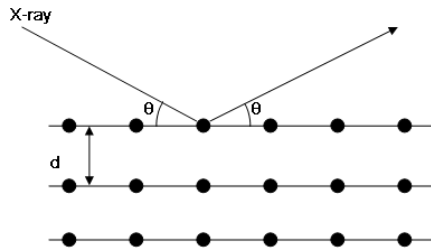


Figure 1.4: Diffraction of X-rays from crystal planes.

When X-rays are diffracted from powder samples, diffraction will occur from the crystals which are oriented such that the conditions of Bragg's equation is fulfilled. When scanning the powder sample over a certain range of  $2\theta$  values a diffraction pattern can be obtained, like the one in figure 1.5. The reflections can be indexed and

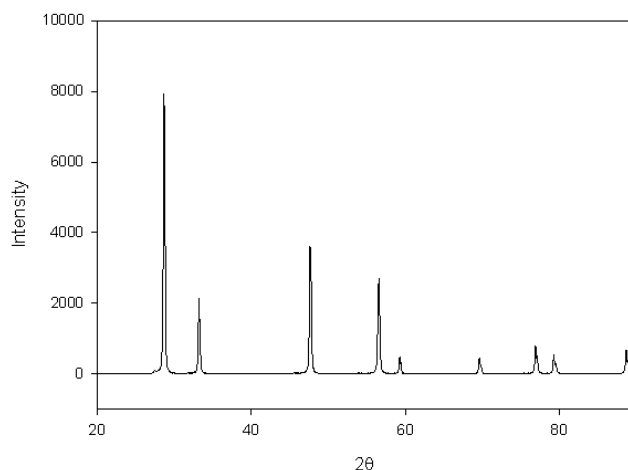


Figure 1.5: Diffraction pattern of CPO20.

connected to the planes from which they arise. When comparing the peaks in the powder diffraction pattern with powder diffraction patterns from other known materials from a database the material can be identified, and the phase purity confirmed. Although the method can not be expected to detect other phases which constitute less than 5 % of the sample. [78]

### X-ray Absorption Near Edge Spectroscopy

X-ray absorption near edge spectroscopy (XANES) can be used to determine the oxidation state of atoms and their coordination. XANES measurements can be done in-situ, so the change in oxidation state and coordination for certain atoms due to atmosphere or temperature change can be monitored.

A core level electron can absorb an X-ray, if the energy of the X-ray is higher than the binding energy of the electron. The excess energy is ejected as a photo electron from the atom.

Absorption only takes place if there is an available state for the photo electron. The released photo electron can also scatter among the neighbouring atoms, and the absorption coefficient value will change due to this. Therefore information regarding the crystal structure can be extracted from the spectra. For the absorption energy ( $\mu$ ) as a function of the energy there will be a sharp rise when the energy reaches the binding energy of a core electron. The pre-edge, the edge and the beginning of the fine structure is called XANES, it covers approximately 50 eV. The region afterwards, the rest of the fine structure is called extended X-ray absorption fine structure (EXAFS), see figure 1.6 [78].

The binding energy of the core electrons are depending on the atomic number,

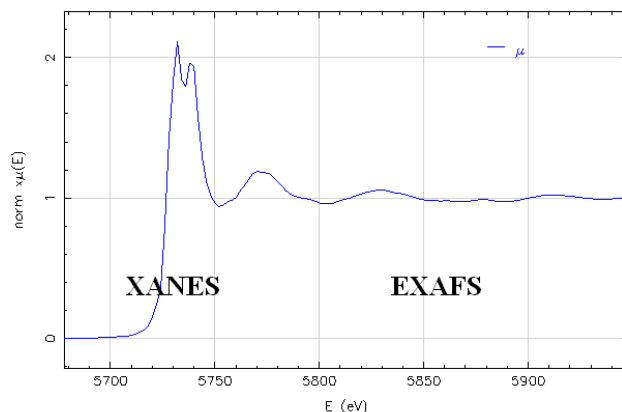


Figure 1.6: Normalised absorption energy as a function of energy for the Ce L3 peak.

and both K and L shell core electrons can adsorb X-rays. For a specific element an energy edge in a suitable energy can be found from the known bonding energies. The XANES region is dependent on oxidation state and coordination of the atom. Therefore the specific oxidation state of a compound can be found from linear combinations of spectra of the same metal in identical coordination with known oxidation states.

To align the spectra a reference is used, usually the element investigated or one with an energy edge close to the expected value for the element.

## 1.5 Electrochemical characterisation

### EIS

Electrochemical impedance spectroscopy (EIS) can be used for characterisation of electrodes. Separation of the arcs which compose the impedance spectra can give valuable information about how adsorption takes place, electrode structure and current transfer etc.

Alternating current (AC) can be described as in equation (1.32) and equation (1.33) is the correspondingly equation for the voltage. The time is given as  $t$ ,  $\omega$  is the frequency,  $I_o$  and  $E_o$  are the amplitudes for the current and the polarisation. The current and the polarisation are not necessarily in phase, the phase difference is called  $\phi$ .

$$I(t) = I_o \cos(\omega t + \phi) \quad (1.32)$$

$$E(t) = E_o \cos(\omega t) \quad (1.33)$$

From Ohm's law the resistance (R) can be found as the polarisation (E) divided by the current (I). Likewise the impedance is defined as the polarisation from (1.33) divided by the current from (1.32) as seen in (1.34).

$$Z = \frac{E(t)}{I(t)} = \frac{E_o \cos(\omega t)}{I_o \cos(\omega t + \phi)} = Z_o \frac{\cos(\omega t)}{\cos(\omega t + \phi)} \quad (1.34)$$

The impedance is a complex quantity with both a real and an imaginary part, as seen in equation (1.35).

$$Z(\omega) = Z_o(\cos \phi + j \sin \phi) \quad (1.35)$$

The impedance can be represented as a vector with the length  $Z_o$ , and if Re is on the x-axis and Im on the y-axis, then the angle between the x-axis and the impedance vector will be  $\phi$ .

The impedance data can be modelled with an equivalent circuit, and then the elements of the equivalent circuit can be linked to physical, chemical or electrochemical processes. The arcs reflect chemical and physical processes, and by varying experimental parameters such as atmosphere and temperature, the nature of the processes connected to the impedance arcs can be uncovered. Different elements for equivalent circuits can be seen together with their corresponding impedance in table 1.2.

Table 1.2: Elements in equivalent circuits

Element	Impedance
Capacitor	$Z = \frac{1}{j\omega C}$
Resistor	$Z = R$
Inductor	$Z = j\omega L$

The elements can be combined in series and parallel in order to get the best fit for the data. Most often the semi circles in the impedance are depressed, resembling arcs instead. This is referred to as a constant phase element (CPE), the impedance of a CPE can be found in equation (1.36), where  $Y_0$  is  $|Z|$  and  $\alpha$  has a value between 0 and 1, where 1 corresponds to an ideal capacitor. Constant phase elements are caused by nonideality of the system measured [79].

$$Z = \frac{1}{Y_0(j\omega)^\alpha} \quad (1.36)$$

Impedance data is often represented in a Nyquist plot with the real part of the impedance on the x-axis and the imaginary part times -1 on the y-axis.

### Cyclic voltammetry

Cyclic voltammetry (CV) is an electrochemical measurement technique, where the potential is changed linearly with time and the current response recorded. The potential is ramped until a certain potential is reached (the limit potential), and

then the ramp is inverted. The ramp for the change in potential is called the scan range. In this study CV is mostly used to evaluate the electrochemical activity of the electrodes in different atmospheres, by comparing the current densities at similar potential.

### Chronoamperometry

Chronoamperometry is a very simple electrochemical technique, where the potential is kept stable for a certain time period while the current is measured as a function of time. When the electrodes are polarised, gas conversion can be measured with equipment for gas analysis.

## 1.6 Measurement of gas composition

Gas analysis is an important tool in investigating potential electrode materials activity. If conversion takes place, the change in gas composition can be seen with the gas analysis equipment and be compared to current consumption.

### Mass spectrometer

Mass spectrometry works by ionising the gas molecules, and then the detector can find the mass of the ions as a function of their speed. A mass spectrogram is produced where the x-axis shows the mass of the molecule divided by the charge ( $m/Z$ ) and the y-axis the intensity.

Some molecules can be split into fractions when ionised and others can loose more than 1 electron, when ionized. For instance can  $\text{NO}_2$  split into NO and N, and from  $\text{N}_2$  there is both a large peak at  $m/Z = 28$  and a much smaller one at  $m/Z = 14$ . During the measurements the height of all the peaks can vary a bit, therefore it is best to look at the relative height, that is set the height of the peak for one component to 1 and look at all other peaks relative to this peak. As the concentrations of NO,  $\text{NO}_2$ ,  $\text{N}_2\text{O}$ ,  $\text{N}_2$  and  $\text{O}_2$  are quite small the height of these compounds were all set relative to the height of the Argon peak at  $m/Z = 36$  (a smaller isotope Ar peak), as the big Ar peak at  $m/Z = 40$  is many times larger than the small concentrations of the compounds that are interesting for these experiments.

It is necessary to calibrate the equipment in order to transfer the height of the peaks into actual concentrations of the gas components. If the height of the  $\text{N}_2$  peak at  $m/Z = 28$  decreases by 50%, then the concentration of  $\text{N}_2$  has probably also decreased by 50%, but before that conclusion can be drawn, it must be shown that the relationship between the actual gas concentrations and the height of the peaks is in fact linear.



# Chapter 2

## Experimental

### 2.0.1 Glycine nitrate combustion synthesis

The glycine nitrate combustion synthesis was used for synthesis of metal oxides [80]. Metal nitrate solutions were mixed in stoichiometric amounts and glycine was added. The ratio between glycine and nitrate was to 0.548. The solution was evenly distributed in 2 l glass beakers, with 1 beaker for each 0.2 M of final product. Each beaker was placed on a heating plate and heated with around 175 °C until the evaporation of water turned the solution into a highly viscous liquid with intense formation of bubbles. This process took between 90 to 180 minutes depending on heating and concentration of the nitrate solutions. Then the beaker was placed under a hood, and the heating plate was switched to maximum heat. The solution started to react within minutes, and the metal oxide powder was formed. The reaction could be rather violently, where powder was thrown out of the beaker; therefore the hood was placed above the beaker to collect the powder. Afterwards the powder was ball milled for 24 hours and then calcinated.

## 2.1 Experimental setups

The preparation of the samples and test conditions are described in details in the experimental section of each chapter.

### 2.1.1 XANES setup

The XANES measurements were done at the C beam line at the DORIS III ring at HASYLAB, DESY, Hamburg in Germany. The spectra were aligned with a reference foil of Cr, where the K1 edge is very close in energy to the L3 edge of Pr. A Si(111) monochromator was used in the experiments. The setup for the in-situ measurements are shown in figure 2.1, it is a home made setup, which is described by Hagen *et al.* [81]. A sample pellet is placed in a holder inside the glass tube. The glass tube is equipped with Kapton windows and the atmosphere inside the glass tube can be controlled. Further the glass tube is placed in a tubular furnace, which is seen in figure 2.1, so the temperature could be controlled.

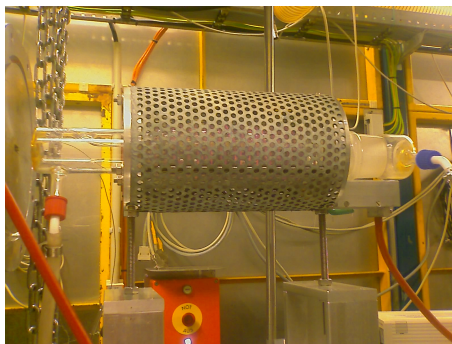


Figure 2.1: The setup for the XANES measurements. The beam passes through the glass tube in the oven seen in the picture.

### 2.1.2 Electrochemical setups

Four types of electrochemical cells have been tested in this work.

#### Cone setup

The cone electrodes were used for screening of electrode materials, and had the advantage that microstructure effects are minimised. The concept of point electrodes was first demonstrated by Fabry *et al.* [82]. The cone setup was a pseudo three electrode setup, where the cone was the working electrode and the tip was pressed into contact with a YSZ electrolyte. A counter electrode and a reference electrode was placed under the YSZ plate, see figure 2.2 for a sketch of the setup. The reference gas was air, while the atmosphere at the cone could be changed between air and 1 % NO in Ar. The point in which the tip of the cone touches the YSZ electrolyte was the TPB. EIS and CV measurements were performed on the cones, furthermore

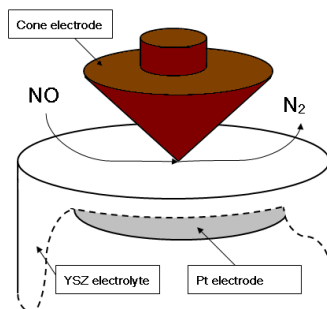


Figure 2.2: Sketch of the cone setup.

the OCV was measured and in some cases the cones were subjected to polarisation before CV measurements. It is not possible to measure any gas conversion with the cone setup due to the limited contact between cone tip and electrolyte.

The contact area was calculated with Newmans formula [83] from the conductivity of YSZ and the  $R_s$  value obtained from EIS. Knowing the contact area is necessary in order to calculate current density for comparison of cyclic voltammograms for dif-



ferent cones. The cones were made by pressing metal oxide powders into cylindrical shape followed by sintering and mechanically shaping.

### Symmetrical cells

The symmetrical cells were two electrode, four wire cells. The cells consisted of two identical electrodes on each side of an electrolyte tape. The symmetrical cells were used for screening of electrodes and subjected to EIS measurements at OCV. Only one atmosphere was present and gas conversion cannot be measured. The electrodes were screen printed on both sides of CGO tape, which had a thickness of approximately  $180\text{ }\mu\text{m}$ . The screen printed cells had the dimensions  $5\text{ cm} \times 5\text{ cm}$  and were cut into many small cells in the size  $6\text{ mm} \times 6\text{ mm}$ .

Gold paste with 20 wt. % carbon was applied to the electrodes, and afterwards the sides of the cells were rinsed with ethanol in order to remove excess gold paste causing short circuit. The cells were placed between two alumina holders covered with gold net with a weight load pressing the gold net into contact with the cells. Four similar cells were mounted in the setup and tested sequentially. This was done to test the reproducibility of the data.

### Three electrode cells

The three electrodes were the working electrode, the counter electrode and the reference electrode. The working electrode was the electrode which properties should be investigated. The three electrode cells could be used for EIS, CV and chronoamperometry. Further the OCV could be measured in different atmospheres. Gas conversion could be measured over the three electrode cell with gas analysis equipment during polarisation.

The working electrode was screen printed onto the CGO or YSZ pellets. Winkler *et al.* [84] designed the geometry of the three electrode test cells used as standard at Risø, in order to obtain a uniform current distribution and thereby reliable values for  $R_p$ . See figure 2.3 for a sketch of the geometry of the cylindrical three electrode cell. The counter electrode was painted onto the surface of the pellet with Pt paste

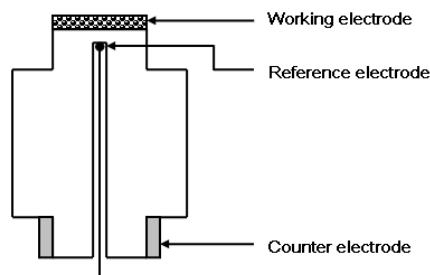


Figure 2.3: Sketch of the three electrode test cell.

as shown in figure 2.3. The working electrode was screen printed onto the three electrode pellet. The diameter of the working electrode is  $72\text{ mm}$ . Gold paste with 20 wt. % carbon (pore former) was used as current collector, together with some

gold mesh.

The three electrode pellet was placed between two alumina tubes, see figure 2.4 for a sketch of the setup. Silver and glass was used as sealings. A glass tube with an

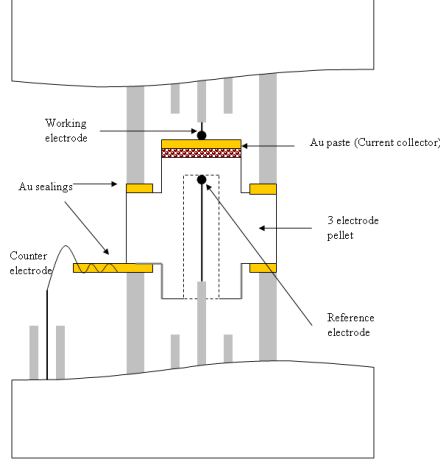


Figure 2.4: Sketch of the three electrode setup.

inert purge gas (Ar) surrounded the setup and a vertically mounted furnace was used to heat the setup. The atmosphere at the counter electrode was air, while the atmosphere at the working electrode was changed between air, 0.1 % NO in Ar and 0.1 % NO + 5 % O<sub>2</sub> in Ar. The gas flow was controlled with Brooks mass flow controllers. The measurements were done in the temperature range 300 to 600 °C. There is a thick layer of electrolyte between the reference electrode and the working electrode, and therefore the potential should be corrected for the ohmic loss, as shown in equation (2.1), where  $R_s$  can be found from impedance measurements.

$$E_{reel} = E_{measured} - R_s I \quad (2.1)$$

### Porous cell stacks

The porous cell stacks were two electrode cells in one atmosphere. The two electrodes were working electrode and counter electrode. The porous cell stacks were subjected to EIS, CV and chronoamperometry, even though any potential applied was versus OCV, as no reference electrode was present. The outlet gas composition could be measured with gas analysis equipment. The cell stacks consisted of interchanging layers of laminated electrode and electrolyte tape. The electrolyte was CGO10 and the electrode was composite metal oxide electrode. The porous cell stacks were developed especially for the exhaust purification group at Risø [85] with the purpose of achieving good contact between electrode and gas molecules, so that gas conversion could be detected at low temperatures.

The porous cell stacks were round with a diameter around 12 mm, and a thickness of 200-400  $\mu\text{m}$  depending on number of layers and thickness of layers. Gold paste with 20 wt. % carbon was painted onto the electrodes as current collector, and afterwards the sides of the cell stacks were grinded in order to avoid short circuit.

Two different setups were used for the porous cell stacks. Initially the porous cell stack was placed in the same setup as the three electrode pellets, with gold and glass sealings, and with NO containing gas flowing through the cell. Argon was used as the purge gas. Later a special setup for the porous cell stacks was developed, where the cell stack was placed between two alumina tubes without any sealing. The sealings could be avoided because a glass tube with o-rings as sealings surrounded the alumina tubes. Therefore it could be avoided to warm the setup up to 1000 °C to make Au sealings soft.



# Chapter 3

## Characterisation of $\text{Ce}_{1-x}\text{Pr}_x\text{O}_{2-\delta}$

### 3.1 Introduction

This chapter contains the results from the measurements on cone-shaped electrodes of  $\text{Ce}_{0.9}\text{Pr}_{0.1}\text{O}_{2-\delta}$  (CPO10) and  $\text{Ce}_{0.8}\text{Pr}_{0.2}\text{O}_{2-\delta}$  (CPO20) and the XANES measurements. The material has both ionic and electronic conductivity and the Pr ions can easily change oxidation state between +3 and +4. Therefore it might have some catalytic properties, and it is interesting to see how the material reacts to changes in atmospheres and how the cone electrodes performs electrochemically.

The XANES measurements can show whether there is a change in oxidation state both for Ce and Pr, when the atmosphere is changed. Changes in the oxidation state might give an indication of whether the CPO has any catalytic activity to NO reduction/oxidation.

The cone-shaped measurements can also provide some information on the catalytic processes taking place by interpretation of the OCV. Further the ratios of the cathodic current densities obtained in air and 1 % NO in Ar can provide information on the selectivity of the material. Using the cone-shaped electrodes ensures that the results are not influenced by the micro structure of the electrodes.

### 3.2 Experimental

Powders of CPO10 and CPO20 was synthesised with the GNP synthesis [80]. The powders were ball milled and then calcinated for 6 hours at 1000 °C. X-ray powder diffraction on a Theta-Theta STOE diffractometer confirmed that the powders were single phased and had fluorite structure.

#### Cone measurements

The powder was pressed into pellets of cylindrical shape with a diameter of 1.2 cm and these pellets were sintered at 1550 °C. The sintered pellets were examined with X-ray diffraction and the structure was determined to be fluorite, so the high sintering temperature did no cause any phase change. The pellets mechanically shaped into cone shape.

The cones were mounted in the cone setup, as shown in figure 2.2. The tip of the cone is in contact with a YSZ plate. The small contact area between the cone and YSZ plate is the TPB, with electrolyte (YSZ), electrode (Cone) and the gas phase around with NO molecules. The contact area can be found from the  $R_s$  value from the impedance measurements, as shown in equation (3.1) (Newman's formula [83]). Equation (3.1) is based on the assumption that the contact area is circular and  $r$  is the radius of this circle.  $\sigma$  is the conductivity of YSZ. The contact area is used for calculating the current densities for the cyclic voltammograms.

$$r = \frac{1}{4\sigma R_s} \quad (3.1)$$

Electrochemical measurements used were EIS and CV, and before every measurement the OCV was monitored for two hours in order to establish equilibrium. Further experiments were performed on the CPO20 cone with two hours of polarisation prior to CV measurements. The measurements were done in air and in 1 % NO in Ar at 300, 400 and 500 °C. Cyclic voltammograms were recorded with the limits -1 V and + 0.4 V and step size 1 and 10 mV was used. The frequency range for the impedance measurements was 50 mHz to 1 Mhz. A Gamry Reference 600 potentiostat was used for the electrochemical measurements.

The impedance data were fitted with an equivalent circuit with a stray capacitance, the stray capacitance arising from the equipment (the Gamry). An equivalent circuit like the one shown in figure 3.1 was used to find  $R_s$  for the calculation of the contact area.

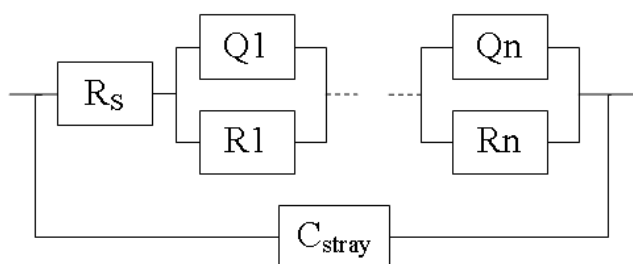


Figure 3.1: Equivalens diagram used to fit the impedance data from the cone measurements. Between 2 and 4 RQ units was necessary for an acceptable fit.

### XANES measurements

Approximately 5 mg CPO powder was thoroughly mixed with 25 mg boron nitride in an agate mortar and then pressed into a thin disk.

A home made flow cell was used for the in situ measurements [81]. The pellets were carefully placed in a holder inside a glass tube with Kapton windows for the x-ray. The glass tube was placed inside a tubular furnace, which allowed the temperature to be controlled, and the sample could be heated up to 497 °C. The atmosphere in the glass tube could be changed between air and 1 % NO in Ar. The massflow

controllers from Bronkhorst ensured a flow of 100 mL/min.

XANES transmission mode measurements were performed the beam line C at HASYLAB/DESY with a Si (111) monochromator. A chromium metal foil was used as a reference, with an K edge energy of 5989 eV, close to the 5964 eV of the  $L_3$  edge of Pr.

The  $L_3$  edge was chosen for both Ce and Pr, as the  $L_1$  and  $L_2$  edges had to low intensity and the K edge was out of reach with an edge energy of 41991 eV. In the region around the Ce and Pr  $L_3$  edges steps of 0.2 eV was used.

Data reduction was done by normalising the spectra; first a linear preedge background was subtracted and then the spectra were normalised to unity.

ATHENA from the IFEFFIT program package was used for analysing the XANES spectra [86].

Spectra were recorded at room temperature in air and every 30 minutes while heating. The atmosphere was changed from air to 1 % NO in Ar at 400 and 497 °C.

## 3.3 Results

### 3.3.1 Cone measurements

#### OCV

The OCV measured in the temperature range of 300 to 500 °C for 1 % NO in Ar atmosphere can be seen in figure 3.2. The trend is that the OCV value decreases in 1 % NO in Ar with increasing temperature.

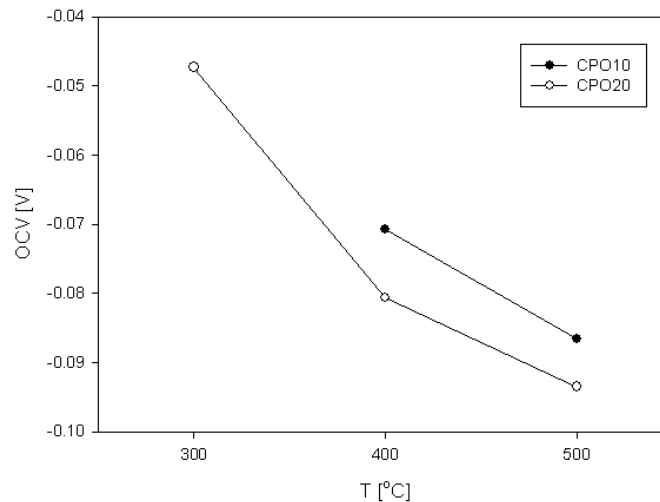


Figure 3.2: OCV for the CPO10 and CPO20 cone in 1 % NO in Ar in the temperature range 300 to 500 °C.

**CV**

Generally CPO10 has higher current densities in NO than in air at high temperatures, see figure 3.3 for an example. Whereas the opposite is seen for the CPO20 except for the measurement at 500 °C.

The ratio between  $i_{NO}$  and  $i_{air}$  at maximum cathodic current is shown in figure

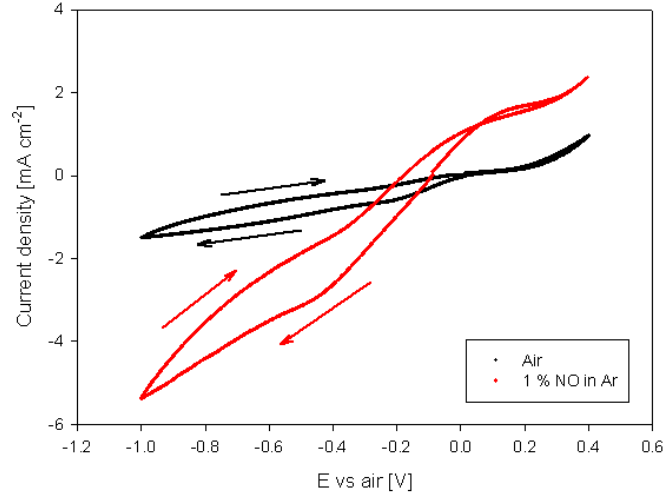


Figure 3.3: Cyclic voltammogram for the CPO10 cone in air and 1 % NO in Ar at 500 °C with a scanrate of 1 mV/s.

3.4. The apparent selectivity of CPO10 and CPO20 seems to increase with temperature, except that the datapoint at 400 °C seems to be a bit off.

The order of the measurements was: first the CPO20 cone measurements in air in

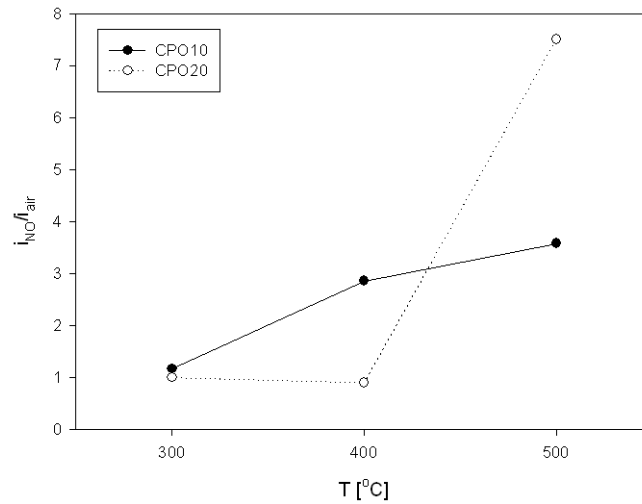


Figure 3.4: Ratio between  $i_{NO}$  and  $i_{air}$  in the temperature range of 300 to 500 °C.

temperature range 300 to 400 °C, in 1 % NO in Ar in temperature range 300 to



400 °C. Then the same measurements were done on the CPO10 cone, followed by measurements at 500 °C in air and in 1 % NO in Ar. Finally the measurements for the CPO20 cone was repeated in the temperature range of 300 to 500 °C.

It was observed that the new datapoint at 400 °C for selectivity of the CPO20 electrode seemed to fit better with the trend, see figure 3.5. The change in the ap-

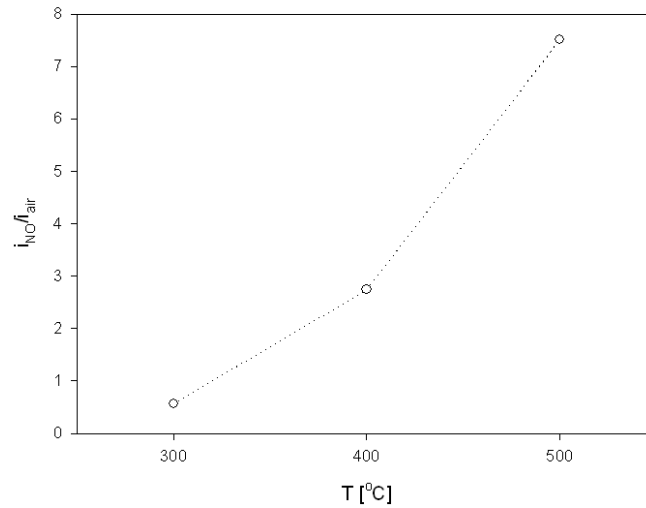


Figure 3.5: Ratio between  $i_{NO}$  and  $i_{air}$  for the second series of measurements on the CPO20 cone in the temperature range of 300 to 500 °C for CV measurements with a scan rate of 1 mV/s.

parent selectivity for the datapoint at 400 °C for the second series of measurements of the CPO20 cone could be due to changes in stoichiometry from either heating or previous polarisations. Therefore a series of cyclic voltammograms were recorded immediately after polarising the CPO20 cone. The maximum anodic current in 1 % NO hardly changed, while the maximum cathodic current was highly dependent on the previous polarisation. The cathodic current density was higher for CV measurements following a positive polarisation, while the opposite was seen for CV measurements after a negative polarisation of the CPO20 cone, see figure 3.6. The cathodic maximum current density after polarisation with +0.4 V is 12 % higher than the current density achieved without any polarisation at 300 °C, correspondingly  $i_{NO,max}$  is 14 % lower after polarisation with -0.4 V. The effect of an earlier polarisation decreases with temperature, and at 500 °C only changes of 1-2 % in current density is seen.

### 3.3.2 XANES

Heating from room temperature to 497 °C in air had no effect on the oxidation state of neither Ce or Pr in CPO10 and CPO20. The oxidation states of Ce and Pr are very stable in that temperature region for CPO10 and CPO20.

The Ce ion did not change oxidation state when varying the atmosphere between air and 1 % NO in Ar at 400 and 497 °C.

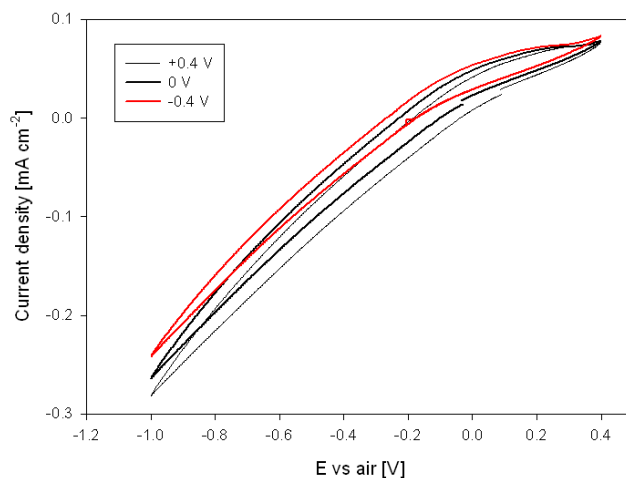


Figure 3.6: Cyclic voltammograms recorded after polarisation with +0.4, 0 and -0.4 V for two hours in 1 % NO in Ar for the CPO20 cone in at 300 °C with a scan rate of 1 mV/s.

Likewise the Pr L<sub>3</sub> edge did not shift, when changing the atmosphere at 400 °C. But at 497 °C the Pr L<sub>3</sub> edge was shifted slightly to lower energies for both CPO10 and CPO20. The shift in edge of the CPO20 sample can be seen in figure 3.7.

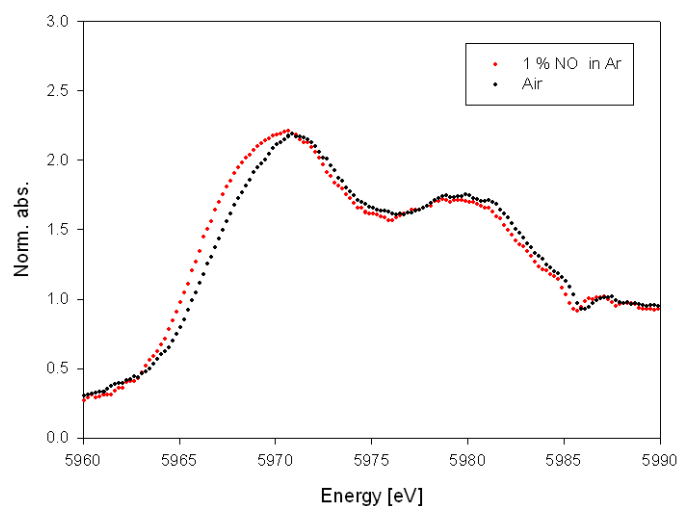


Figure 3.7: XANES spectra of Pr L<sub>3</sub> edge in different atmospheres for CPO20.

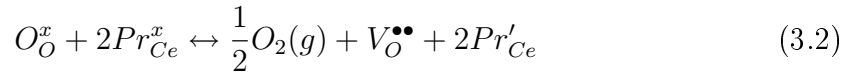
This indicates that some of the praseodymium ions were reduced in the 1 % NO in Ar gas, changing their valence from +4 to +3. For the CPO20 the average shift of the edge is approximately 0.5 eV, while it is only around 0.2 eV for the CPO10.

## 3.4 Discussion

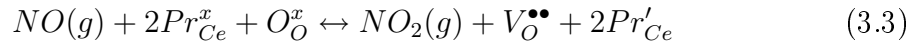
### 3.4.1 Surface reactions

The XANES measurements show that the Pr ions are getting reduced due to the change in atmosphere for the measurements at 497 °C, while the oxidation state of the Ce ions is stable. The change in edge energy for CPO10 is less than for CPO20, and this is not what was expected. The change in energy should not be dependent on the concentration of Pr ions, so this means that a smaller portion of the ions in CPO10 is reduced than for CPO20.

A negative OCV is expected when there is air at the reference electrode and the cone electrode is in 1 % NO in Ar. The  $pO_2$  can be calculated from the Nernst equation with the OCV value in 1 % NO in Ar. This value does not show the actual  $pO_2$ , but what the electrode feels is present electrochemically, as there can be other species from the nitrogen oxide system present, which can react electrochemically with the electrode. The virtual  $pO_2$  values calculated from OCV at 500 °C for CPO10 and CPO20 in 1 % NO in Ar is 0.001 atm and 0.0008 atm respectively. So the CPO20 electrode react as if there were less  $O_2$  present, than the CPO10 electrodes. Although it is the same atmosphere, 1 % NO in Ar. The same is seen for the XANES measurements, a larger fraction of  $Pr^{+4}$  ions are reduced to  $Pr^{+3}$  for the CPO20 sample than the CPO10. This could be due to surface reactions. The fluorite structure could loose  $O_2$  due to the low oxygen pressure as shown in equation (3.2)



Alternatively something else is being oxidised - the NO molecules. NO could be oxidised to either  $NO_2$  as in equation (3.3) or nitrates on the surface of the CPO.



When the atmosphere was changed back from 1 % NO in Ar to air again the  $Pr_{3d}$  edge resumed its original position in the XANES measurements - the Pr ions were reoxidised.

As the OCV values at 500 °C for CPO10 and CPO20 indicate different levels of  $pO_2$  despite both measurements in 1 % NO in Ar, then equation (3.2) cannot be the only reaction going on here. The difference in  $pO_2$  is not large, but it follows the same trend over the temperature interval of 300 to 500 °C, with lower values for CPO20 than CPO10. Further it fits with the XANES measurements. The results from the cone measurements and the XANES measurements indicate that CPO10 is less active than CPO20 in oxidising NO.

### 3.4.2 Selectivity

The current ratio of the maximum cathodic current at -1 V vs air ( $i_{NO}/i_{air}$ ) for CPO10 and CPO20, see figure 3.5 and 3.6, shows that generally the electrodes have higher current density in 1 % NO in Ar than air, when the temperature increased. This is the opposite of what is seen for the composite electrodes see chapter 5. .

CPO20 has higher selectivity than CPO10 at 500 °C, while the opposite is the case at 300 and 400 °C.

# Chapter 4

## LSM and ceria doped symmetrical cells

This chapter is the manuscript "Characterisation of  $(\text{La}_{1-x}\text{Sr}_x)_s\text{MnO}_3$  and doped ceria composite electrodes in  $\text{NO}_x$  containing atmosphere with impedance spectroscopy" which will appear in Journal of Electrochemical Society.

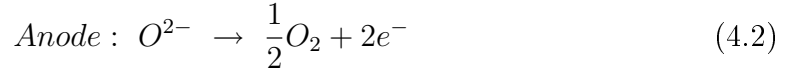
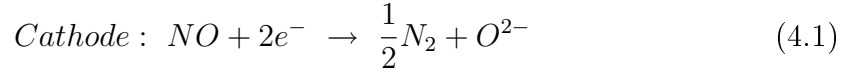
### Abstract

This study uses electrochemical impedance spectroscopy (EIS) to characterise composite metal oxide electrodes in atmospheres containing  $\text{NO}$ ,  $\text{NO}_2$  and  $\text{O}_2$ . Symmetrical cells with electrodes of  $(\text{La}_{1-x}\text{Sr}_x)_s\text{MnO}_3$  ( $(x, s) = (0.15, 0.9)$  and  $(0.5, 0.99)$ ) and doped ceria -  $\text{Ce}_{0.9}\text{Gd}_{0.1}\text{O}_2$  and  $\text{Ce}_{1-x}\text{Gd}_x\text{O}_2$  ( $x = 0.1, 0.2$ ) - were subjected to EIS, while varying the temperature (300 to 600 °C), the composition of the atmosphere and the gas flow. The impedance spectra were fitted to equivalent circuits, and common arcs were identified and sought related to physical and chemical processes.

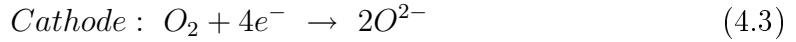
The electrodes had much lower polarisation resistance ( $R_p$ ) when  $\text{NO}$  or  $\text{NO}_2$  was present in the atmosphere at low temperatures (300-400 °C) than in air. The impedance spectra for electrodes in 1 %  $\text{NO}$  in Ar were dominated by a low frequency arc at high temperatures (500 - 600 °C). This arc seems to be a type of conversion arc, related to a gaseous intermediate - possible  $\text{NO}_2$  - formed from  $\text{NO}$ , through which the electrode reaction occur. Indications were found that the electrodes are not electrochemically active towards  $\text{NO}$  around open circuit voltage (OCV).

## 4.1 Introduction

Nitrogen oxides are formed from  $O_2$  and  $N_2$  at the high temperatures found in combustion engines.  $NO_x$  are poisonous for human beings and a threat to the environment. Therefore great focus is on detecting and removing  $NO_x$ .  $NO_x$  can be reduced electrochemically as first shown by [19], and since then several studies have been done concerning electrochemical removal of  $NO_x$  [22] [23] [27]. Electrochemical removal of  $NO_x$  has been suggested as a method to remove the  $NO_x$  from the exhaust stream of a diesel engine where oxygen is present [18]. NO reduction after removing  $O_2$  by electrochemical pumping was demonstrated by Hibino *et al.* [26]. A solid oxide electrochemical cell with composite oxide electrodes can be used for removal of  $NO_x$ . The idea is that  $NO_x$  is reduced at the cathode, (4.1), resulting in the formation of  $N_2$ , while the oxide ions are transported through the electrolyte to the anode, where  $O_2$  is formed (4.2).



The oxygen reduction reaction (4.3) is a competing reaction, which also can take place at the cathode.



This work is part of a technological explorative investigation of the  $(A_{1-x}A'_x)_{1-\delta}B_{1-y}B'_yO_3 - M_{1-z}^hM_z^dO_2$  perovskite electrode system with respect to possibilities of finding combinations that might work as NO reduction electrodes. A and A' are large A-site ions in the  $ABO_3$  type perovskite,  $M^h$  and  $M^d$  are the metal host ion and dopant ion in the  $MO_2$  type fluorite.

Two sets of relative different materials within the same family were studied,  $(La_{0.5}Sr_{0.5})_{0.99}MnO_3$  (LSM50) and  $Ce_{1-x}Pr_xO_2$  (CPO) ( $x = 0.1, 0.2$ ) and  $(La_{0.85}Sr_{0.15})_{0.9}MnO_3$  (LSM15) and  $Ce_{0.9}Gd_{0.1}O_2$  (CGO). Both LSM15 and LSM50 are A-site substoichiometric resulting in extra  $MnO_x$ , but the LSM15 have 10 times more than the LSM50. Thus, this testing of different sets of composite electrodes that have potential for activity towards the electrochemical removal of NO is a kind of digging down into different sites in a corner of the vast field of the  $ABO_3$ - $MO_2$ -composite electrodes. It was decided to investigate the composite electrodes of LSM and CGO or CPO. These materials were chosen because various perovskites have been tested for activity toward decomposition of  $NO_x$  [55][56][58] and electrochemical reduction [27], among them  $La_{1-x}Sr_xMnO_3$  (LSM) showed activity.  $Ce_{1-x}Pr_xO_2$  (CPO) can conduct both electrons and oxide ions and the praseodymium ions in CPO can easily change oxidation state between +3 and +4, which might provide some catalytic activity for the reduction reaction.

In the field of electrochemical removal of  $NO_x$  Reinhardt *et al.* [22] used EIS on

tip electrodes to determine the number of time constants, i.e. number of limiting processes. EIS has also been used for characterisation of electrochemical cells for  $\text{NO}_x$  detectors [87][88]. Further AC measurements on symmetric electrochemical cells have earlier been used in cells for  $\text{NO}_x$  detection [89][90].

EIS has been used intensively to characterize electrodes and to obtain knowledge about kinetics in the field of solid oxide fuel cells (SOFC). Separation of the arcs which compose the impedance spectra can give valuable information about how adsorption takes place, electrode structure and current transfer etc.

Symmetrical cells in a one atmosphere setup were used for the characterisation, the gas composition was not monitored. The EIS measurements were done in the temperature range of 300 to 600 °C. The range of 300 to 400 °C corresponds well with the temperature in the actual exhaust of a diesel engine. Information about the temperature dependence, can be found by measure over a broader temperature range, so the temperature range was expanded to 600 °C. Also at 600 °C it is possible to compare results for measurements in air with existing results, as this is in the low temperature end of SOFCs temperature operating range.

## 4.2 Experimental

The electrochemical experiments were carried out using a symmetrical cell, which is a two electrode cell where the electrodes on both sides of the cell are identical.

The powders of  $(\text{La}_{0.5}\text{Sr}_{0.5})_{0.99}\text{MnO}_3$  (LSM50),  $\text{Ce}_{0.9}\text{Pr}_{0.1}\text{O}_2$  (CPO10) and  $\text{Ce}_{0.8}\text{Pr}_{0.2}\text{O}_2$  (CPO20) were synthesised by the glycine nitrate combustion synthesis [80], and the LSM50 powder was made with 1% Mn in excess. The Mn, La, Pr and Sr nitrates was from Alfa Aesar and the Ce nitrate from Johnson Matthey. The CPO powders were calcined at 1000 °C for 6 hours, while the LSM50 powder was calcined at 1200 °C for 50 hours. X-ray powder diffraction with a theta-theta STOE diffractometer was used to determine if the powders were single phased.

The CGO10 powder was a commercial product from Rhodia, and the  $(\text{La}_{0.85}\text{Sr}_{0.15})_{0.9}\text{MnO}_3$  (LSM15) powder was from Haldor Topsoe A/S.

A sintered tape of  $\text{Ce}_{0.9}\text{Gd}_{0.1}\text{O}_2$  (CGO10) with a thickness around 160  $\mu\text{m}$  was used as an electrolyte. A slurry with CGO powder and binder was tape casted, and the tape was subsequently sintered at 1150 °C. The electrodes were screen printed on both sides of the 50 x 50 mm CGO10 tape and the cells were sintered at 1050 °C for 2 hours.

Terpineol based screen printing pastes were made by mixing the powders with a solvent, milling on a planetary mill and finally adding binder. The particle size distribution was measured with a Beckman Coulter Particle Size Analyzer, and the pastes were milled until a  $d_{90}$  value below 7  $\mu\text{m}$  was obtained for all of them.

Afterward the big cells (50 x 50 mm) were cut into small cells of approximately 6 times 6 mm with a diamond tool.

Three different electrodes were prepared; one with 50 wt. % LSM15 and 50 wt. % CGO10 (LSM15/CGO10), another with 50 wt. % LSM50 and 50 wt. % CPO10 (LSM50/CPO10) and the last with 50 wt. % LSM50 and 50 wt. % CPO20

(LSM50/CPO20).

The electrodes of the symmetrical cells were examined with focused ion beam-scanning electron microscopy (FIB-SEM) in order to view the micro structure. The sample was prepared by mounting in Cold Mount<sup>TM</sup> resin supplied by Structure Probe Inc. at atmospheric pressure. A Zeiss XB 1540 CrossBeam<sup>TM</sup> was used for both SEM imaging and FIB milling. The accelerating voltage was 10 kV and the SE2 detector of the XB 1540 was used. Furthermore the polished cross section of cells mounted in epoxy was examined in a Hitachi Tabletop Microscope (TM1000). Gold paste with 20 wt. % carbon was painted on the sides of the symmetrical cell as a current collector. The carbon was added as a pore former.

The symmetrical cells were placed in a setup as shown in figure 4.1. Gold wires and gold net are used as current collectors. Platinum cannot be used, because it is catalytic active in the process of decomposition of nitrogen oxide.

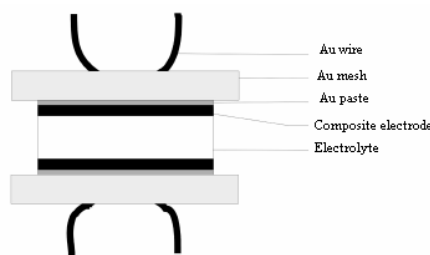


Figure 4.1: A sketch of the symmetrical cell setup.

Four small cells with similar electrodes were placed in an oven with a controlled atmosphere. The setup was heated to 850 °C to remove the carbon in the gold paste and to make the gold paste come into contact with the gold net and the electrodes, and this was done in air.

Afterward electrochemical measurements were done at 600, 500, 400 and 300 °C in different atmospheres; air, 1 % NO in Ar, 1 % NO<sub>2</sub> in Ar and 0.75 % NO + 5 % O<sub>2</sub> in Ar. Furthermore the LSM50/CPO20 electrodes were subjected to EIS in 1 % N<sub>2</sub>O in Ar at 500 and 600 °C. A gas flow of 100 mL per min was used unless anything else is stated.

The 350-S flue gas analyzer from Testo was used to measure the ratio between the concentration of NO and NO<sub>2</sub> at 400, 500 and 600 °C in the outlet gas from the setup. The gas analyser uses electrochemical sensors to detect NO and NO<sub>2</sub>.

A solartron 1260 frequency response analyser was used for EIS characterisation of the cells. This was done at OCV and with an amplitude of 36 mV RMS over the cell and an internal resistor of 50 Ω. The maximum frequency was 1 MHz and the lowest 1-100 mHz.

EIS was used to test the electrodes. Electrochemical impedance measurements are done by applying an alternating voltage signal over the cell, and then measuring the current response. The AC current response will be phase shifted compared to the AC potential. The impedance is defined as the ratio between the potential and the current response. Only small potential amplitude is used, as the system response



must be linear.

The impedance of the electrode reveals to which degree it is resisting the polarisation. When the cell is polarised, current is running and the electrochemical processes can take place, i.e. the electrodes are active and surface reactions with  $\text{NO}_x$  can occur. So the impedance can tell how hindered the electrodes activity is. Usually the impedance spectrum consists of several overlapping arcs, which can be separated by fitting equivalent circuits to the experimental data.

Ideally the polarisation impedance is composed from several resistances (R) with associated capacitances (C). These RC units connected in series make up the total impedance spectrum. The constant phase elements (CPE) are used instead of capacitances, because of non ideal behavior. The impedance for the CPE can be seen in equation (4.4)[79].

$$Z = \frac{1}{Y_0(j\omega)^\alpha} \quad (4.4)$$

RQ elements replace RC, but the Q values are dependent on the frequency and cannot be directly compared to the capacitance. Therefore the equivalent capacitance (EC), also called  $C_\omega$  defined in equation (4.5), is used, which is the capacitance calculated from the summit frequency of the arc, as described in [91].

$$C_\omega = R^{(1-\alpha)/\alpha} Q^{1/\alpha} \quad (4.5)$$

When the atmosphere is changed, the  $\text{pO}_2$  changes. The LSM, CGO and CPO electrodes will desorb  $\text{O}_2$ , when the  $\text{pO}_2$  is low, thereby changing the electrodes properties. This should be taken into account when viewing the results for measurements in atmospheres with changing  $\text{pO}_2$ .

The data obtained was analysed with "Equivalent circuit for Windows" from University of Twente [92]. The simplest possible fit with series connected (RQ) elements was sought for. Then the arcs found were compared, and some trends in  $\alpha$  values (see equation (4.4)) and equivalent capacitances were recognised. Average  $\alpha$  values were found for similar arcs, and the data was remodeled holding the  $\alpha$  values constant. The EC and resistances obtained were assumed to represent real physical processes.

More than 180 impedance spectra were used for the analysis, varying the type of electrode, temperature, atmosphere, and flow rate.

## 4.3 Results

### 4.3.1 Micro structure

The thickness of the electrodes was approximately  $20 \mu\text{m}$ , and the structure was porous. The microscopy pictures showed mostly small sized particles, less than  $1 \mu$  in diameter along with some larger particles, up to  $5 \mu\text{m}$  in diameter. The focused ion beam was used to mill a trench in the cell and a picture of the cut

can be seen in figure 4.2, where both the LSM50/CPO20 electrode and some of the dense CGO electrolyte is visible. The electrode appears to be slightly disconnected from the electrolyte. This is likely an artifact from the preparation of the sample for microscopy, but it still indicate that the contact between the electrode and electrode can be improved.

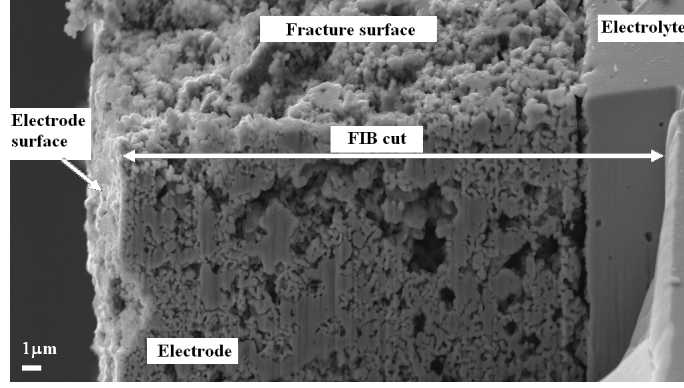


Figure 4.2: FIB-SEM image of the LSM50/CPO20 electrode and part of CGO electrolyte

### 4.3.2 Data treatment

The difference between the high and low frequency intercepts with the x-axis in the impedance spectra is the polarisation resistance of the electrodes of the cell,  $2R_p$ , as shown in figure 4.3.

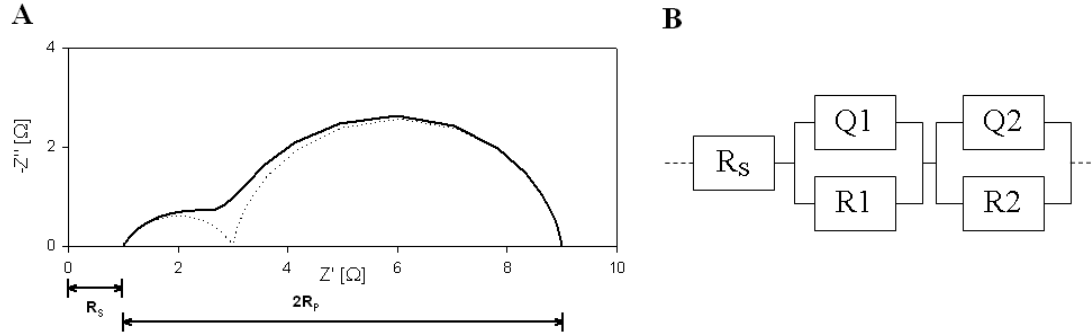


Figure 4.3: A: Sketch of impedance plot of symmetrical cell with marked  $R_p$  and serial resistance,  $R_s$ . B: Corresponding equivalent circuit.

For the three types of composite electrodes three to four arcs were identified in the impedance spectra depending on temperature, electrode composition and atmosphere.

The following steps were used to treat the large amount of EIS data.

1. An equivalent circuit was fitted to every set of impedance spectra without any restrictions on values of parameters or number of arcs.
2. Then the resulting equivalent circuits were compared. Arcs appearing in multiple impedance spectra with similar capacitances and  $\alpha$  values were identified.
3. For the identified arcs average  $\alpha$ -values were calculated.
4. The data was fitted again, this time with the identified number of arcs with average  $\alpha$  values locked.

To use this approach it is important to have a very large number of impedance spectra, both for similar cells under identical conditions, but also varying parameters such as atmosphere, temperature and flow rate. This is necessary because there are many free parameters in the fit, and more EIS data ensures a more realistic picture.

As an example the impedance spectra for LSM50/CPO10 electrodes in 1 % NO in Ar at 600 °C could be fitted with 2, 3 and 4 arcs. It can be determined visually from the spectrum in figure 4.4 that at least two arcs are present: a large dominating LF arc and a smaller arc at higher frequencies. By enlarging the high frequency area, figure 4.5, it is seen that for the fit with two arcs, the MF arc cannot fully model the high frequency data points. Adding another or two other arcs provides a better fit in the high frequency range and the  $\chi^2$  value decreases from 2.5E-3 to 2.1E-4 and 1.6E-4 respectively. The fit with 4 arcs only decrease the  $\chi^2$  25 % extra compared to the fit with 3 arcs, and it is seen in figure 4.5 that the main part of the extra high frequency arc is located outside of the experimental data range. Applying an extra arc will nearly always improve the fit, but does not necessarily have any physical meaning to the system. Also adding extra unknown parameters to be fitted from the same amount of data increases the uncertainty, so the smallest number of arcs should be used to get a reasonably fit. Therefore the fit with 3 arcs is assumed optimal. It is close to the experimental data both at high and low frequency, and the decrease in  $\chi^2$  by adding another arc is very little.

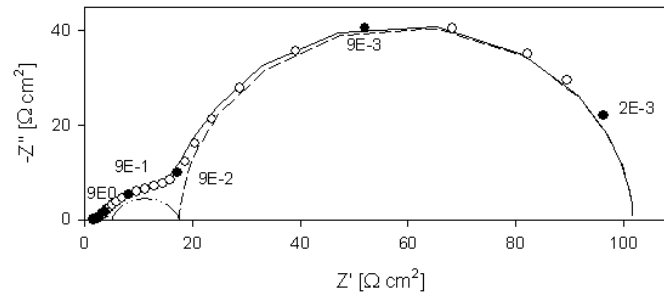


Figure 4.4: The impedance spectra for LSM50/CPO10 electrodes in 1% NO at 600 °C along with the deconvolution of the data (dotted lines). For the solid points the frequency of the data point is given in Hz.

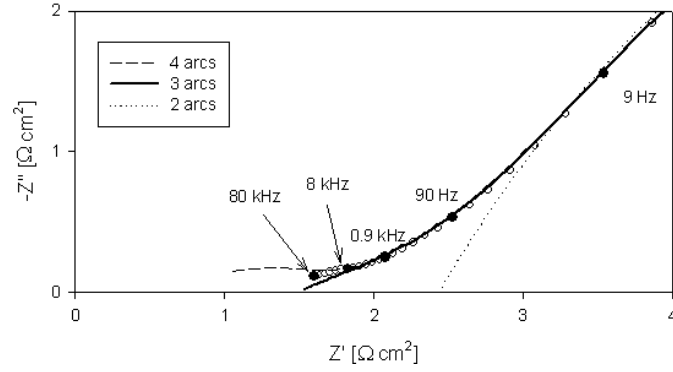


Figure 4.5: High frequency close up of impedance spectra of symmetrical cell with LSM50/CPO10 electrodes in 1 % NO in Ar at 600 °C along with the fit with 2 ( $\cdots$ ), 3 ( $—$ ) and 4 ( $- -$ ) arcs.

The average  $\alpha$  values for the LSM50/CPO electrodes was 1 for the low frequency arc, 0.7 for a middle frequency arc and 0.35 for a high frequency arc. The very low  $\alpha$  value for the high frequency arc raises the question whether it is representing a real process, or high frequency measurement errors.

Fitting the spectra with the average  $\alpha$  values did not change the  $\chi^2$  value, which indicates that the average  $\alpha$  values are correct.

The next step is to repeat the approach for sets of impedance spectra recorded at difference temperatures and for other types of electrodes, and compare the arcs identified. This may lead to sets of arcs with average  $\alpha$  values, which can be used for all impedance spectra within a group. For instance electrodes with LSM50 and CPOX ( $X = 10, 20$ ) in 1 % NO in Ar at 500 to 600 °C can be fitted with the same set of arcs.

The impedance plot for the LSM50/CPO10 cells in air at 600 °C were composed of three arcs as seen in figure 4.6. Some impedance spectra were better fitted with four arcs, such as the spectra for LSM15/CGO10 electrodes in 1 % NO<sub>2</sub> in Ar at 600 °C, see figure 4.7.

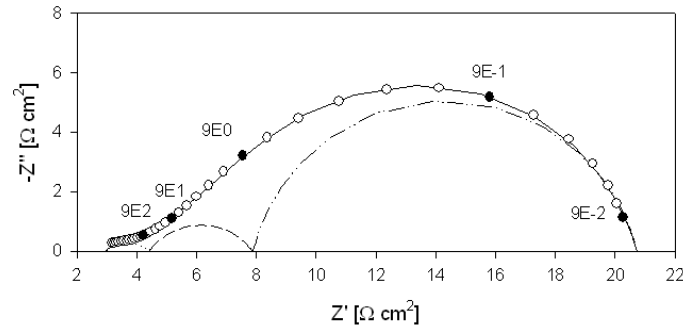


Figure 4.6: Impedance plot for LSM50/CPO10 electrodes in air at 600 °C along with the deconvolution of the data (dotted lines). For the solid points the frequency of the data point is given in Hz.

The data points measured at low frequency sometimes showed time dependence,

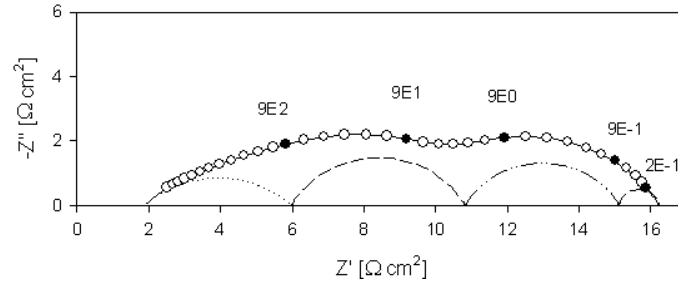


Figure 4.7: Impedance plot for LSM15/CGO10 electrodes in 1% NO<sub>2</sub> in Ar at 600 °C along with the deconvolution of the data (dotted lines). For the solid points the frequency of the data point is given in Hz.

ie. the system was not stable over the time period the measurement requires. Therefore some of these points were disregarded in the fitting process.

The apparent activation energy was calculated from the slope of the logarithm of the inverse resistance as a function of the inverse temperature. In some cases the points were very close to linearity, while in other cases the points form a curve, and there are probably two activation energies.

The overall apparent activation energy calculated for the total  $R_p$  for all the cell types can be seen in table 4.1. The apparent activation energy is the activation energy calculated from an approximate straight line disregarding the value of  $R^2$ , so in some cases it is an average of two (or more) different activation energies. The total  $R_p$  can be used as a crude estimate of the activity of the electrodes in NO<sub>x</sub>, all though it consist of resistance from several different electrode reaction steps, which likely have different activation energy.

The standard deviation between the small cells are noted along with the square of the correlation coefficient,  $R^2$ , value for the linear regression.

### 4.3.3 Air

In the impedance spectra for all the types of cells in air there were one large frequency arc and two to three smaller arcs at higher frequencies. The large arc had an EC in the range of E-04 to E-02 F cm<sup>-2</sup> depending on electrodes and temperature, see figure 4.6 for an example. Typically there were three to four arcs in the impedance spectra.

For the cells with LSM15/CGO10 electrodes there were found to be three arcs at 600 °C and four arcs at the lower temperatures. The impedance plots for cells with electrodes of LSM50/CPO10 were also composed of three to four arcs, while only three arcs were found in the impedance spectra for cells with electrodes of LSM50/CPO20 in air.

Table 4.1: The overall apparent activation energy for electrodes in air, 1 % NO in Ar, 1 % NO<sub>2</sub> in Ar and 0.75 % NO + 5 % O<sub>2</sub> in Ar over the temperature range of 300 to 600 °C in a flow of 100 mL/min together with the corresponding R<sup>2</sup> values for the fit and R<sub>p</sub> values at 600 °C.

		LSM15/CGO10	LSM50/CPO10	LSM50/CPO20
Air	E <sub>a</sub> /eV	0.88 ± 0.01	1.06 ± 0.06	1.11 ± 0.02
	R <sup>2</sup>	0.972	0.978	0.965
	R <sub>p</sub> (600 °C) /Ω cm <sup>2</sup>	8.8 ± 0.6	8.3 ± 0.9	2.9 ± 0.5
NO	E <sub>a</sub> /eV	0.55 ± 0.01	0.40 ± 0.03	0.34 ± 0.02
	R <sup>2</sup>	0.988	0.965	0.912
	R <sub>p</sub> (600 °C) /Ω cm <sup>2</sup>	31 ± 1	76 ± 3	48 ± 6
NO <sub>2</sub>	E <sub>a</sub> /eV	0.75 ± 0.01	0.88 ± 0.01	0.86 ± 0.01
	R <sup>2</sup>	0.996	0.996	0.993
	R <sub>p</sub> (600 °C) /Ω cm <sup>2</sup>	6.3 ± 0.3	5.7 ± 0.6	2.7 ± 0.1
NO + O <sub>2</sub>	E <sub>a</sub> /eV	0.97 ± 0.01	0.86 ± 0.01	0.72 ± 0.11
	R <sup>2</sup>	0.999	0.993	0.999
	R <sub>p</sub> (600 °C) /Ω cm <sup>2</sup>	7.2 ± 0.2	3.6 ± 0.5	2.4

#### 4.3.4 NO

When the cells were subjected to impedance spectroscopy in an atmosphere of 1% NO in Ar, three to four arcs were necessary to model the spectra. A large arc at very low frequencies dominated the spectra, followed by a smaller arc in the middle frequency (MF) region and some smaller arcs in the high frequency end, see figure 4.4.

The EC of the LF arc increased with the content of Pr. The LF arc did not increase as much with decreasing temperature as the MF arc. As a result the MF arc dominated at the lower temperatures, and at 300 °C the LF arc could not be separated from the spectra. The activation energy for the MF and LF arcs along with their EC for the three electrodes can be found in table 4.2. Figure 4.8 shows the resistance of the high frequency (HF), MF and LF arc for LSM15/CGO10 electrodes.

The flow of gas was changed from 100 mL/min to 10 mL/min. This had a large effect on the LF arc in the NO spectra, see figure 4.9, R<sub>LF</sub> increased with increasing flow rate. This phenomenon was observed for both the LSM50/CPO10 and LSM50/CPO20 cells in the temperature range of 400 to 600 °C.

#### 4.3.5 NO<sub>2</sub>

An equilibrium between NO, O<sub>2</sub> and NO<sub>2</sub> may be established according to equation (4.6), and due to fast kinetics at high temperatures a part of the NO<sub>2</sub> present in the inlet gas stream will be converted into O<sub>2</sub> and NO.



Table 4.2:  $E_a$  values together with the corresponding  $R^2$  values for the fit, EC values,  $R_{MF}$  and  $R_{LF}$  values at 600 °C for MF and LF arcs in 1 % NO in Ar with a flow of 100 mL/min.

		LSM15/CGO10	LSM50/CPO10	LSM50/CPO20
MF	$E_a$ /eV	$0.64 \pm 0.02$ eV	$0.67 \pm 0.03$ eV	$0.63 \pm 0.05$ eV
	$R^2$	0.990	0.977	0.977
	EC /F cm <sup>-2</sup>	8E-05 to 5E-03	3E-04 to 5E-02	5E-04 to 2E-02
	$R_{MF}$ (600 °C) / $\Omega$ cm <sup>2</sup>	$6.8 \pm 0.5$	$5.8 \pm 0.6$	$5 \pm 0.1$
LF	$E_a$ /eV	$0.34 \pm 0.02$	$0.48 \pm 0.01$	0.46
	$R^2$	0.980	0.978	0.998
	EC /F cm <sup>-2</sup>	1E-02 to 1E-01	2 to 4E-01	3 to 7E-01
	$R_{LF}$ (600 °C) / $\Omega$ cm <sup>2</sup>	$6.8 \pm 0.5$	$68 \pm 2$	$42 \pm 7$

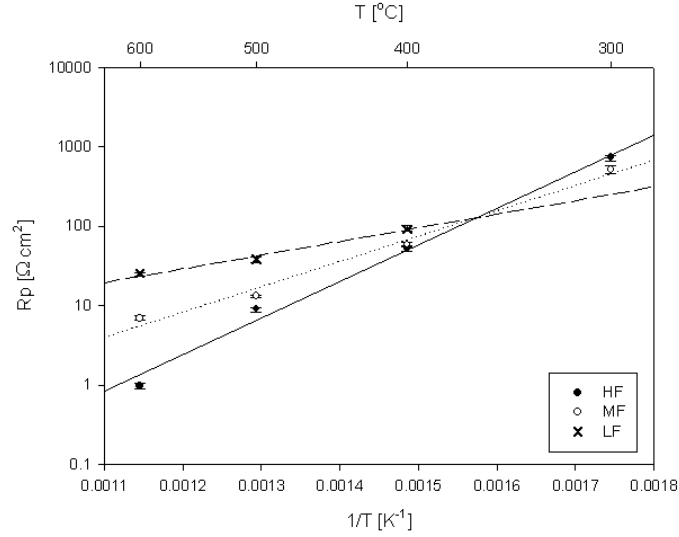


Figure 4.8: The  $R_{HF}$  (●),  $R_{MF}$  (○) and  $R_{LF}$  (x) for the LSM15/CGO10 electrodes in 1 % NO in Ar as a function of the inverse temperature.

The concentration of NO<sub>2</sub> described for the experiments in this section is thus based on the concentration in the inlet gas stream, while the actual concentration around the cell might be different. The Testo 350-S flue gas analyzer was used to measure the ratio between NO and NO<sub>2</sub> in the temperature range 400 to 600 °C to determine exactly how much NO<sub>2</sub> was present. The ratio between NO<sub>2</sub> and NO were 2.7 and 0.9 at 400 and 500 °C respectively, while it was as low as 0.7 at 600 °C.

Three to four arcs were found in the impedance plots for cells in 1 % NO<sub>2</sub> in Ar. There were two large arcs - one at middle frequency and one at low frequency, the resistance of the MF arc decreased more with temperature than the LF arc, and by 400 °C, the LF arc could not be seen anymore. If the impedance plots for LSM15/CGO10 electrodes in 1% NO<sub>2</sub> in Ar at 500 and 600 °C, figure 4.10 and 4.7, are compared then it is clear that the MF arc decreases much more with temperature than the LF arc.

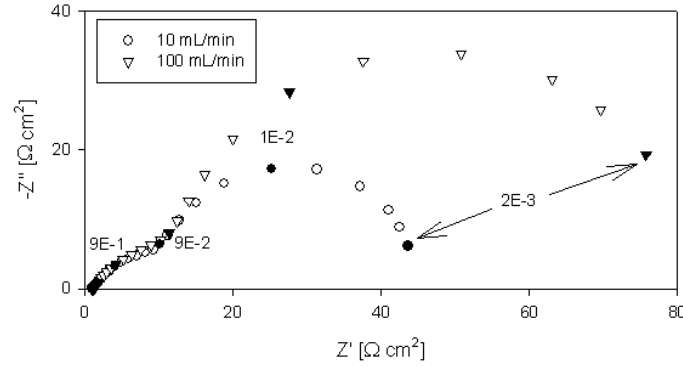


Figure 4.9: Impedance plots for LSM50/CPO20 cells in 1 % NO at 600 °C with a gas flow of 10 mL/min ( $\circ$ ) and 100 mL/min ( $\bullet$ ). The frequency of the data point is given in Hz for the solid points.

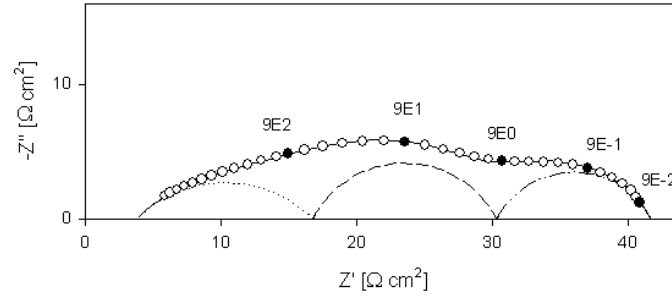


Figure 4.10: The impedance spectra for LSM15/CGO10 electrodes in 1% NO<sub>2</sub> in Ar at 500 °C along with the deconvolution of the data (dotted lines). For the solid points the frequency of the data point is given in Hz.

For the electrodes containing CPO the resistance of the LF arc did not seem to vary with temperature, as it could only be seen in the impedance spectra at 500 and 600 °C, and even at 500 °C it was mere a distortion of the spectra in the low frequency end. The EC for this arc was in the range of 4E-02 to 6E-01 F cm<sup>-2</sup> for the LSM50/CPO10 and LSM50/CPO20 electrodes. For the LSM15/CGO10 electrodes an activation energy of  $0.58 \pm 0.03$  eV was calculated for the LF arc with an EC in the range 1-2E-02 F cm<sup>-2</sup>. But in the LSM15/CGO10 electrodes there was another arc present at even lower frequency at 600 °C with EC equal to 1.9E-02 F cm<sup>-2</sup>. The activation energy for the MF arc for the three types of electrodes together with the corresponding EC range can be seen in table 4.3.

#### 4.3.6 N<sub>2</sub>O

Only the LSM50/CPO20 electrodes were subjected to EIS in 1 % N<sub>2</sub>O in Ar at 500 and 600 °C. The impedance plot were composed of 3 arcs.  $R_p$  was very large, more than 15 times larger than for electrodes in 1 % NO<sub>2</sub> at 600 °C. Changing the gas



Table 4.3:  $E_a$  values together with the corresponding  $R^2$  values for the fit, EC and  $R_{MF}$  values at 600 °C values for resistance of MF arc in 1 %  $\text{NO}_2$  in Ar

Electrode	$E_a$ eV	EC $\text{F cm}^{-2}$	$R_{MF}$ (600 °C) $\Omega \text{ cm}^2$
LSM15/CGO	$0.82 \pm 0.04$ ( $R^2=0.973$ )	9E-05 to 2E-04	$2.420 \pm 0.005 \Omega \text{ cm}^2$
LSM50/CPO10	$1.00 \pm 0.01$ ( $R^2=0.991$ )	1E-04 to 1E-02	$3.3 \pm 0.7 \Omega \text{ cm}^2$
LSM50/CPO20	$0.73 \pm 0.02$ ( $R^2=0.967$ )	6E-04 to 7E-02	$1.5 \pm 0.2 \Omega \text{ cm}^2$

flow from 100 mL/min to 10 mL/min had no effect on the impedance plot or value of  $R_p$ .

#### 4.3.7 $\text{NO} + \text{O}_2$

The electrodes were subjected to impedance spectroscopy while 0.75 %  $\text{NO}$  and 5 %  $\text{O}_2$  were present in the atmosphere.

The impedance plots are composed from three to four arcs with one large arc dominating. A smaller low frequency arc can be found at the higher temperatures.

The  $R_p$  of the electrodes were lower than the  $R_p$  for electrodes in 1 %  $\text{NO}$  in Ar in most cases, as seen in figure 4.11 and 4.12.

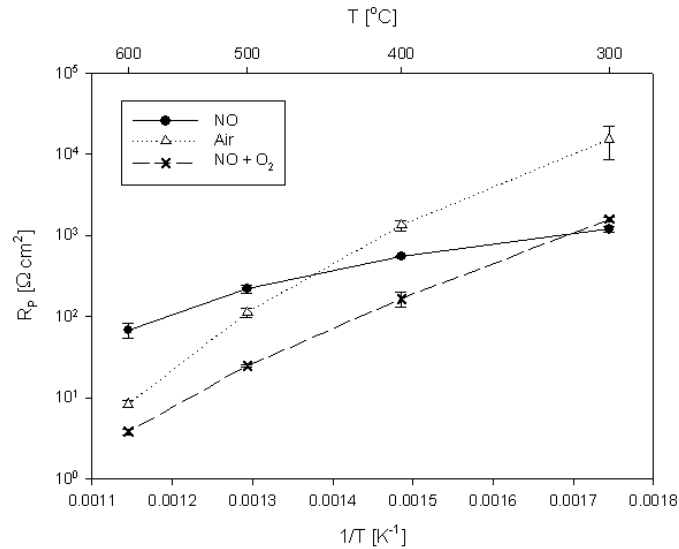


Figure 4.11: The  $R_p$  for the LSM50/CPO10 electrodes in 1 %  $\text{NO}$  in Ar ( $\bullet$ ), air ( $\Delta$ ) and 0.75 %  $\text{NO}$  and 5 %  $\text{O}_2$  in Ar ( $\times$ ) as a function of the inverse temperature.

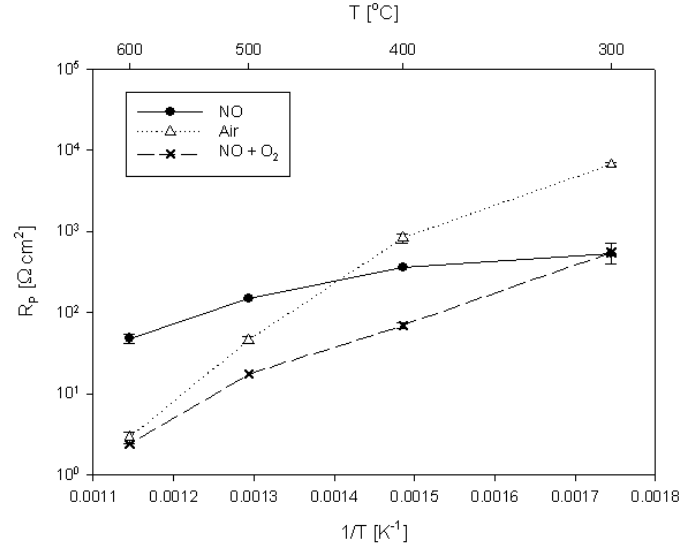


Figure 4.12: The  $R_p$  for the LSM50/CPO20 electrodes in 1 % NO in Ar (●), air and 0.75 % NO and 5 % O<sub>2</sub> in Ar (×) as a function of the inverse temperature.

## 4.4 Discussion

### 4.4.1 Matching of arcs to processes

Several distinct arcs are seen in the impedance plots, and we will try to match these arcs to processes.

Some of the arcs described in the result section are called MF and LF because of their location in the impedance plot, but the EC and summit frequency depend on the temperature. Therefore it would be more convenient to use another naming system, and we will use the same names as Jørgensen *et al.* in [93], where 5 types of arcs, A to E, are identified.

In the high frequency area of the impedance plots one or two small arcs seem to be present for all the impedance plots. They are not affected by change in atmosphere nor flow, but they do depend on temperature. Typically the activation energy is around 1 eV, and the arcs are quite depressed with  $\alpha$  values around 0.4 to 0.6. We believe these arcs to be similar to the arcs of type A and B, which cannot always be separated.

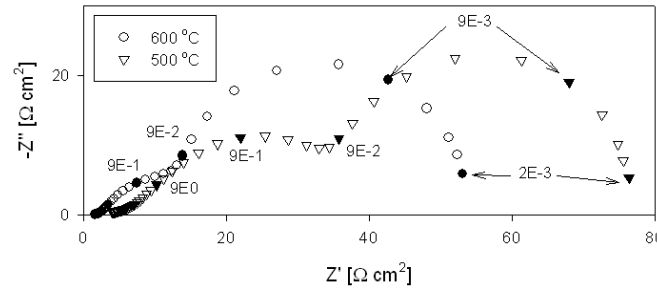
These arcs are related to transport of oxide ions across and through the LSM/doped ceria interface into the dense electrolyte [93]. A middle frequency arc is also identified in many of the impedance arcs. For the spectra recorded in air, the summit frequency of this arc is around 1 Hz for all the tested electrodes at 600 °C, which corresponds with the range given in [93] for the C arc at 850 °C. The processes of arc C are believed to be due to adsorption, surface diffusion and transfer across the triple phase boundary (TPB). Therefore the C arc is dependent on the length of the TPB. The activation energy for the C arc in air is around 1.4 to 1.6 eV for this work, which is overlapping with the values reported in [93], 1.5 to 2.0 eV. The  $\alpha$  value for the middle frequency arc is typically 0.7 to 0.8 depending on type of

electrode and atmosphere.

When the atmosphere is 1 % NO in Ar the activation energy for the C arc decreases to 0.5 to 0.7 eV, while it is higher for the CPO containing electrodes in 1 % NO<sub>2</sub> in Ar, 1.1 - 1.2 eV.

All the electrodes in NO containing atmosphere had a very large LF arc present in the impedance spectra in the temperature range of 400 to 600 °C. Especially for the electrodes containing CPO, the low frequency arc had a high EC, 2-4 E-01 F cm<sup>-2</sup> and 3-7 E-01 F cm<sup>-2</sup> for LSM50/CPO10 and LSM50/CPO20, while LSM15/CGO10 had an EC in the range 1E-02 to 1E-01 F cm<sup>-2</sup>. The  $\alpha$  value was very high - around 0.9 to 0.98, and in some cases the arc could be fitted with an RC element instead of an RQ element.

Variation of the flow rate had a large effect on the size of all the LF arcs, the resistance increased with the flow rate, as illustrated in figure 4.9.



cause of the LF arc.  $N_2O$  is often suggested as an intermediate [58], but it is not stable at high temperatures [95], and therefore it is not likely that a reaction with  $N_2O$  as the limiting intermediate is causing the LF arc at 500 and 600 °C, although it can be present as a short lived intermediate.  $R_p$  is more than 15 times larger for LSM50/CPO20 electrodes in 1 %  $N_2O$  than 1 %  $NO_2$  in Ar, and also the  $R_p$  of the electrodes in 1 %  $N_2O$  in Ar does not depend on the gas flow. This supports the idea of  $NO_2$ , and not  $N_2O$ , as an intermediate.

The hypothesis is that  $NO_2$  is formed catalytically from  $NO$  as described in equation (4.7), where LSM acts as a heterogen catalyst, afterwards the electrode reacts electrochemically with  $NO_2$ .



The LF arc is also seen in the spectra for cells in 1 %  $NO_2$  in Ar at 500 and 600 °C, but it is much smaller than for the spectra for cells in  $NO$ , which corresponds well with the higher concentration of  $NO_2$ . Also the arc does not increase with decreasing temperature for electrodes in  $NO_2$  in Ar, which is expected as the actual concentration of  $NO_2$  increases at lower temperatures.

The impedance plots for cells in an atmosphere of  $NO$  and  $O_2$  in Ar also include a small LF arc at 600 and 500 °C, and the EC values were in range of the ones for the large  $NO$  LF arc for all the electrodes. Again some  $NO_2$  must be present, due to the equilibrium between  $NO$ ,  $O_2$  and  $NO_2$ .

These results indicate that  $NO$  is not directly reacting electrochemically with the electrode around OCV, but only indirectly via the intermediate. If  $NO$  reacts electrochemically with the electrodes, then the reaction has a much higher resistance, than the reaction proceeding via an intermediate. But if the  $R$  value of this process is much larger than the one for the reaction with the intermediate, then it will not be visible in the impedance spectra, as it mainly reflects the path of the equivalent circuit with the lowest overall resistance.

The  $NO_2$  formed is quickly flushed away at the high flow rate, while at the low flow rate the concentration of  $NO_2$  close to the electrodes will be higher. This could explain why the resistance of the LF arc is higher at high flow rates than at low flow rates.

When  $NO_2$  is formed from  $NO$  on the perovskite and  $O_2$  is not present in the atmosphere, then the perovskite must slowly become under stoichiometric with respect to oxygen, see equation (4.7), and its ability to form  $NO_2$  should decrease by time. This is illustrated in figure 4.14 where the resistance of the LF arc has clearly increased in size after 5 days in  $NO$  containing atmosphere. But even after 5 days the presence of the arc means that  $NO_2$  is still being formed. This suggests that some other species than the perovskite is being reduced, and in this system, the only other candidate would be formation of  $N_2O$  from  $NO$ . A equilibrium such as (4.8) could be formed.



$O_2$  could also be a candidate for the component, which causes the LF conversion

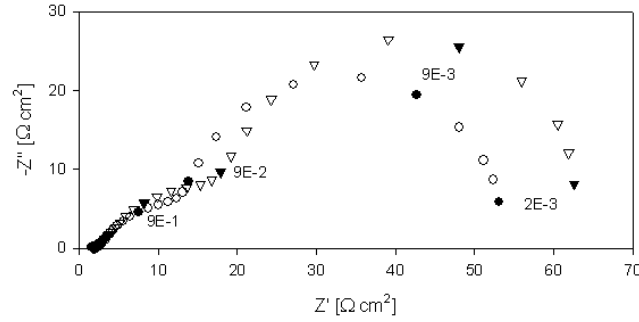


Figure 4.14: The impedance plots for LSM50/CPO10 electrodes in 1 % NO in Ar at 600 °C with a flow rate of 10 mL/min. The a plot (o) is after 2 hours in % 1 NO in Ar, while the b plot (∇) is after 5 days in 1 % NO in Ar.

arc due to low concentration in case a small leak was present in the setup.  $O_2$  is not supposed to be present in the 1 % NO in Ar atmosphere, as the setup has been leak tested before experiments. But this could explain that  $R_p$  is increasing with flow rate, the higher flow rate, the less effect a possible leak would have. The LF arc has, however, also been identified in the spectra for electrodes in 0.75 % NO + 5 %  $O_2$  in Ar, and as there is not lack of  $O_2$  in this atmosphere a diffusion arc due to lack of  $O_2$  should be unlikely. Furthermore the size of the LF arc depend quite strongly on the type of LSM - doped ceria composite, which may be explained by significant differences between the heterogenous catalytic activity for the  $NO_2$  forming processes.

#### 4.4.2 Temperature dependence

The electrodes had much lower  $R_p$  for 1 % NO or  $NO_2$  in Ar than for air in the 300 to 400 °C range. The  $R_p$  for the electrodes in air at 600 °C was lower than 1 % NO in Ar and similar to 1 %  $NO_2$  in Ar, but the activation energy for  $R_p$  in air was larger than for 1 % NO or  $NO_2$  in Ar for nearly all the electrodes examined, only exception being the LSM50/CPO10 electrodes, which had a larger  $E_a$  for 1 %  $NO_2$  in Ar than for air.

As the actual temperatures in the exhaust of a diesel engine is in the region of 200 to 300 °C it is optimal that the electrodes tested have lower resistances for  $NO_x$  than for air in the low temperature range.

The apparent  $E_a$  for electrodes in 1 % NO in Ar was much lower than for air, this is mostly due to the large LF arc dominating the spectra in NO at high temperatures. When the  $E_a$  for the middle frequency arc, type C, are compared, then the values in air are still higher than in 1 % NO in Ar. Thus the electrodes react more easily with the intermediate (or NO), at low temperatures than with  $O_2$ . This could be due to changes in the kinetics at lower temperature, as the LF arc cannot be identified in the impedance spectra at 300 °C for electrodes in 1 % NO in Ar. The low  $pO_2$  pressure could also affect the electrodes.

### 4.4.3 Addition of oxygen

When 5 %  $O_2$  was added to the atmosphere containing 0.75 % NO in Ar the  $R_p$  either decreased (high temperatures) or did not increase nearly as much as could be expected when looking at the very high  $R_p$  for air in the temperature range of 300 to 400 °C. This can be interpreted as the oxygen was not inhibiting the reaction between the electrodes and  $NO_2$ . The addition of oxygen decreases the  $R_p$  compared to the situation when only NO and Ar is present at some temperatures, as seen in figure 4.15.

The LF arc, which are usually present in the impedance spectra recorded in atmosphere containing NO is very small or missing, when 5 %  $O_2$  is present. The first part of the impedance spectra for LSM electrodes in 1 % NO in Ar and in 5 %  $O_2$  + 0.75 % NO in Ar are similar, see figure 4.15. The lack of the LF arc could be explained by the presence of  $NO_2$  from reaction between  $O_2$  and NO.

An alternative explanation could be that the electrodes becomes more efficient at reducing  $O_2$ , when NO are present, due to the formation of a more reactive oxygen surface species from the reaction between NO and  $O_2$  as suggested by Reinhardt *et al.* [22].

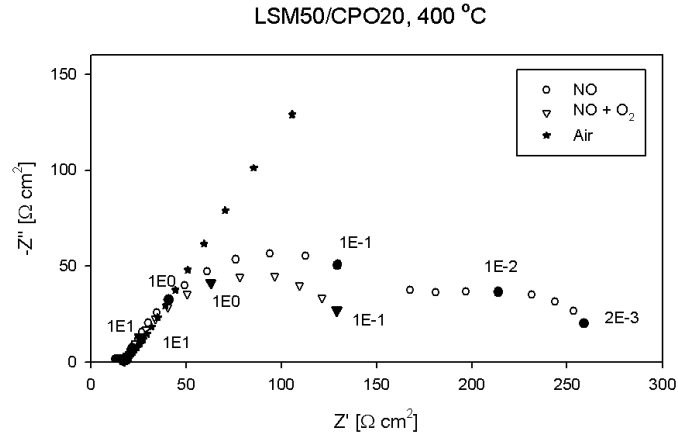


Figure 4.15: Impedance spectrum for LSM50/CPO20 cells in Air (●), 1 % NO in Ar (○) and 0.75 % NO + 5 %  $O_2$  in Ar (▽) at 400 °C. For the solid points the frequency of the data point is given in Hz.

### 4.4.4 Doping with Pr

The LF arc in NO was larger for the electrodes containing CPO and the EC was higher compared to the LSM15/CGO10 electrodes, shifting the LF arc to even lower frequencies. The summit frequency of the for LF arc at 600 °C for CPO containing electrodes was around 5 mHz, while it was around 250 mHz for the LSM15/CGO10 electrodes. This shift to higher capacitance, table 4.2, must be related to the doping of ceria with Pr. The Pr ions can change oxidation state between +3 and +4 much easier than Ce and Gd. Thus the higher capacitance may come from charge storage

in the Pr ions. This corresponds well with the LSM50/CPO20 having higher capacitances than the LSM50/CPO10, see table 4.2, which contains only half the amount of Pr ions.

The LSM50/CPO20 electrodes generally have lower  $R_p$  than the LSM50/CPO10 electrodes regardless of temperature and atmosphere, compare figure 4.11 and 4.12. Addition of Pr to ceria can increase electronic conductivity, and as CPO20 contains twice as much Pr as CPO10, that could explain the lower  $R_p$  values.

The two sets of electrodes which contained CPO10 and CPO20 respectively had lower overall apparent  $E_a$  in atmospheres containing NO compared to the LSM15/CGO10 electrodes, and also higher apparent  $E_a$  in air than LSM15/CGO10 electrodes, see table 4.1. Furthermore the electrodes with the most Pr, LSM50/CPO20, had the lowest  $E_a$  in NO and the highest  $E_a$  in air. This is due to higher  $R_{LF}$  of the CPO containing electrodes at high temperatures, where  $R_{LF}$  dominates the spectra. The LSM50/CPO10 and LSM50/CPO20 electrodes must have less catalytic activity for producing  $\text{NO}_2$  compared to the LSM15/CGO10 electrodes at the high temperatures, as the LF arc is linked to the concentration of the intermediate. This can be caused by the CPO doping, but also the variation in Sr content between LSM15 and LSM50 might play a role.

## 4.5 Conclusion

All the impedance data was fitted with equivalent circuits and between 2 and 4 arcs were identified in each impedance spectrum. Changing the atmosphere and temperature had a large impact on the appearance of the impedance spectra and on the size of the  $R_p$ . The electrodes were more active in atmospheres containing NO or  $\text{NO}_2$  at low temperature, as the  $R_p$  was much smaller than for air. Addition of 5 %  $\text{O}_2$  lowered the  $R_p$  for electrodes in 1 % NO in Ar.

The electrodes had lower apparent  $E_a$  in  $\text{NO}_x$  containing atmosphere than in air. The electrodes containing CPO had lower  $E_a$  in NO containing atmosphere than the LSM15/CGO10 electrodes. Further the electrodes of type LSM50/CPO20 had the lowest  $R_p$  when the atmosphere was 1 % NO or  $\text{NO}_2$  in Ar at the temperatures of 300 to 400 °C. The resistance was significantly lower in 1 %  $\text{NO}_2$  in Ar than for 1 % NO in Ar at higher temperatures, mostly due to the large low frequency arc seen in the NO impedance spectrum for all types of electrodes. The same type of arc was also seen in spectra for electrodes in  $\text{NO} + \text{O}_2$  and  $\text{NO}_2$ . This arc is a type of conversion arc, caused by a reaction which is limited by low concentration of intermediate reactants. The electrodes seems to be relatively inactive towards NO around OCV, when no  $\text{O}_2$  or  $\text{NO}_2$  is present at high temperatures. The intermediate is probably  $\text{NO}_2$ , as the electrodes have much lower  $R_p$  in an atmosphere containing  $\text{NO}_2$ . Therefore the reaction causing the LF arc is likely taking place through the following reaction steps; first the intermediate,  $\text{NO}_2$ , is formed catalytically from NO by LSM and then the electrode can react electrochemically with  $\text{NO}_2$ .

### 4.5.1 Acknowledgments

This work was supported financially by The Programme Commission on Sustainable Energy and Environment, The Danish Council for Strategic Research, via the Strategic Electrochemistry Research Center (SERC) ([www.serc.dk](http://www.serc.dk)), contract no. 2104-06-0011. Dr. T. Jacobsen, Technical University of Denmark, is acknowledged for fruitful discussions. P. Jørgensen, Risø National Laboratory for Sustainable Energy, Technical University of Denmark, is acknowledged for FIB-SEM imaging of the sample of symmetrical cell.



# Chapter 5

## LSM and doped ceria electrodes for NO removal

The following chapter is based on the manuscript "Electrochemical testing of composite electrodes of  $(\text{La}_{1-x}\text{Sr}_x)_s\text{MnO}_3$  and doped ceria in NO containing atmosphere" in preparation.

### Abstract

The possibility of using electrochemical cells for removal of  $\text{NO}_x$  in exhaust gas with excess  $\text{O}_2$  has been examined.

$(\text{La}_{1-x}\text{Sr}_x)_s\text{MnO}_3$  and ceria doped with Pr or Gd were selected for electrode materials and investigated in three electrode cells. The electrodes were characterised electrochemically with electrochemical impedance spectroscopy (EIS) and cyclic voltammetry (CV), and the gas composition monitored while the electrodes were polarised.

The electrodes of  $(\text{La}_{0.5}\text{Sr}_{0.5})_{0.99}\text{MnO}_3$  and  $\text{Ce}_{0.8}\text{Pr}_{0.2}\text{O}_2$  exhibit higher current densities in 0.1% NO in Ar than in Air at 300 to 400 °C during CV. This indicates some selectivity towards NO compared to  $\text{O}_2$ .

Gas conversion is observed at 600 °C when the electrodes were polarised and up to 66% of NO is removed when no  $\text{O}_2$  is present.

The electrodes can remove NO, when polarised to at least -0.6 V vs Pt/Air at 600 °C, and EIS measurements under polarisation indicate that the kinetics of the electrodes change, when the electrode potential gets below -0.6 V vs Pt/Air.

### 5.1 Introduction

Nitrogen oxides are formed from  $\text{N}_2$  and  $\text{O}_2$  present in the atmosphere at the high temperature in combustion engines. Nitrogen oxides take part in the formation of acid rain, they are dangerous to the health of humans and  $\text{N}_2\text{O}$  is a known greenhouse gas. Therefore great effort is taken in removing nitrogen oxides from exhaust gas. A three way catalytic converter can remove  $\text{NO}_x$  in engines running with a low air to fuel ratio, but this is not possible in an engine running lean due to the surplus

of  $O_2$  in the exhaust.

Pancharatnam *et al.* [19] proved that NO could be decomposed by applying a voltage over a Pt|YSZ|Pt cell. The F-centers formed on the YSZ surface were suggested as the active sites and this was later confirmed [20].

Since then many studies in electrochemical removal of nitrogen oxides have been done [22][23][27], but the great obstacle is still to achieve acceptable current efficiencies (CE) for NO reduction, while  $O_2$  is present.

The wish is to remove NO with a solid oxide electrochemical cell, by reduction of NO to  $N_2$  at the cathode, according to (5.1). Then the oxide ions are transported through the electrolyte and oxidised to  $O_2$  at the anode, (5.2). Figure 5.1 shows a sketch of this type of cell.

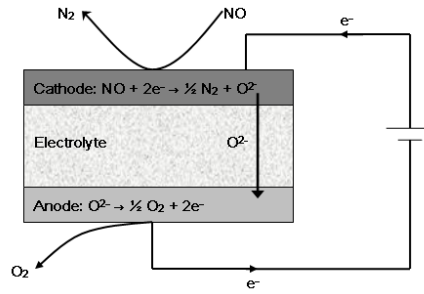
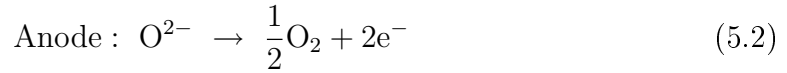
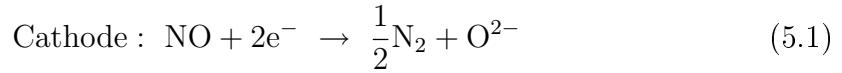
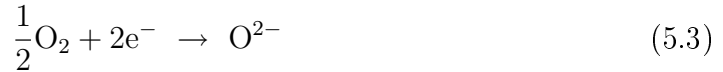


Figure 5.1: A sketch of a solid oxide electrochemical cell for removal of  $NO_x$ .



Oxygen is present in the exhaust in much higher concentrations than  $NO_x$ , and therefore the materials used for catalyst should preferable have high selectivity toward  $NO_x$ , in order to avoid wasting power for pumping  $O_2$  through the cell, i.e. the reaction of equation (5.3) should not take place at the cathode.



Several perovskites can catalyse the direct decomposition of NO: examples from the literature are  $La_{0.8}Sr_{0.2}CoO_3$  and  $La_{0.4}Sr_{0.6}Mn_{0.8}Ni_{0.2}O_3$  [55],  $La_{0.7}Ba_{0.3}Mn_{0.8}In_{0.2}O_3$  [58],  $La_{1-x}Sr_x M_{1-y}M'_yO_3$  ( $M = Co, Ni, Cu$ ) [56], and  $La_{0.8}Sr_{0.2}Co_{0.9}Ru_{0.1}O_3$  has also been used as electrode materials for electrochemical removal of NO [27].  $La_{1-x}Sr_xMnO_3$  is used for cathodes for solid oxide fuel cells (SOFCs) and has previously been used as electrode material for electrochemical removal of  $NO_x$  [27].

Ceria doped with praseodymium is a material, that has been used for a wide number of applications, such as SOFC electrodes [68], gas sensors [69] and soot oxidation [70]. The Pr ions can easily change oxidation state between +3 and +4, therefore it is possible that the material has some catalytic activity.

This work is part of an explorative investigation of the  $(A_{1-x}A'_x)_{1-\delta}B_{1-y}B'_yO_3$  -

$M_{1-z}^h M_z^d O_2$  perovskite electrode system with respect to possibilities of finding combinations that might work as NO reduction electrodes. A and A' are large A-site ions in the  $ABO_3$  type perovskite,  $M^h$  and  $M^d$  are the metal host ion and dopant ion in the  $MO_2$  type fluorite.

Two sets of relative different materials within the same family were studied,  $(La_{0.5}Sr_{0.5})_{0.99}MnO_3$  (LSM50) and  $Ce_{1-x}Pr_xO_2$  (CPO) ( $x = 0.1, 0.2$ ) and  $(La_{0.85}Sr_{0.15})_{0.9}MnO_3$  (LSM15) and  $Ce_{0.9}Gd_{0.1}O_2$  (CGO). Both LSM15 and LSM50 are A-site understoichiometric resulting in extra  $MnO_x$  being present as a third phase, and the LSM15 have 10 times more  $MnO_x$  than the LSM50. The LSM50 has a significant higher electronic conductivity (p-type) than LSM15 ( $\sigma_{LSM15} = 120 \text{ S cm}^{-1}$  and  $\sigma_{LSM50} = 500 \text{ S cm}^{-1}$  at  $600^\circ\text{C}$  [96]). CGO10 has a negligible electronic conductivity while CPO has a low but significant p-type electronic conductivity ( $\sigma_e$  for CPO20 is around  $1.6 \cdot 10^{-2} \text{ S cm}^{-1}$  at  $600^\circ\text{C}$  [67]).

This testing of different sets of composite electrodes that have potential for activity towards the electrochemical removal of NO is a kind of digging down into two different sites in a corner of the vast field of the  $ABO_3$ - $MO_2$ -composite electrodes.

## 5.2 Experimental

The composite working electrodes were screen printed onto three-electrode-cell electrolyte, which is sketched in figure 5.2. The materials were either synthesised by glycine nitrate combustion [80] ( $(La_{0.5}Sr_{0.5})_{0.99}MnO_3$  (LSM50),  $Ce_{0.9}Pr_{0.1}O_2$  (CPO10) and  $Ce_{0.8}Pr_{0.2}O_2$  (CPO20)) or commercial:  $(La_{0.85}Sr_{0.15})_{0.9}MnO_3$  (LSM15) from Haldor Topsoe A/S and  $Ce_{0.9}Gd_{0.1}O_2$  (CGO10) from Rohdia. The synthesised metal oxide powders were calcinated at  $1000^\circ\text{C}$  and  $1200^\circ\text{C}$  for the CPO and LSM50, respectively. Afterwards the powders were determined to be single phased with x-ray powder diffraction on a theta-theta STOE diffractometer.

Inks for screen printing were prepared by ball milling the metal oxide powders together with a solvent (terpineol) and a binder. The particle size distribution (PSD) of the inks were measured with a Beckman Coulter Particle Size Analyzer, and the final inks had a PSD with  $d_{90}$  smaller than  $7 \mu\text{m}$ .

The three electrode pellets were pressed from yttria stabilised zirconia (YSZ) powder and sintered. Afterwards the pellet were cut into the shape displayed in figure 5.2, and the geometry of the pellet and placement of reference electrode is based on the calculation from [84].

Table 5.1: The composition of the screen printed electrodes.

Electrode	Composition
LSM50/CPO10	50 wt.% $(La_{0.5}Sr_{0.5})_{0.99}MnO_3$ + 50 wt.% $Ce_{0.9}Pr_{0.1}O_2$
LSM50/CPO20	50 wt.% $(La_{0.5}Sr_{0.5})_{0.99}MnO_3$ + 50 wt.% $Ce_{0.8}Pr_{0.2}O_2$
LSM15/CGO10	50 wt.% $(La_{0.85}Sr_{0.15})_{0.9}MnO_3$ + 50 wt.% $Ce_{0.9}Gd_{0.1}O_2$

The perovskite are all A-site deficient, with 1 and 10% excess Mn. There are

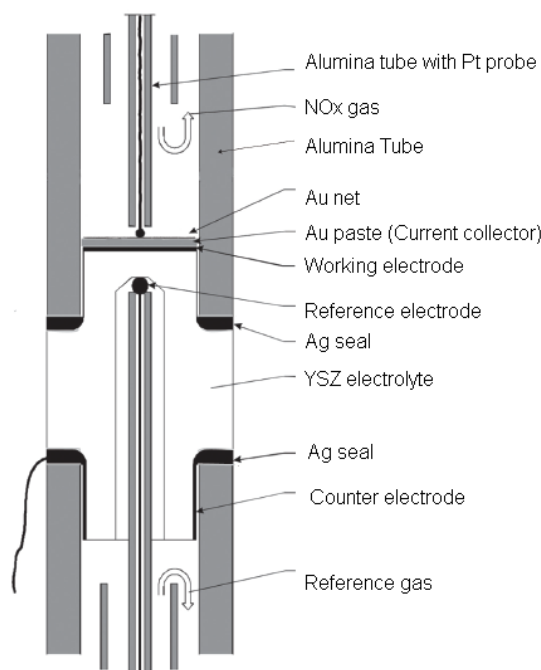


Figure 5.2: Sketch of the three electrode setup

two reasons for this approach. First of all this is done in order to prevent the formation of non-conductive phases, such as  $\text{SrZrO}_3$  and  $\text{La}_2\text{Zr}_2\text{O}_7$  at the electrolyte-electrode interface [97]. Secondly it is not possible to make completely stoichiometric perovskites, either a little A or B metal ions will always be in excess. When the perovskites are understoichiometric with respect to A, then we know that the third phase will be  $\text{MnO}_x$ .

### 5.2.1 Three electrode setup

Gold paste was painted on the working electrode as a current collector, and 20 wt.% carbon was added to the gold paste as a pore former. Furthermore gold net was placed on the gold paste as a current collector. The counter electrode was Pt paste painted on the YSZ pellet. The working electrode is round with a diameter of 7.2 mm, corresponding to an electrode area of approximately  $0.4 \text{ cm}^2$ . The three electrode cell is placed between the two alumina tubes as shown in figure 5.2, and Ag was used as sealing between the YSZ pellet and the alumina tubing. The alumina tubes are inside a quartz tube with an inert atmosphere (Ar) in a tube furnace.

The atmosphere at the anode and cathode are separated. Air was used as a reference gas at the anode compartment, while gas mixtures of Ar, NO and  $\text{O}_2$  was used in the cathode compartment. The gas flow was 5 mL/min unless other stated. The gas mixtures used was: 0.1% NO in Ar, 0.1% NO + 5%  $\text{O}_2$  in Ar and 20%  $\text{O}_2$  in Ar. Around 0.1 to 0.2%  $\text{O}_2$  was also present, detected by mass spectrometer, due to leaks in the gas inlet. The gas flows were controlled by mass flow controllers from Brooks.

The setup was placed inside a vertically mounted furnace, and the measurements

were done in the temperature range of 300 to 600 °C. A quadrupole mass spectrometer, OmniStar from Pfeiffer, was used to monitor the gas composition in the outlet gas.

The electrochemical measurements were done with a Gamry Femtostate.

Measurements were also performed using symmetrical cells as described elsewhere [98].

### 5.2.2 Electrochemical techniques

The electrodes were subjected to EIS. The lowest frequency used was 1 mHz, and the highest 100 kHz. The impedance spectroscopy was applied both at electrodes at open circuit voltage (OCV) and under cathodic potential. An RMS of 36 mV was used.

Further, cyclic voltammetry was applied to the electrodes. A sweep rate of 5 mV/s was used, and the limits were -0.8 V and 0.8 V, and in some cases -1 V and 1 V relative to the reference electrode (Pt/air). The electrodes were also subjected to chronoamperometry, where the cells were polarised for 1 or 2 hours under -0.8 to -1 V relative to the reference electrode (Pt/air).

The impedance data were analysed with the software "Equivalent circuit for Windows" from University of Twente [92].

## 5.3 Results

### 5.3.1 OCV

The OCV varied as a function of the gas flow, see figure 5.3. The lowest value for OCV obtained in an atmosphere containing 0.1% NO in Ar was around -0.155 V vs Pt/air, so the electrodes are not changing composition very much due to low pO<sub>2</sub>.

The theoretical OCV was calculated with the Nernst equation from the amount of O<sub>2</sub> present at the cathode measured by MS, assuming only equation (5.2) taking place.

### 5.3.2 EIS and equivalent circuits

The impedance spectra recorded at OCV were fitted to equivalent circuits having between 2 and 4 arcs depending on temperature and atmosphere, see figure 5.5 for an example. All the arcs were best described by an ohmic resistance in parallel with a constant phase element (CPE) as defined in equation (5.4) [79].

$$Z = \frac{1}{Y_0(j\omega)^\alpha} \quad (5.4)$$

An equivalent capacitance (EC) can be calculated for the CPE, see equation (5.5) [91].

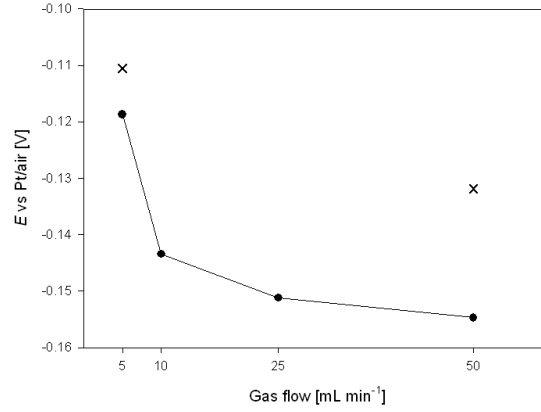


Figure 5.3: OCV (●) as a function of flow rate for the LSM50/CPO10 electrode in 0.1% NO in Ar at 600 °C. Calculated OCV (x) from  $pO_2$  using the Nernst equation with equation (5.2).

$$C_\omega = R^{(1-\alpha)/\alpha} Q^{1/\alpha} \quad (5.5)$$

The impedance spectra for the working electrodes of the three electrode pellets were fitted with the equivalent circuits found in earlier studies with symmetrical cells for the same type of electrode and experimental conditions [98].

The impedance spectra typically consists of one to two small high frequency arcs and a larger middle frequency arc. When the atmosphere is NO in Ar a low frequency (LF) arc is also found. Figure 5.4 shows the impedance spectra for the symmetrical cells in 1% NO in Ar at 600 °C. The ohmic resistance,  $R_s$ , found in the impedance

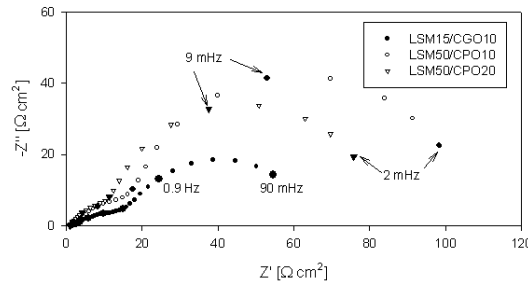


Figure 5.4: Impedance plot for symmetrical cells with LSM15/CGO10 (●), LSM50/CPO10 (○) and LSM50/CPO20 (▽) electrodes in 1% NO in Ar, 100 mL/min flow at 600 °C.

spectra for the cells was very large, around 70  $\Omega$  at 600 °C due to the part of the YSZ electrolyte between the reference electrode and working electrode, see figure 5.2. By ohmic resistance is meant resistance that is not associated with the working electrode reaction.

During polarisation of the cell the electrode potential,  $E_{\text{electrode}}$ , can be found from equation (5.6) and in figure 5.6 an example of the changes in a cyclic voltammogram

due to correction of  $R_s I$  losses is shown. When the imposed potential is -1 V vs air/Pt, the actual electrode potential is only -0.8V vs Pt/Air.

$$E_{\text{electrode}} = E - R_s I \quad (5.6)$$

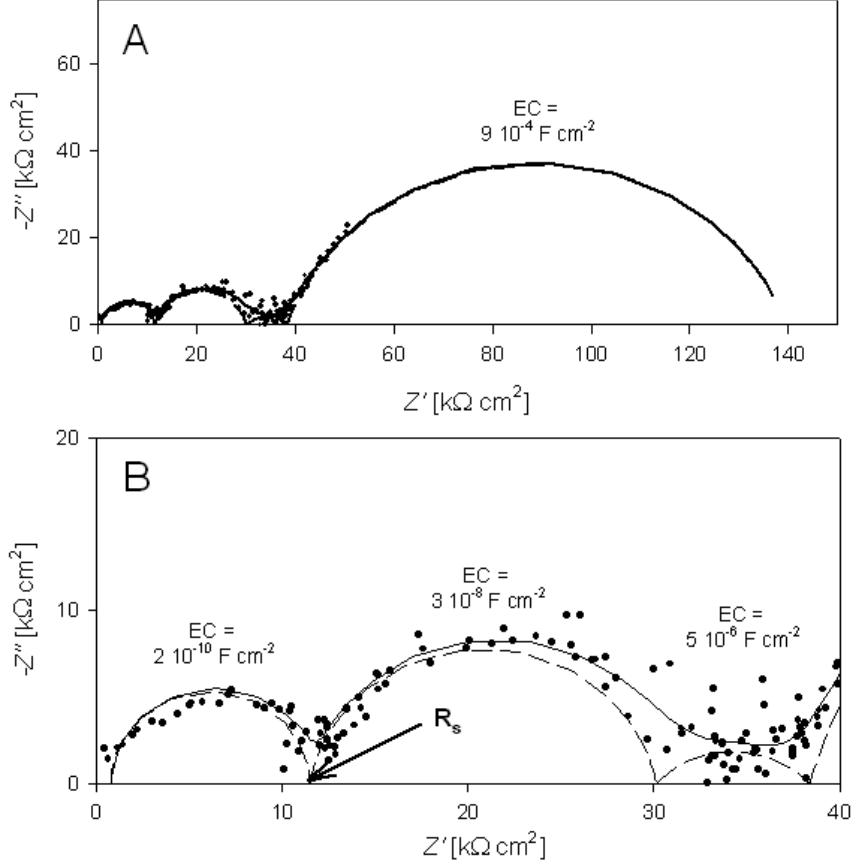


Figure 5.5: A: Impedance spectra for LSM15/CGO10 electrodes in air at 300 °C along with the deconvolution of the data. B: Magnification of the high frequency arcs marked with their  $EC$ . The summit frequency of the two high frequency arcs are: 70 kHz and 300 Hz.

The determination of  $R_s$  at 300 °C is difficult because at such low temperatures high frequency arcs can be found in the impedance spectra, which might result from the electrolyte, and therefore these resistances are a part of  $R_s$ . There is an arc with an  $EC$  around  $2 \cdot 10^{-10} \text{ F cm}^{-2}$  either resulting from grain boundaries in the electrolyte or capacitance in the equipment and another arc with an  $EC$  around  $3 \cdot 10^{-8} \text{ F cm}^{-2}$ , which results from the transfer of oxide ions into the electrolyte. The first arc is part of the  $R_s$ , while the second is not. Therefore the  $R_s$  is around  $12 \text{ kΩ cm}^{-2}$  at 300 °C as seen in figure 5.5b.

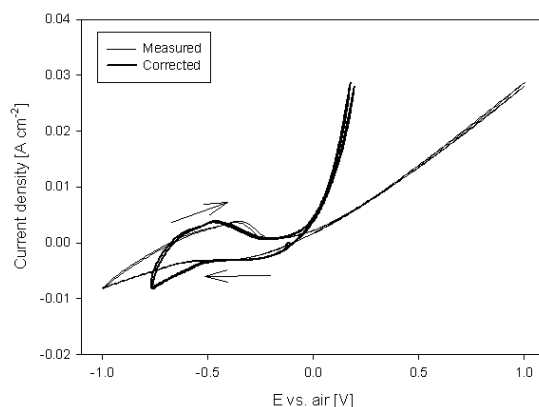


Figure 5.6: Cyclic voltammogram for LSM50/CPO10 electrodes cells in 0.1% NO in Ar at 600 °C. The thin line represents the measured data and the thick line the data with the  $R_s I$  losses have been subtracted from the potential.

### 5.3.3 Cyclic voltammetry

The current density is higher in the anodic region than in the cathodic region for all the electrodes regardless of temperature and atmosphere. Further the current density decreases with decreasing temperature.

All the electrodes had higher cathodic current densities in air than in 0.1% NO in Ar or 0.1% NO + 5% O<sub>2</sub> in Ar at 600 °C, see figure 5.7a. However, this changed when the temperature decreased. The current density for electrodes in NO + O<sub>2</sub> was higher than for electrodes in air in the temperature range of 300 to 500 °C for all the electrodes, while the current density for electrodes in NO in most cases was higher than air but lower than NO + O<sub>2</sub>, see figure 5.7b as an example. Figure 5.8 shows cathodic current densities recorded at -0.6 V vs Pt/air for the electrodes in the temperature range of 300 to 600 °C.

Peaks was observed in the voltammograms recorded at 600 °C and in 0.1% NO for all the electrodes, see figure 5.6 for an example. When the atmosphere is 0.1% NO and 5% O<sub>2</sub> in Ar or air at 600 °C, then no peaks were found. The same is seen for cyclic voltammograms recorded at lower temperature.

### 5.3.4 Polarisation of electrodes

When the electrodes were polarised it was possible to observe conversion of NO with the mass spectrometer at 600 °C for 0.1% NO in Ar for all three types of electrodes. During polarisation a decrease in the O<sub>2</sub> concentration was also seen. The conversion degree along with the current efficiency (CE) for each type of electrodes can be seen in table 5.2.

The CE is defined as the ratio between the amount of NO molecules removed as measured by mass spectrometer to the theoretical amount of NO reduced,  $I/(2F)$ , calculated from the current, see equation (5.7), assuming 2 electrons per reduced



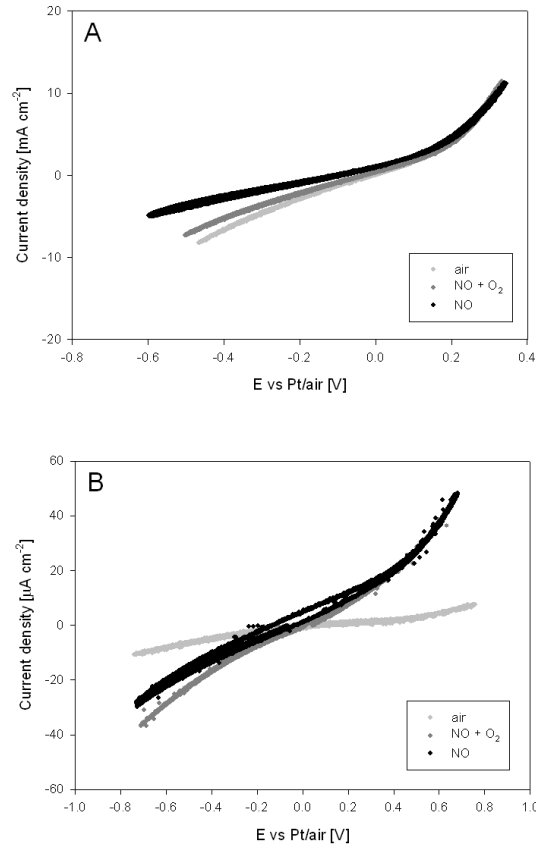


Figure 5.7: Cyclic voltammogram for LSM50/CPO20 electrodes in air (grey), 0.1% NO + 5% O<sub>2</sub> in Ar (dark grey) and 0.1% NO in Ar (black) at 600 °C (A) and 500 °C (B).

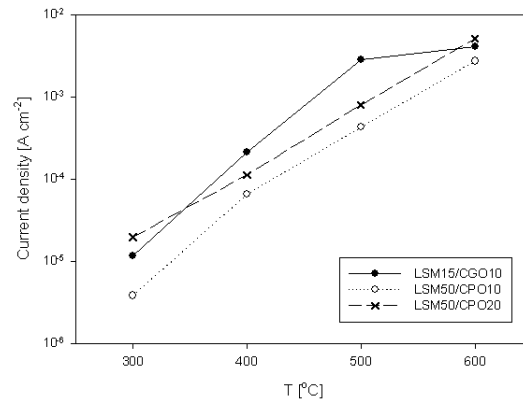


Figure 5.8:  $i_{NO}$  as a function of temperature for electrodes of LSM15/CGO10 (●), LSM50/CPO10 (○) and LSM50/CPO20 (×) in 0.1% NO in Ar at -0.6 V vs Pt/air.

NO molecules as seen in equation (5.1).

$$\text{Current efficiency} = \frac{\text{NO removed (measured)}}{I/2F} \quad (5.7)$$

Table 5.2: Degree of NO conversion and CE for polarisation with -0.8 V vs Pt/Air for electrodes in 0.1 % NO in Ar, 5 mL/min flow and at 600 °C.

Electrode	LSM15/CGO10	LSM50/CPO10	LSM50/CPO20
NO conversion	66%	53%	56%
NO removed	590 ppm	430 ppm	450 ppm
O <sub>2</sub> present	2100 ppm	1700 ppm	1800 ppm
O <sub>2</sub> removed	41%	28%	22%
N <sub>2</sub> formed	360 ppm	50ppm	250ppm
CE	18%	20%	35%
Current density	5.5 mA cm <sup>-2</sup>	3.4 mA cm <sup>-2</sup>	2.0 mA cm <sup>-2</sup>

The three types of electrodes were also polarised to -0.8 V vs air/Pt (*IR*-corrected) at 600 °C in 1000 ppm NO + 5% O<sub>2</sub> in Ar, and no gas conversion was detected with the mass spectrometer.

For the cell with LSM15/CGO10 and LSM50/CPO10 electrodes the polarisation was varied, and a decrease in NO concentration was detected from around -0.6 V vs Pt/Air over the electrode. NO conversion and CE can be seen as a function of the polarisation over the LSM15/CGO10 electrode in figure 5.9.

The decrease in the O<sub>2</sub> concentration at polarisation with potentials in the range

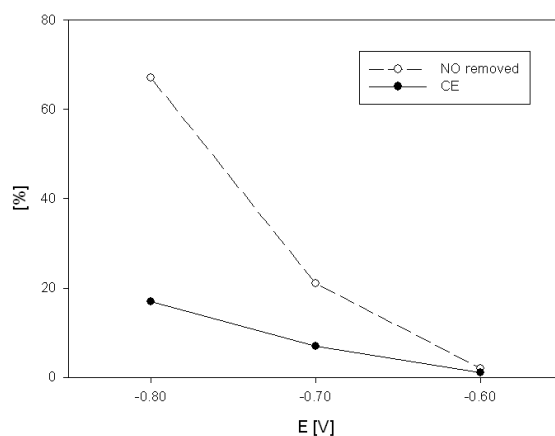


Figure 5.9: NO conversion (○) and CE (●) as a function of polarisation for LSM15/CGO10 electrodes in 0.1% NO in Ar at 600 °C.

-0.6 to -0.8 V vs Pt/Air, is around 40% independent of polarisation. The LSM50/CPO20 electrode can achieve 12% NO removal at -0.6 V vs Pt/Air, again with the amount of O<sub>2</sub> reduced being independent of polarisation. The CE also decreases from 35% to 8% in this case .

It was not possible to detect gas conversion at temperatures lower than 600 °C. The MS measurements indicated no formation of NO<sub>2</sub> or N<sub>2</sub>O.

### 5.3.5 EIS under polarisation

An LSM50/CPO20 electrode was subjected to EIS at 600 °C in 0.1% NO in Ar under polarisation at gas flow equal to 5, 10 and 20 mL/min. The polarisation resistance ( $R_p$ ) increased dramatically when the electrode was polarised, see figure 5.10.  $R_p$  also increases with increasing flow rate, which was also seen for the symmetrical cells. The most of this increase was found in the resistance of the LF arc,  $R_{LF}$ , which is believed to be a type of conversion arc caused by low concentration of an intermediate gaseous reactant [98], while the resistance of the middle frequency arc,  $R_{MF}$ , which is related to charge transfer, when NO or O<sub>2</sub> is reduced, increases much less.

The EC for the LF arc also vary with the polarisation, as seen in figure 5.11.

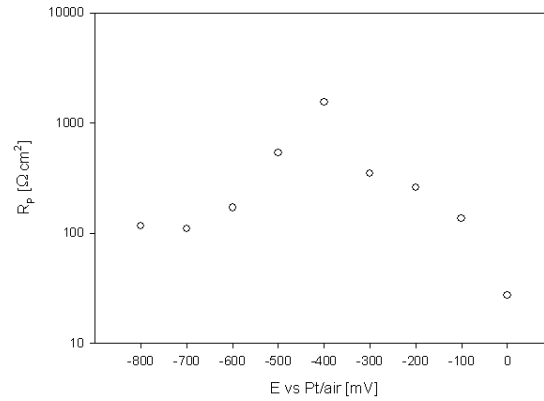


Figure 5.10:  $R_p$  for LSM50/CPO20 electrode in 5 mL/min 0.1% NO in Ar at 600 °C as a function of potential of the electrode.

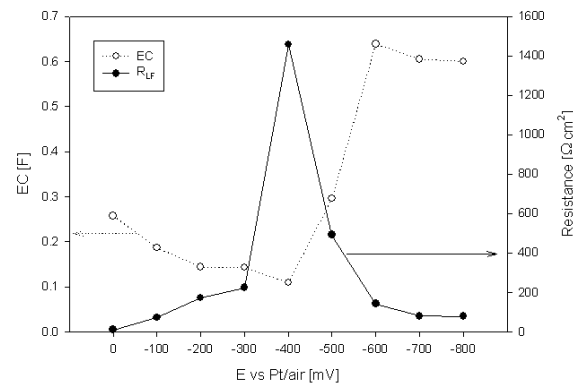


Figure 5.11:  $R_{LF}$  (●) and  $EC_{LF}$  (○) for LSM50/CPO20 electrode in 5 mL/min 0.1% NO in Ar at 600 °C as a function of potential of the electrode.

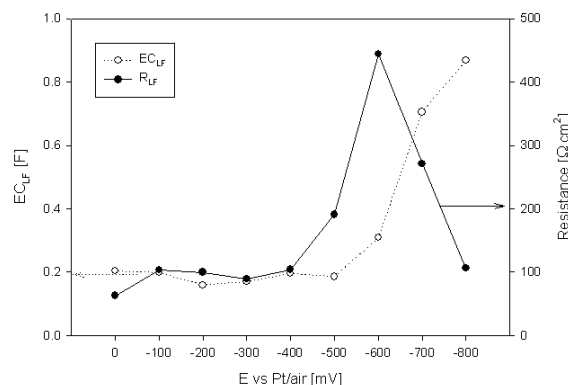


Figure 5.12:  $R_{LF}$  (●) and  $EC_{LF}$  (○) for LSM50/CPO20 electrode in 10 mL/min 0.1% NO in Ar at 600 °C as a function of potential of the electrode.

## 5.4 Discussion

### 5.4.1 Reaction mechanism

The low frequency (LF) arc in the impedance spectra is seen for electrodes in 0.1% NO in Ar, and it is dependent on gas flow and concentration of NO. This arc is likely a type of conversion arc, because of the low frequency, a high  $\alpha$  value and the dependence of flow rate [94]. It was found that this arc increases with increasing flow rate in an earlier study [98], the opposite of what would be expected for a conversion arc. Consequently the LF arc was linked to the low concentration of an intermediate, possible  $\text{NO}_2$ , which was formed catalytically by the electrode materials. By increasing the flow rate this intermediate would be flushed away, decreasing its concentration and thereby increasing the  $R_{LF}$ .

The change in OCV, when the flow rate is changed shows that electrode reactions, which are affected by flow rate, are taking place. A higher flow rate can dilute intermediates. The atmosphere at the reference electrode is air, so the difference in oxygen partial pressure explains some of the negative OCV. Oxygen could be formed at the cathode according to equation (5.2), and the  $\text{O}_2$  concentration decreases with increasing flow rate, as leaks have less influence, which could explain the more negative OCV with higher flow rate as seen in figure 5.3. Likewise it would also be possible for NO to react with the oxide ions, as in equation (5.8). This fits well with the hypothesis that low concentration of  $\text{NO}_2$ , formed by LSM is causing the LF arc, which is flow dependent.



The measured value for OCV is at more negative potential than the one calculated from  $\text{pO}_2$ . The difference between the OCV calculated from  $\text{pO}_2$  and the experimental data are small at 5 mL/min, while the difference is larger at a flow of 50 mL/min. If the difference is assumed to be caused by the reaction in equation (5.8), then the  $\text{NO}_2$  concentration must be lower at the electrode at a flow of 50 mL/min compared to 5 mL/min as the NO concentration stays the same.

$\text{NO}_2$  can be produced from  $\text{NO}$  by LSM, as shown in [71]. This could be through reaction (5.8), which the OCV measurements seems to indicate or through an equilibrium between  $\text{NO}$ ,  $\text{NO}_2$  and  $\text{N}_2\text{O}$ , as shown in equation (5.9). No  $\text{N}_2\text{O}$  was detected with the mass spectrometer, this point to equation (5.8), although it could be that  $\text{N}_2\text{O}$  is below the detectable limit (around 25 ppm).



The LF arc completely dominates the impedance spectra for the symmetrical cells in  $\text{NO}$ . This indicates that  $\text{NO}$  does not react with the electrode directly electrochemically around OCV at high temperatures. Instead the electrodes react with an intermediate, possible  $\text{NO}_2$ , formed catalytically by the electrodes. It is possible to have an equivalent circuit as the one sketched in figure 5.13, where a parallel  $RQ$  element exist corresponding to a direct reaction with  $\text{NO}$ . But if the  $R$  value of the direct reaction is much larger than the one for the reaction with the intermediate, then it will not be visible in the impedance spectra, as it mainly reflects the path of the equivalent circuit with the lowest overall resistance.

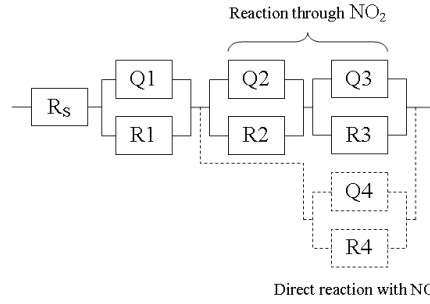


Figure 5.13: Potential equivalent circuit diagram for impedance of cells with electrodes of LSM/CPO at 600 °C in 1%  $\text{NO}$  in  $\text{Ar}$ . The parallel  $RQ$  unit drawn with dotted lines represents a direct reaction between the electrodes and  $\text{NO}$ , which have higher resistance than  $(R2Q2)(R3Q3)$ , which represents the reaction with an intermediate such as  $\text{NO}_2$ .

Figure 5.4 shows the impedance measurements on symmetrical cells in  $\text{NO}$  in  $\text{Ar}$  at 600 °C, from this the activity for the electrodes is expected to be the following:  $\text{LSM15/CGO10} > \text{LSM50/CPO20} > \text{LSM50/CPO10}$  because the LSM15/CGO10 electrodes have the lowest  $R_p$  and LSM50/CPO10 the highest  $R_p$ . This is in accordance with the conversions seen in table 5.2. So the resistance found from the impedance spectra of the symmetrical cells at OCV can predict the conversion at least at 600 °C. The LF arc dominates the impedance spectra recorded in the  $\text{NO}$  containing atmosphere, and therefore makes up most of the  $R_p$ . As this arc is connected with low concentration of an intermediate, possible  $\text{NO}_2$ , this could indicate that the the same route of  $\text{NO}$  removal takes place when the electrodes are polarised.

For the impedance measurements under polarisation, there is a sudden increase in EC, which coincides with the peak of the  $R_p$  value, see figure 5.11 and 12. The

gas conversion of NO can be detected by mass spectrometry when the electrode is polarised with -0.6 V vs Pt/air or more, this is the polarisation range where EC is stable with a value around 0.6 F. The same tendency is seen at higher flow rates, however, the peak in  $R_p$  and increase in EC is seen at the more negative potential, see figure 5.12.

The electrode does not remove NO in any detectable amounts in the polarisation range of 0 to -0.6 V vs Pt/air, but some reduction of O<sub>2</sub> does take place. The increasing value of  $R_{LF}$  in this region could be due to low concentration of O<sub>2</sub> as there is only a very small amount present. But the size of  $R_{LF}$  does also depend on electrode material, as seen in figure 5.4, which indicate that the materials catalytic properties has an effect as well. This would not be the case if the arc was caused by low concentration of O<sub>2</sub>. A parallel reaction with NO through an intermediate could also explain the increasing  $R_p$ , especially if this intermediate was a compound like NO<sub>2</sub>, which requires an oxidation of NO, as the potential of the electrode becomes more and more reducing.

The increase in EC at -0.6 V vs Pt/air over the electrode, suggests that at these negative potentials there is a different LF arc present. The reduction of NO starts at this potential and likely proceeds through another, less hindered path, this could be the direct reaction with NO with stippled lines in the equivalent diagram in figure 5.13. The reason for this could be, that the electrode composition starts changing at these low potentials.

The increase in N<sub>2</sub> corresponds with what should be expected from (5.1) for the LSM50/ CPO20 and LSM15/CGO10 electrodes, see table 5.2. This is not the case for the LSM50/ CPO10 electrodes, where too little N<sub>2</sub> is formed. The lack of formation of N<sub>2</sub> must mean that some other nitrogen containing species is formed, that could be nitrates on the surface of the electrode or NO<sub>2</sub> in the gas phase. N<sub>2</sub>O formation would be detectable in the mass spectrometer, and was not observed during the polarisation.

### 5.4.2 Selectivity

The relationship between the cathodic current densities at a similar potential in different atmospheres obtained from the cyclic voltammograms are used as a measure for selectivity. When  $i_{NO}$  is larger than  $i_{air}$  at a similar potential then the electrodes are more active towards NO<sub>x</sub> than towards O<sub>2</sub>.

Generally the  $i_{NO}/i_{air}$  ratio of the electrodes increases with decreasing temperature, indicating that the electrodes become more selective towards NO with decreasing temperature. Further the LSM50/CPO20 electrode is more dependent on temperature than the LSM50/CPO10 and LSM15/CGO10 electrodes as seen in figure 5.15. The ratio between  $i_{NO}$  and  $i_{air}$  is below or around 1 in the temperature range of 500 to 600 °C for all electrodes. A higher  $i_{NO}$  than  $i_{air}$  is seen at 300 °C, for all the electrodes and also at 400 °C for the electrodes with CPO. When O<sub>2</sub> and NO is simultaneously present in the atmosphere, then the two species will compete for reaction with the electrode. Preferable the electrodes should be selective towards NO, and if  $i_{NO+O_2}$  is larger than  $i_{air}$ , then we assume that the electrodes activity

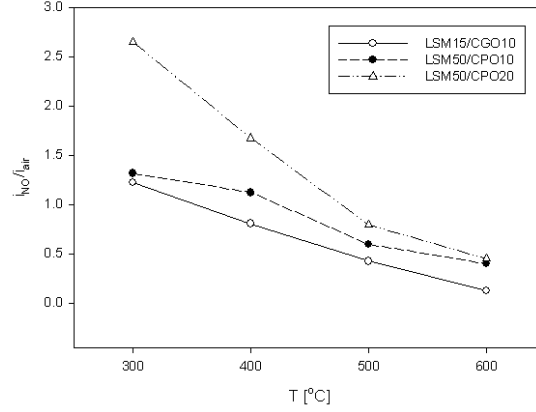


Figure 5.14: The ratio between  $i_{\text{NO}}$  and  $i_{\text{Air}}$  as a function of temperature for electrodes of LSM15/CGO10 ( $\square$ ), LSM50/CPO10 ( $\bullet$ ) and LSM50/CPO20 ( $\triangle$ ).

towards NO is not hindered by  $\text{O}_2$ . As there is only 5%  $\text{O}_2$  present compared to the 20% in air, then it is not expected that  $i_{\text{NO}+\text{O}_2}$  is larger than  $i_{\text{air}}$  unless the electrodes react with NO or an intermediate originating from NO. The ratio between  $i_{\text{NO}+\text{O}_2}$  and  $i_{\text{air}}$  can be seen in figure 5.15. The LSM50/CPO20 electrode has the

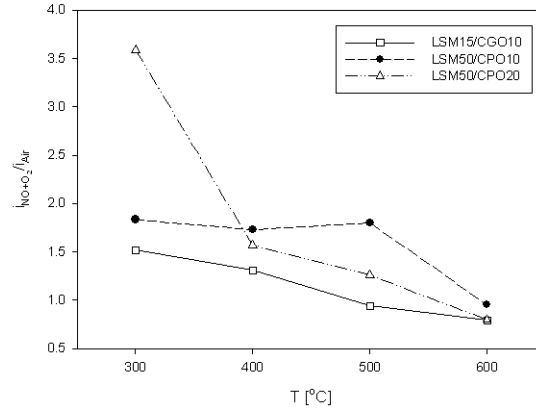


Figure 5.15: The ratio between  $i_{\text{NO}+\text{O}_2}$  and  $i_{\text{Air}}$  as a function of temperature for electrodes of LSM15/CGO10 ( $\square$ ), LSM50/CPO10 ( $\bullet$ ) and LSM50/CPO20 ( $\triangle$ ).

highest selectivity at 300 °C, and as the ratio between  $i_{\text{NO}+\text{O}_2}$  and  $i_{\text{air}}$  is well above 1, the apparent selectivity is not hindered by the presence of  $\text{O}_2$ . The electrodes containing CPO have similar selectivity in the temperature range of 400 to 600 °C, while the LSM15/CGO10 electrodes generally have lower selectivity except at 600 °C.

Electrodes containing CPO seems to have higher selectivity. This could be due to Pr ions changing oxidation state and thereby being more catalytically active or the the smaller amount of "third phase"  $\text{MnO}_x$  being present in LSM50 compared to LSM15.

The general trend with higher selectivity with lower temperature could be caused by change in the reaction mechanism at lower temperature. For the symmetrical cells the LF arc becomes less dominating with lower temperature, and cannot be found at 300 °C, this indicates that the direct reaction with NO takes place at low temperature. The discussion about selectivity is based on the assumption, that when the ratio between  $i_{\text{NO}+\text{O}_2}$  and  $i_{\text{Air}}$  is high, then the electrodes react preferably with NO compared to O<sub>2</sub>. There could, however, also be the alternative explanations; that the presence of NO makes the electrode more effective of reducing O<sub>2</sub>. Reinhardt *et al.* [22] suggested that a more reactive oxygen surface species was formed from reaction between O<sub>2</sub> and NO, but the investigations were based on measurements on currents and not gas analysis, therefore the reactive species could just as well have been NO<sub>2</sub> formed from O<sub>2</sub> and NO.

The measurements of  $i_{\text{NO}}$  from CV in figure 5.8 shows a slightly higher current density for LSM50/CPO20 than for LSM15/CGO10 electrodes, but the LSM15/CGO10 electrodes removed more NO than the LSM50/CPO20 electrodes. The cyclic voltammograms at 600 °C in 0.1% NO are, however, different from the others recorded at lower temperature, due to the cathodic peak. This cathodic peak is likely related to the reduction of NO or formation of nitrates.

The LSM50/CPO20 electrode has the highest CE, almost twice as high as for LSM15/CGO10 electrode. The concentration of O<sub>2</sub> decreases as well during polarisation, due to reduction of O<sub>2</sub>, but while the LSM15/CGO10 electrode has a 41% drop in O<sub>2</sub> concentration, then the LSM50/CPO20 electrode only experiences a drop of 22%. This explains the differences in CE. The LSM50/CPO20 electrode shows a high selectivity towards NO compared to O<sub>2</sub>, but only at low O<sub>2</sub> concentrations, not when 5% O<sub>2</sub> is present. The order of the electrodes with respect to CE corresponds to the order predicted by figure 5.14, the LSM50/CPO20 electrode which has the highest ratio between  $i_{\text{NO}}$  and  $i_{\text{air}}$  also has the highest CE.

If the current achieved at -0.8 V vs Pt/Air from the cyclic voltammogram for the LSM15/ CGO10 electrode is converted into ppm NO removed assuming the same CE as at 600 °C, then only 12 ppm NO is removed, approximately 1%. The CE is however, not necessary the same at lower temperatures. The selectivity seems to be better at 300 °C, so likely the CE would also be higher at this temperature, while the selectivity does not change remarkably from 600 to 500 °C.

## 5.5 Conclusion

The electrodes are not electrochemically active towards NO around open circuit voltage. A conversion arc in the impedance spectra in 0.1% NO is connected with low concentration of an intermediate - possible NO<sub>2</sub> - which react with the electrode instead. The NO<sub>2</sub> can be formed catalytically by the LSM in the electrode, either with small amounts of O<sub>2</sub> present in the atmosphere or from oxide ions from the electrode. The latter is supported by increasingly negative OCV with increasing flow rate, which cannot all be explained by the concentration of O<sub>2</sub>. Impedance measurements under polarisation show that the mechanism changes at more negative



potentials, from -0.6 V vs Pt/Air. It is likely that the electrodes react directly with NO at these low potentials.

All the electrodes tested could remove NO at 600 °C and below -0.6 V vs Pt/air in an atmosphere of 0.1% NO in Ar, and N<sub>2</sub> was produced. The (La<sub>0.85</sub>Sr<sub>0.15</sub>)<sub>0.9</sub>MnO<sub>3</sub>/Ce<sub>0.9</sub>Gd<sub>0.1</sub>O<sub>2</sub> electrode was the most active removing two thirds of all NO present when polarised with -0.8 V vs Pt/air.

Comparison of the current densities from cyclic voltammetry at -0.6 V vs Pt/Air in 0.1% NO in Ar and in Air shows that all the electrodes have increasing selectivity towards NO with decreasing temperature. Furthermore the results indicate that the (La<sub>0.5</sub>Sr<sub>0.5</sub>)<sub>0.99</sub>MnO<sub>3</sub>/Ce<sub>0.8</sub>Pr<sub>0.2</sub>O<sub>2</sub> electrode has the highest selectivity in the temperature range of 300 to 400 °C.

## Acknowledgements

This work was supported financially by The Programme Commission on Sustainable Energy and Environment, The Danish Council for Strategic Research, via the Strategic Electrochemistry Research Center (SERC) ([www.serc.dk](http://www.serc.dk)), contract no. 2104-06-0011.



# Chapter 6

## LSF and LSCF electrodes

### 6.1 Introduction

Electrodes based on LSF and LSCF shows high eletrocatalytic activity in intermediate temperature SOFCs (IT-SOFCs) , and are generally good oxygen electrodes. It was decided to characterise these materials mixed with CGO10 or CPO20 as composite electrodes in atmospheres containing NO. The characterisation was done with impedance spectroscopy on symmetrical cells. Further the LSCF40/CGO10 electrode was tested for gas conversion on a three electrode pellet.

### 6.2 Experimental

Metal oxide powders of  $\text{La}_{0.75}\text{Sr}_{0.25}\text{FeO}_3$  (LSF25),  $\text{La}_{0.6}\text{Sr}_{0.4}\text{FeO}_3$  (LSF40),  $\text{La}_{0.75}\text{Sr}_{0.25}\text{Co}_{0.2}\text{Fe}_{0.8}\text{O}_3$  (LSCF25),  $\text{La}_{0.6}\text{Sr}_{0.4}\text{Fe}_{0.8}\text{Co}_{0.2}\text{O}_3$  (LSCF40) and CPO20 was synthesized with the glycine nitrate combustion synthesis [80]. The powders were determined to be single phased by x-ray powder diffraction done on a Theta-Theta STOE diffractometer. Commercially available CGO10 from Rhodia was used. Inks for screen printing were produced from 50 wt. % CGO10 or CPO20 and 50 wt. % of LSF or LSCF, see table 6.1 for the composition of the 7 different types of electrodes.

Table 6.1: The composition of the screen printed electrodes.

Electrode	Composition
LSF25/CGO10	50 wt.% $\text{La}_{0.75}\text{Sr}_{0.25}\text{FeO}_3$ + 50 wt.% $\text{Ce}_{0.9}\text{Gd}_{0.1}\text{O}_2$
LSF25/CPO20	50 wt.% $\text{La}_{0.75}\text{Sr}_{0.25}\text{FeO}_3$ + 50 wt.% $\text{Ce}_{0.8}\text{Pr}_{0.2}\text{O}_2$
LSF40/CGO10	50 wt.% $\text{La}_{0.6}\text{Sr}_{0.4}\text{FeO}_3$ + 50 wt.% $\text{Ce}_{0.9}\text{Gd}_{0.1}\text{O}_2$
LSCF25/CGO10	50 wt.% $\text{La}_{0.75}\text{Sr}_{0.25}\text{Co}_{0.2}\text{Fe}_{0.8}\text{O}_3$ + 50 wt.% $\text{Ce}_{0.9}\text{Gd}_{0.1}\text{O}_2$
LSCF25/CPO20	50 wt.% $\text{La}_{0.75}\text{Sr}_{0.25}\text{Co}_{0.2}\text{Fe}_{0.8}\text{O}_3$ + 50 wt.% $\text{Ce}_{0.8}\text{Pr}_{0.2}\text{O}_2$
LSCF40/CGO10	50 wt.% $\text{La}_{0.6}\text{Sr}_{0.4}\text{Co}_{0.2}\text{Fe}_{0.8}\text{O}_3$ + 50 wt.% $\text{Ce}_{0.9}\text{Gd}_{0.1}\text{O}_2$
LSCF40/CPO20	50 wt.% $\text{La}_{0.6}\text{Sr}_{0.4}\text{Co}_{0.2}\text{Fe}_{0.8}\text{O}_3$ + 50 wt.% $\text{Ce}_{0.8}\text{Pr}_{0.2}\text{O}_2$

The electrodes were screen printed on each side of pieces of CGO10 tape, producing symmetrical cells with the dimension 5 cm x 5 cm. The large cells were

sintered at 1250 °C and cut into small symmetrical cells (6 mm x 6 mm) with a diamond tool. The micro structure of the symmetrical cells were examined with a Hitachi TM 1000 scanning electron microscope.

Gold paste with 20 wt. % carbon was painted on both side of the cells as a current collector, and the 4 similar cells was mounted in the symmetrical cell setup, as described in chapter 4 .

The atmosphere in the setup was controlled and changed between air and 1 % NO in Ar and the gas flow was 10 and 100 mL/min, 100 mL/min was used unless otherwise stated. The temperature range was 300 to 600 °C.

The symmetrical cells were subjected to EIS, the frequency range was 1 mHz to 80 kHz, but frequencies above 10 kHz was disregarded in the fitting process. A Hioki 3522 was used for the EIS measurements.

Further a LSCF40/CGO10 electrode was screen printed on a CGO three electrode pellet. Gold paste with 20 wt. % carbon was used as current collector together with a piece of gold net. A counter electrode was painted onto the CGO pellet with Pt paste, and Ag sealing was used between the alumina tubes and CGO pellet. The atmosphere at the reference electrode was air, and the atmosphere at the working electrode was changed between air, 0.1 % NO in Ar and 0.1 % NO + 5% O<sub>2</sub> in Ar. Electrochemical measurements was done in the temperature range of 400 to 600 °C. A Gamry Femtostat was used for CV, EIS and chronoamperometry. The frequency range used for EIS was 1 mHz to 300 kHz. The CV measurements were performed with 1 and -1 V vs Pt/air as the limits and a scan rate of 5 mV/s. The electrode was subjected to chronoamperometry for 2 hours, and the composition of the atmosphere was measured before, during and after the polarisation with a quadrupole mass spectrometer, OmniStar from Pfeiffer.

The impedance data were analysed with the software "Equivalent circuit for Windows" from University of Twente [92].

## 6.3 Results

### 6.3.1 Symmetrical cells

#### SEM-pictures

The SEM investigation of the electrodes of the symmetrical cells showed some pores in the electrodes. The LSF/LSCF particles were larger than the CGO10/CPO20, and the smaller CGO10/CPO20 particles was packing around the LSF/LSCF particles, see figure 6.1. The electrodes had a thickness of around 10 to 20  $\mu\text{m}$ .

#### EIS measurements

Equivalent circuits were fitted to the impedance data, and between 2 and 4 arcs were necessary for a satisfying fit depending on temperature and atmosphere.

The  $R_p$  for the cells in air is much smaller than for 1 % NO in Ar, see figure 6.2 in the temperature range of 500 to 600 °C, while at 300 °C the  $R_p$  is smaller for cells in 1 % NO in Ar than in air.

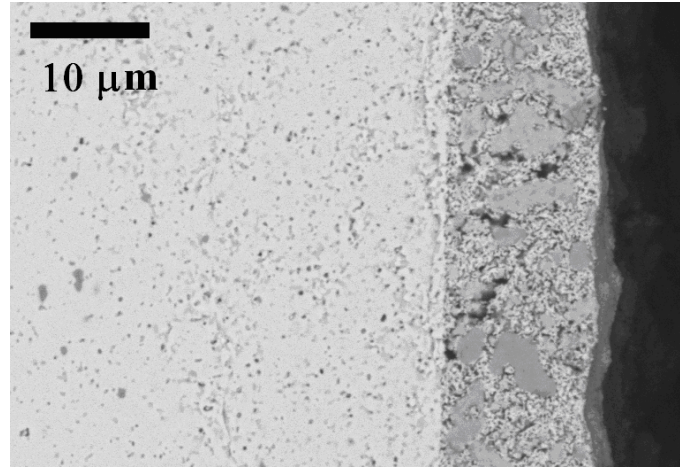


Figure 6.1: SEM picture of LSF40/CGO10 composite electrode on symmetrical cell.

5 different arcs can be identified for the impedance spectra recorded in air, but they

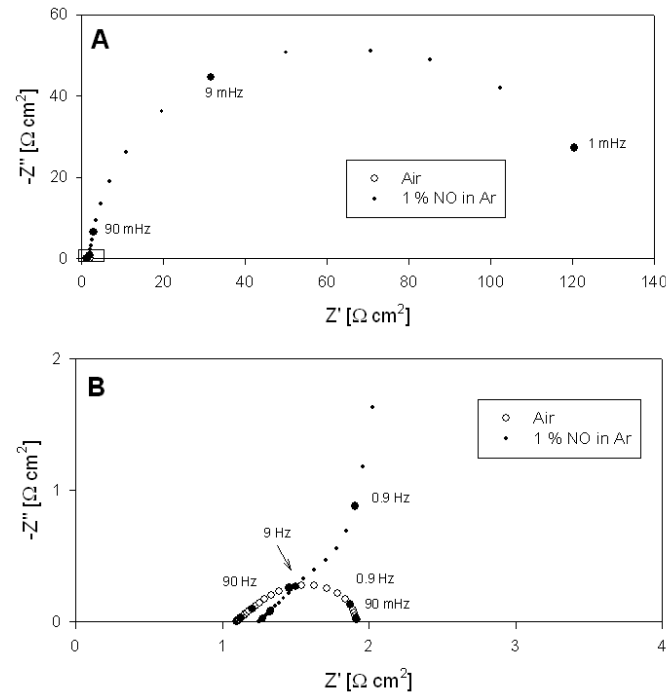


Figure 6.2: A: Impedance spectra of LSF25/CGO10 electrode in air and 1 % NO in Ar at 600 °C. B: The high frequency region, where the impedance spectra in air is clearer.

are not all present at the same time in any impedance spectra. A large arc in the low frequency area can be found in impedance spectra recorded in the temperature range 500 to 600 °C, it has an EC around 0.11 to 0.18  $\text{F cm}^{-2}$  and an  $\alpha$  value of 0.97. A middle frequency (MF) arc can be found at all temperatures, and it becomes dominating at low temperatures. The MF arc has an  $\alpha$  value around 0.8

and the activation energy,  $E_a$ , is in the range 1 to 1.6 eV, see table 6.2. The EC values at 600 °C is typically around  $10^{-1}$  F cm $^{-2}$ . Two more arcs are found in the high frequency area with  $\alpha$  values of 0.6 to 0.7 and 0.5, they are not present in all impedance spectra, depending on temperature and electrode material. These two arcs are also seen in the impedance spectra recorded for cells in 1 % NO in Ar. Furthermore a high frequency impedance arc with an  $\alpha$  values of 0.7 to 0.8 is found in impedance spectra in the temperature range of 300 to 400 °C. This arc is present in all impedance spectra recorded in this temperature range independent of electrode material and atmosphere, and the EC is in the range  $10^{-6}$  to  $10^{-5}$  F cm $^{-2}$ .

An MF arc is also found in the impedance spectra recorded in 1 % NO in Ar, similar to the one recorded in air, with an  $\alpha$  value of 0.8, but with far lower activation energy, 0.3 to 0.9 eV see table 6.2. The impedance spectra recorded in 1 % NO in Ar are dominated by a very large low frequency (LF) arc, this causes the large difference in  $R_p$  depending on atmosphere. The summit frequency of the LF arc is typically around 5 - 10 mHz and it is close to a perfect half circle with  $\alpha$  values around 0.98-1. The activation energy ( $E_a$ ) of the LF arc is very low, typically between 0.2 to 0.4 eV, see table 6.2. The LF arc are most dominant at high temperatures, but can also be found at temperatures as low as 300 °C, see figure 6.3. The size of the LF

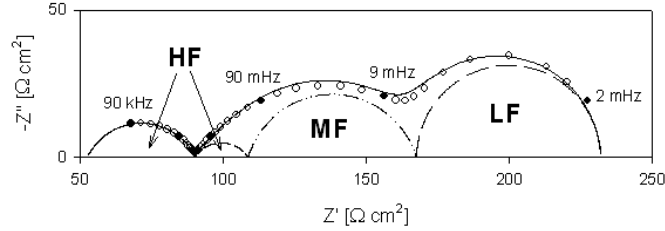


Figure 6.3: Impedance spectra of LSCF40/CPO20 cell in 1 % NO in Ar at 300 °C with a flow of 10 mL/min.

arc is also strongly dependent on the flow of gas, with the resistance of the LF arc increasing with increasing gas flow, see figure 6.4 for an example.

The  $R_p$  for the different types of electrodes in air in the temperature range of 300 to 600 °C can be seen in figure 6.5. The data shows that composite electrodes of LSF25/CPO20 have higher  $R_p$  than the LSF25/CGO10 and LSF40/CGO10. Doping of LSF with 20 % Co also lowers  $R_p$  for the electrodes containing CPO.

Figure 6.6 similarly shows the  $R_p$  for all the electrodes in 1 % NO in the temperature range of 300 to 600 °C. The LSF25/CPO20 electrodes have lower  $R_p$  in the temperature range of 300 to 500 °C, than the LSF25/CGO10 and LSF40/CGO10 electrodes.

Table 6.2:  $E_a$  values for impedance arcs for symmetrical cells in air and 1 % NO in Ar with a gas flow of 100 mL/min.

Electrode	Air MF arc	1 % NO in Ar MF arc	LF arc
LSF25/CGO10	1.18(1) eV	0.69(6) eV	0.29(1) eV
LSF40/CGO10	1.47(3) eV	0.70(7) eV	0.26(7) eV
LSF25/CPO20	1.27(4) eV	0.53(8) eV	0.18(2) eV
LSCF25/CGO10	0.93(4) eV	0.7(1) eV	0.33(3) eV
LSCF40/CGO10	1.17(2) eV	0.53(7) eV	0.34(3) eV
LSCF25/CPO20	1.11(4) eV	0.45(2) eV	0.3(1) eV
LSCF40/CPO20	1.26(2) eV	0.69(3) eV	0.25(5) eV

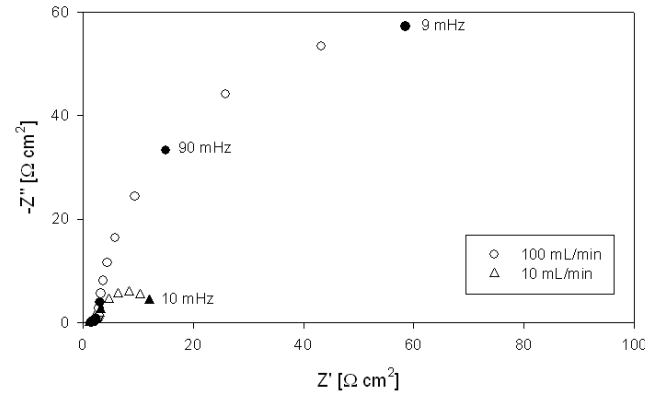


Figure 6.4: Impedance spectra of LSCF40/CGO10 cell in 1 % NO in Ar at 600 °C with a flow of 100 mL/min (○) and 10 mL/min (△).

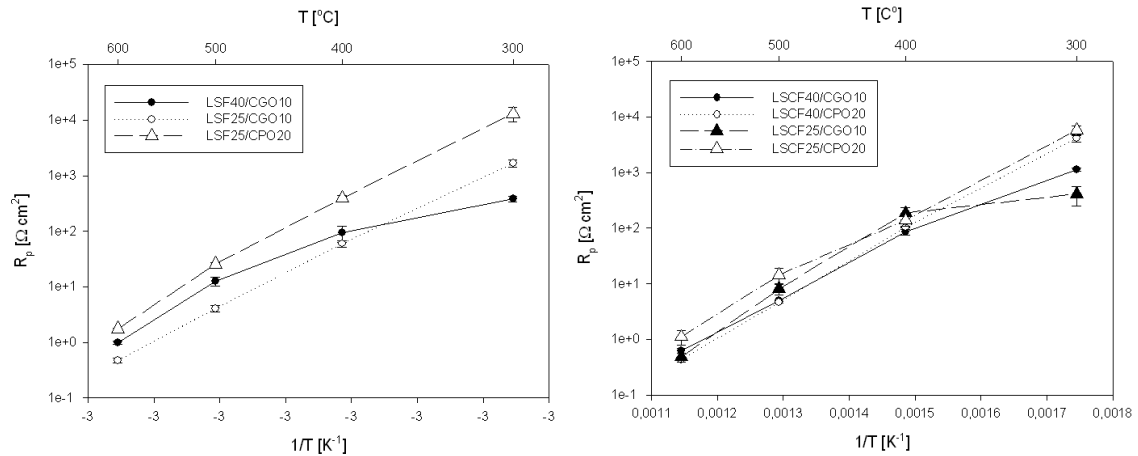


Figure 6.5: Arrhenius plots of  $R_p$ -values determined from impedance spectra for electrodes in air with a flow of 100 mL/min

### 6.3.2 Three electrode cell

All the potentials reported in this section have been subtracted IR losses due to the geometry of the 3E pellet, where a thick layer of CGO10 separates the reference

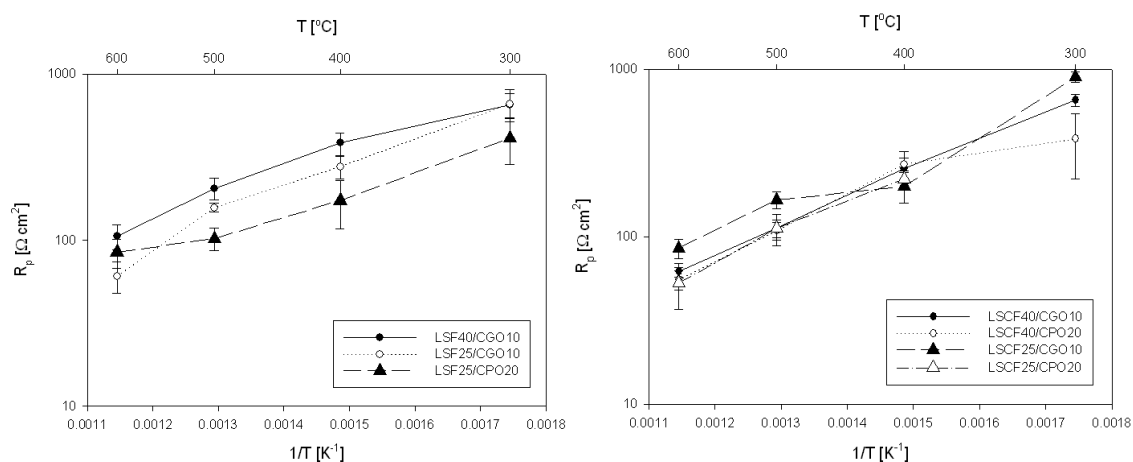


Figure 6.6: Arrhenius plots of  $R_p$ -values determined from impedance spectra for electrodes in 1 % NO in Ar with a flow of 100 mL/min

electrode from the working electrode. The ohmic resistance due to the CGO10 layer is found from the impedance spectra.

The CV measurements all showed that higher current densities could be obtained in an atmosphere of air than an atmosphere containing NO. The current densities from air and 0.1 % NO + 5 %  $O_2$  in Ar were very close at 400 °C, see figure 6.7.

The LSCF40/CGO10 electrode of a three electrode cell was polarised with -0.7

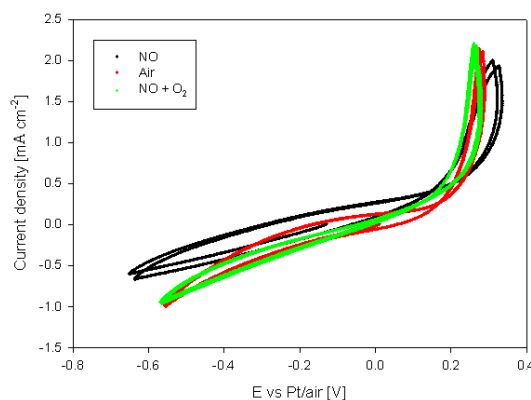


Figure 6.7: Cyclic voltammogram for LSCF40/CGO10 electrodes cells in 0.1% NO in Ar, 0.1% NO + 5 %  $O_2$  in Ar and air at 600 °C.

V vs Pt/air and -0.9 V vs Pt/air at 600 °C in 0.1 % NO in Ar. It was possible to remove up to 88 % of the NO present when the electrode was polarised with -0.9 V vs Pt/air. The increase in  $N_2$  and decrease in  $O_2$  along with the current efficiency (CE) can be seen in table 6.3. The CE depends strongly on the polarisation.



Table 6.3: Degree of NO conversion and CE for polarisation with -0.7 and -0.9 V vs Pt/Air for LSCF40/CGO10 electrodes in 1000 ppm NO in Ar, 5 mL/min flow and at 600 °C.

Polarisation	-0.7 V	-0.9 V
NO conversion	23%	88%
NO removed	200 ppm	760 ppm
O <sub>2</sub> removed	44%	36%
N <sub>2</sub> formed	120 ppm	480 ppm
CE	7%	20%
Current density	1.8 mA cm <sup>-2</sup>	2.5 mA cm <sup>-2</sup>

## 6.4 Discussion

### 6.4.1 Electrode composition

The array of composite electrodes tested has variation of three parameters:

**CGO10/CPO20** The composite electrodes all contain 50 wt. % doped ceria, it is either CGO10 or CPO20.

**Sr content** The A site ion of the perovskite is La substituted with either 25 or 40 % Sr.

**Co content** The B site ion of the perovskite is Fe, for some electrodes 20 % of Fe is replaced by Co.

The LSCF40/CPO20 electrodes have the lowest  $R_p$  at 600 °C in air, 0.44(1)  $\Omega$  cm<sup>2</sup>, while at 300 °C the LSF40/CGO10 electrodes have the lowest  $R_p$ . When the atmosphere is 1 % NO in Ar, then the LSCF25/CPO20 electrodes have the lowest  $R_p$  at 600 °C, 50 (10) $\Omega$  cm<sup>2</sup>, while the LSCF40/CPO20 electrodes have the lowest  $R_p$  at 300 °C.

### CGO10/CPO20

CGO10 is often used in composite electrodes, as the material has good ionic conduction, and addition of CGO should therefore expand the TPB. It was shown in chapter 4 that composite electrodes of CPO20 had lower  $R_p$  and higher selectivity than the ones containing CGO10 and CPO10. Furthermore the XANES measurements clearly shows that the Pr ions in CPO20 reacts with NO to a greater extent than in CPO10, see chapter 3.

For electrodes containing LSF in air, the replacement of CGO with CPO20 seems to increase the  $R_p$ . On the other hand, when the atmosphere is 1 % NO in Ar, the  $R_p$  is lowered for CPO20 containing electrodes in the temperature range of 300 to 500 °C in 1 % NO in Ar.

The electrodes with CPO20 had higher  $E_a$  for the MF arc than the ones with CGO10 in air for all cells, see table 6.2. Likewise the  $E_a$  for the MF and LF arc in 1 % NO

was lowered for the most CPO20 containing electrodes. This indicates that addition of CPO20 to composite electrodes with LSF and LSCF increases the selectivity towards NO compared to O<sub>2</sub>.

### Sr content

For the LSCF electrodes in air, the ones with 40 % Sr have clearly higher  $E_a$  than the electrodes with only 25 % replacement of La with Sr on the A site.

### Co content

Substituting 20 % of the B site Fe with Co decreases the  $E_a$  (air, MF) for all electrodes. When the atmosphere is 1 % NO, the substitution of 20 % Fe with Co increases the  $E_a$  (LF) value in all cases, while the  $E_a$  (MF) decreases.

## 6.4.2 Selectivity

A rough measure of selectivity can be calculated as the ratio between  $R_p$  in 1 % NO in Ar and  $R_p$  in air. The ratio between  $R_p(\text{NO})$  and  $R_p(\text{air})$  should preferably be lower than 1. The ratio is higher than 1 in the temperature range 500 to 600 °C for all electrodes, at 400 °C some of the electrodes have ratios below 1 and at 300 °C the most electrodes have ratios below 1. Generally the selectivity increases with decreasing temperature. The ratio between  $R_p(\text{NO})$  and  $R_p(\text{air})$  are shown in figure 6.8. It is clear that the LSF25/CPO20 electrodes have the lowest ratio overall, especially in the temperature range 300 to 400 °C. The LSF25/CPO20 electrodes have the lowest  $E_a$  value for the LF arc of all the electrodes tested, and the resistance of the LF arc makes up a large part of the  $R_p$ . Therefore the  $R_p(\text{NO})$  value for LSF25/CPO20 electrodes will be low. The  $E_a$  (air, MF) value for LSF25/CPO20 electrodes are 1.4(1) eV, which is the second highest.

The LSCF40/CPO20 electrodes have the second best selectivity, although the ratio of  $R_p(\text{NO})$  and  $R_p(\text{air})$  is only below 1 at 300 °C. The working electrode of the three electrode pellet, LSCF40/CGO10, does not have particularly good selectivity, but at least the ratio of  $R_p(\text{NO})$  and  $R_p(\text{air})$  are only below 1 at 300 °C. Gas conversion was only observed at 600 °C, but this is due to the poor contact between the small electrode area and the NO molecules in the gas stream. N<sub>2</sub> was formed as the product as expected. The CE increases with polarisation, and the percentage of O<sub>2</sub> removed actually decreases with higher polarisation, indicating higher selectivity with a high polarisation. This was not seen for the electrodes with LSM.

The ratio between  $i_{\text{NO}}$  and  $i_{\text{air}}$  in the cathodic region (-0.4 V vs Pt/air) for the LSCF40/CGO10 electrodes can be obtained from the CV measurements, and it is 0.17 at 600 °C, but increases to 0.67 at 400 °C. So the selectivity becomes better, but the electrode still has a higher current density in air than in NO at 400 °C. It should however be noticed that there are 20 % O<sub>2</sub> in air, which could be reduced, while there is only 0.1 % NO present (and around 0.2 % O<sub>2</sub>). Further the  $i_{\text{NO}+\text{O}_2}$  is higher than  $i_{\text{air}}$  for the electrode at 400 °C. As mentioned for the electrodes with LSM, then the increase in current density, when NO is present together with 5 %

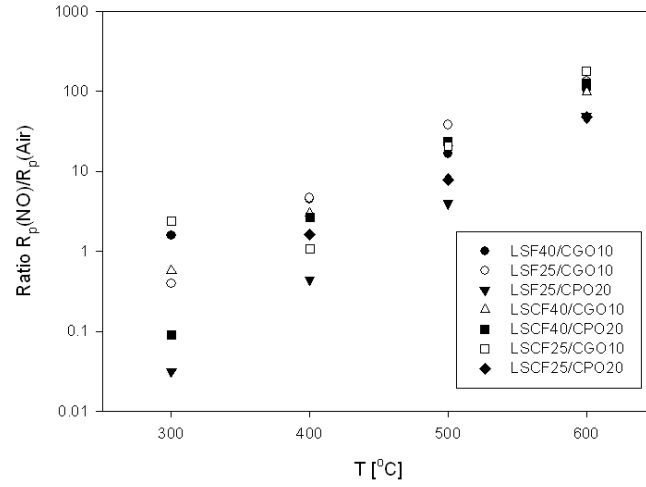


Figure 6.8: The ratio between  $R_p(\text{NO})$  and  $R_p(\text{air})$  as a function of temperature for all the composite electrodes.

$\text{O}_2$  could be caused by the NO forming reactive surface species with  $\text{O}_2$  as suggested by Reinhardt *et al.* [22].

### 6.4.3 Comparison with previous results

The electrodes with LSF and LSCF have much lower  $R_p$  values in air, than the ones with LSM. The  $R_p$  values for the LSM50/CPO20 electrodes in air can be seen in figure 6.9 together with the corresponding  $R_p$  values for the LSF and LSCF cells. The LSM50/CPO20 cells had the lowest  $R_p$  in air among the cells with LSM, but at 600 °C the  $R_p$  value was still more than 6 times larger than  $R_p$  for the LSCF40/CPO20 cells. It is clear that the LSF and LSCF containing electrodes are much better in air, first at 300 °C does the  $R_p$  of the LSM50/CPO20 electrode come within range of the LSF and LSCF electrodes with the largest  $R_p$  values.

So these electrodes are good at reducing  $\text{O}_2$ , but the scope in this project is to locate electrodes which are selective towards NO. The fact that the electrodes are very active in air does not necessarily mean that they are not selective, if only they show an even higher activity in an atmosphere containing NO. The LSCF40/CPO20 electrode is an active air electrode with the lowest  $R_p$  in air at 600 °C, but it still has the second lowest ratio of  $R_p(\text{NO})/R_p(\text{air})$ .

The LSCF40/CGO10 electrode can remove a higher percentage of NO when polarised, than what is seen for the LSM electrodes. But it is also polarised with -0.9 V vs Pt/Air, where the others only were polarised with -0.8 V vs Pt/air, and it is clear that the amount of NO removed depends strongly on the polarisation.

The LF arc in NO containing atmosphere in impedance spectra at OCV is even more dominating in the spectra for the electrodes with LSF and LSCF than for the electrodes with LSM. The change in flow also has more effect, and the LF arc can even be identified down to 300 °C. For the electrodes with LSM the LF arc could only be identified in the temperature range of 400 to 600 °C. The LF arc is assumed

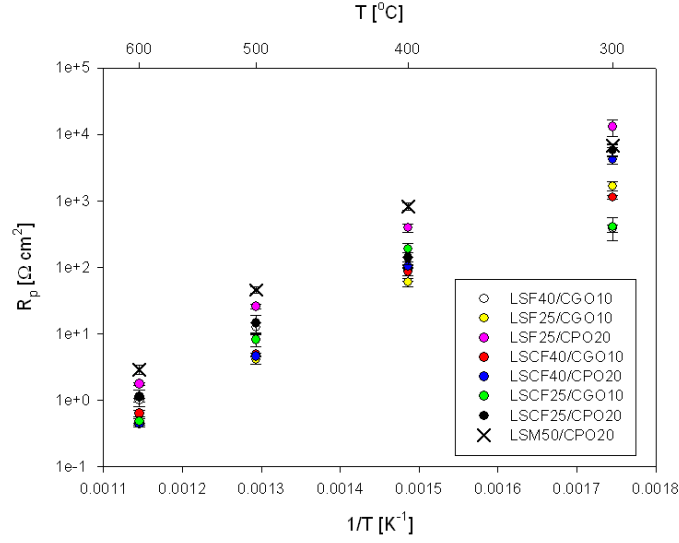


Figure 6.9:  $R_p(\text{air})$  as a function of temperature for all the composite electrodes and LSM50/CPO20 electrodes.

to be caused by the low concentration of an intermediate,  $\text{NO}_2$ , through which the electrodes react. If the LF arcs are even more flow dependent and dominant in the impedance spectra of the electrodes with LSF and LSCF, the concentration of the intermediate must be even lower, thereby causing the conversion arc. The flow rate of the gas is the same in the examples (10 and 100 mL/min), so the difference in  $\text{NO}_2$  (presumably) concentration must be caused by lower formation of  $\text{NO}_2$ . The cobaltite and ferrite perovskites are simply not as effective catalysts in the reaction of oxidising NO to  $\text{NO}_2$  as LSM. When the LF arc is not seen at 300 °C for the electrodes with LSM, then it was assumed that either the larger  $E_a$  for the MF arc meant that the MF arc grew to large for the LF arc to be visible. Alternatively the kinetics changed with lower temperature, and the electrodes would react relatively more with NO. Near OCV the electrodes with LSF and LSCF are still electrochemically unreactive towards NO, even at 300 °C.

# Chapter 7

## Porous cell stacks

This chapter is based on the manuscript "Electrochemical removal of  $\text{NO}_x$  with porous cell stacks".

### Abstract

In this study porous cell stacks were investigated for their ability to remove  $\text{NO}_x$  electrochemically. The cell stacks were made from laminated tapes of porous electrolyte ( $\text{Ce}_{0.9}\text{Gd}_{0.1}\text{O}_{1.95}$  (CGO10)) and composite electrodes of  $\text{La}_{1-x}\text{Sr}_x\text{MnO}_3$  ( $x = 0.15, 0.5$ ) and ceria doped with Gd or Pr. The cell stacks were infiltrated with nano-particles of ceria, CGO10 and  $\text{Ce}_{0.8}\text{Pr}_{0.2}\text{O}_{2-\delta}$  (CPO20) after sintering. A gas stream containing NO were sent through the cell stack. When the cell stacks were polarised with 4.5 V (= 0.75 V per cell) then it was possible to remove som of the  $\text{NO}_x$  in the temperature interval of 250 to 400 °C.

The cell stacks infiltrated with ceria showed the highest activity, while the ones infiltrated with CGO10 had the highest selectivity towards NO compared to  $\text{O}_2$ . Multiple impregnations increased the activity of the cell stacks for NO removal. When the cell stack was polarised with 9 V (= 1.5 V for each cell) it was possible to remove up to 35 % of NO present. The NO removed at 400 °C was decomposed into  $\text{N}_2$  and  $\text{O}_2$ .

### 7.1 Introduction

$\text{NO}_x$  are formed from  $\text{N}_2$  and  $\text{O}_2$  in the high temperatures of combustion engines as a side product. The  $\text{NO}_x$  are poisonous to human beings and dangerous to the environment. Therefore they should be removed from the exhaust gas.

One way, among others, to clean the exhaust gas for  $\text{NO}_x$  is by electrochemical removal of  $\text{NO}_x$ . The principle is to apply a voltage over an electrochemical cell, then NO is reduced at the cathode forming  $\text{N}_2$ , oxide ions are transported through the electrolyte, and  $\text{O}_2$  formed at the anode.

It was first demonstrated in 1975 by Pancharatnam *et al.* [19] that NO can be electrochemically decomposed over a YSZ electrolyte with Pt electrodes. Afterwards many other studies have been done concerning electrochemical removal of

$\text{NO}_x$  [23, 28, 18].

The nitrogen oxide molecules react with the surface of the electrode, and therefore high surface area of the electrodes and good contact between the gas and electrode are necessary for high activity. Consequently porous cell stack, where the gas flows through the cell, as described in [85] is used in this study. This way contact between the nitrogen oxide molecules and the electrode is maximised, and gas conversion could be detected at temperatures as low as 250 °C.

The electrodes are composite electrodes of lanthanum strontium manganites (LSM) and ceria doped with praseodymium or gadolinium.

LSM has earlier been shown to catalyse the reduction of NO [27], and it is a well known material for cathodes in solid oxide fuel cells. Ceria doped with praseodymium has been used for a wide number of applications, such as SOFC electrodes [68], gas sensors [69] and soot oxidation [70].  $\text{Ce}_{1-x}\text{Pr}_x\text{O}_{2-\delta}$  (CPO) is both an electronic and ionic conductor, and the Pr ions can easily change oxidation state between +3 and +4, so it might have some catalytic activity as well.

In previous studies [98, 99] composite electrodes of LSM and doped ceria (Pr, Gd) it was found that the selectivity of the electrodes increased with decreasing temperature. The electrodes with  $(\text{La}_{0.5}\text{Sr}_{0.5})_{0.99}\text{MnO}_3$  and CPO20 had the highest selectivity. NO could be removed at 600 °C and  $\text{N}_2$  formed. It was not however possible to observe removal of NO at lower temperatures due to little electrode area and poor contact between electrode and gas. Further the electrodes were not directly active towards NO around open circuit voltage (OCV), instead they reacted with a catalytically formed intermediate, likely  $\text{NO}_2$ . The electrodes started to react directly with NO at voltages above -0.6 V vs Pt/air.

## 7.2 Experimental

Porous cell stacks were made by lamination of electrode and electrolyte tapes. First a tape was cast from a slurry. The slurries were made by ball milling the powders together with solvent, binder and graphite as a pore former. Then the dried tapes are laminated, cut into round cells and sintered.

Metal oxide powders with the composition  $\text{Ce}_{0.9}\text{Pr}_{0.1}\text{O}_{2-\delta}$  (CPO10), CPO20 and  $(\text{La}_{0.5}\text{Sr}_{0.5})_{0.99}\text{MnO}_3$  (LSM50) were synthesised with the glycine combustion synthesis [80]. The nitrate solutions or the combustion synthesis were made from Mn, La, Pr and Sr nitrates from Alfa Aesar and Ce nitrate from Johnson Matthey. After the combustion synthesis the powders were calcined, six hours at 1000 °C for the CPO10 and CPO20 and 50 hours at 1200 °C for LSM50. X-ray powder diffraction on a Theta-Theta STOE diffractometer confirmed the powders to be single phased. Powders of  $(\text{La}_{0.85}\text{Sr}_{0.15})_{0.9}\text{MnO}_3$  (LSM15) was obtained from Haldor Topsoe A/S and CGO10 was commercially available from Rhodia.

The LSM were understoichiometric on the A site. Therefore a third phase of  $\text{MnO}_x$  is also present, mostly in the LSM15. Furthermore LSM50 and CPO20 were purchased from CerPoTech A/S in larger quantities to produce a large batch of electrodes with LSM50/CPO20.

Four electrode slurries were prepared, with the compositions shown in table 7.1.

The electrolyte slurries were made from CGO10.

During tape casting the gap between the blades were  $250\ \mu\text{m}$  for electrode tapes

Table 7.1: List of the investigated types of porous cell stacks composition and BET surface.

Name	Composition of electrode	BET surface
PSC1	50 wt. % LSM15 + 50 wt. % CGO10	$0.77\ \text{m}^2/\text{g}$
PSC2	50 wt. % LSM50 + 50 wt. % CPO10	$0.40\ \text{m}^2/\text{g}$
PSC3	50 wt. % LSM50 + 50 wt. % CPO20	$0.80\ \text{m}^2/\text{g}$
PSC3b	65 wt. % LSM50 <sup>a</sup> + 35 wt. % CPO20 <sup>a</sup>	$1.49\ \text{m}^2/\text{g}$

<sup>a</sup> Powders purchased from CerPoTech A/S

and  $200\ \mu\text{m}$  for electrolyte. After drying the tapes were laminated with a MailTech laminating machine. Alternating layers of electrode and electrolyte tapes were laminated into a cell stacks with 13 layers, corresponding to 6 cells. This way the cells are symmetrical, with anodes and cathodes being identical, and the anode of cell no. 1 is at the same time the cathode of cell no. 2. Figure 7.1 shows a sketch of a porous cell stack. A more detailed description of production of such cell stacks can be found in [85].

After lamination the green cell stacks were cut into round cells and sintered at

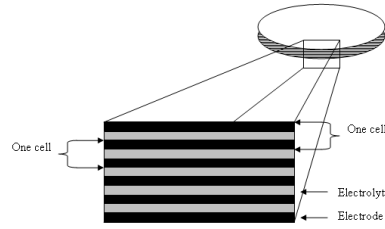


Figure 7.1: Sketch of a porous cell stack.

$1250\ ^\circ\text{C}$ .

A list of types of porous cell stacks and their code is found in table 7.1.

The micro structure of the porous cell stacks were examined in a Hitachi TM 1000 scanning electron microscope (SEM), and BET measurements were performed on broken pieces of the porous cell stacks with an Autosorb 1 from Quantachrome Instruments.

Current collector of gold paste with 20 wt. % carbon (pore former) were painted on each side of the porous cell stack and then sintered at  $850\ ^\circ\text{C}$ . Following that some of the cell stacks were infiltrated with nitrate solutions, 3 M in millipore water with a surfactant added, see Sogaard *et al.* [100] for further details on infiltration with ceria and SEM images of infiltrated electrodes. The cell stacks which were infiltrated multiple times were heated to  $350\ ^\circ\text{C}$  in a furnace in between the infiltrations. The cell stacks gained  $8\ \text{mg}/\text{cm}^2$  on average after each infiltration. Finally the cell stacks were ground on the sides in order to avoid short circuits from gold paste and LSM. The round cell stacks are approximately 14 mm in diameter and have a thickness

around 400  $\mu\text{m}$  depending on the electrode thickness.

For the electrochemical testing the cell stacks were placed between two alumina tubes inside a glass tube in a one atmosphere setup, as illustrated in figure 7.2. The gas flows through the porous structure of the cell, thereby achieving good contact between the gas molecules and the electrodes. This also means that the gas at the anode and cathode sides of the cells are not separated, so there will be a growing content of  $\text{O}_2$  as the gas passes through the cell if NO decomposition takes place, and also the anodes can get into contact with NO. A disadvantage with this setup is that it is possible for some of the gas to go out through the sides of the porous cell stack, which are not sealed, into the small void in the glass tube, and maybe back into the porous cell stack, thereby avoided to pass through all the layers of the cell stack. This does not give any leak, as the gas tube is sealed, but the amount of NO removed could be larger than reported, due to some gas voiding the cell stack. Furthermore due to small leaks in the tubings for the setup some  $\text{N}_2$  and  $\text{O}_2$  were present in the system: around 250 ppm  $\text{O}_2$  and 1200 ppm  $\text{N}_2$ .

The gas flow is provided by Brooks mass flow controllers 0-100 mL/min, and the

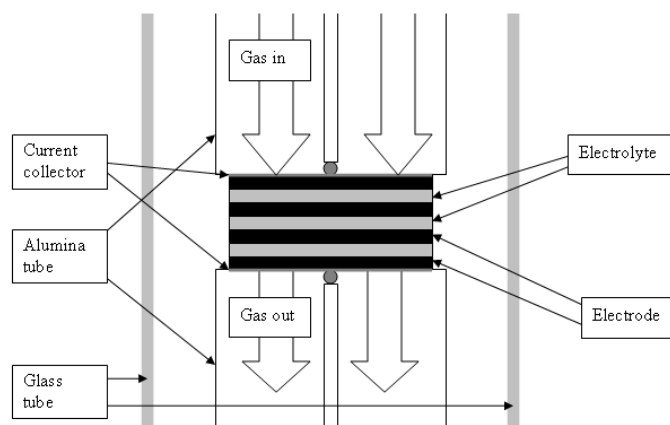


Figure 7.2: Sketch of the setup for porous cell stacks.

gas flow was 33 mL/min unless otherwise stated. The composition of the atmosphere was 0.1 % NO in Ar or 0.1 % NO + 5 %  $\text{O}_2$  in Ar. The setup was placed in a small vertical furnace, which allowed the temperature to be controlled. The measurements were done at 250, 300, 350 and 400  $^{\circ}\text{C}$ .

A Gamry Reference600 potentiostat was used for electrochemical measurements. The cell stack was subjected to cyclic voltammetry (CV) and chronoamperametry. Typically the cell stacks was polarised with 4.5 V for 3 hours.

The outlet gas composition was monitored with a quadrupole mass spectrometer (MS) from Pfeiffer, the Omnistar GSD 301. When the gas composition is changed, it takes approximately 2 minutes before that change is detected in the MS, due to the time it takes for the gas to flow through the pipes from the setup to the MS.



## 7.3 Results

### 7.3.1 Characterisation of porous cell stacks

The BET measurements on pieces of porous cell stacks are shown in table 7.1. The PSC3b cell stacks has remarkably higher surface area than the other types of cell stacks.

The SEM pictures of the profile of the sintered cell stacks showed a porous struc-

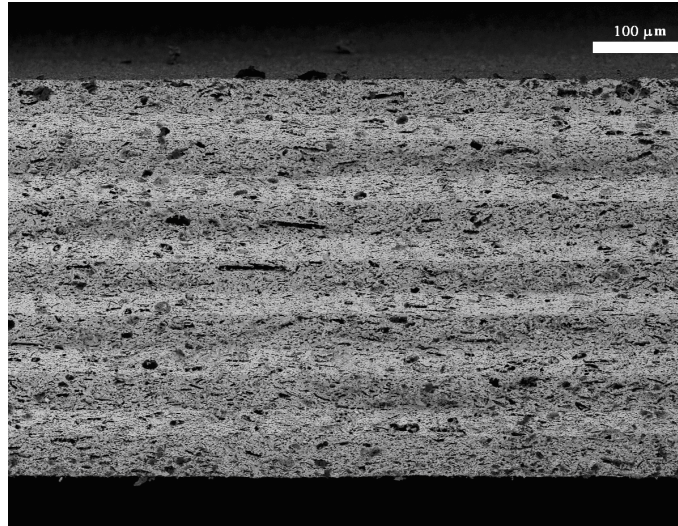


Figure 7.3: SEM picture of the PCS1 cell stack with 13 layers and LSM15/CGO10 electrodes.

ture both for electrodes and electrolytes. The average thickness of the electrolyte layers was 15-20  $\mu\text{m}$ , while the electrode layers had a thickness of 25-30  $\mu\text{m}$  for the LSM50/CPO20 and LSM15/CGO10 electrodes, the LSM50/CPO10 was slightly thicker, 35-40  $\mu\text{m}$  on average. The structure consists of many small pores, along with larger pores, making a network of channels where the infiltration liquid can enter. Further the gas molecules can travel through the cell by the larger pores, so the pressure drop over the cell does not cause the structure to fracture. And the smaller voids provide a high surface area with good contact between the gas molecules and active sites of the electrode. A SEM micrograph of the PCS1 cell can be seen in figure 7.3

### 7.3.2 Electrochemical results

Cell stacks, which had not been infiltrated, were polarised with 4.5 V (= 0.75 V per cell) in 0.1 % NO in Ar for two hours. A small drop in the NO concentration, around 25 ppm, could be seen in the first few minutes after start of polarisation. The NO concentration returned to normal level after 20 minutes.

Cyclic voltammograms of a PCS3b cell stack with and without ceria infiltration is shown in figure 7.4, the infiltrated cell stack have a current density which is around 15 times larger at 4.5 V than for the cell stack without infiltration. When subjected

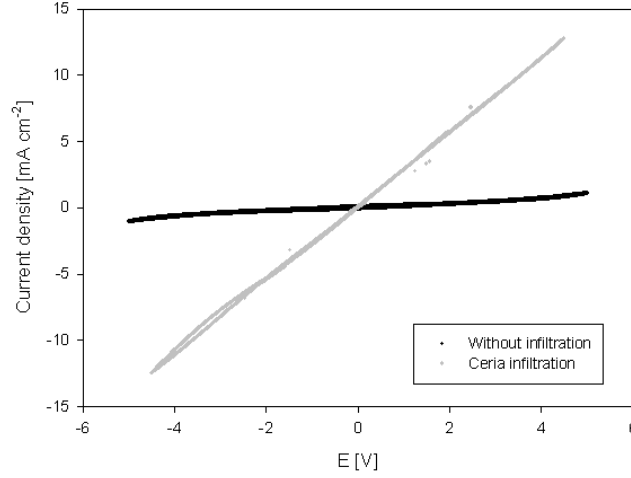


Figure 7.4: Cyclic voltammogram of a 13 layer PCS3b cell stack with and without infiltration in 0.1 % NO in Ar at 400 °C.

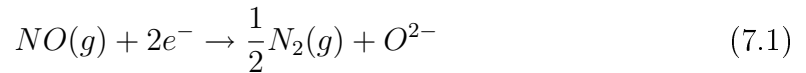
to a polarisation of 4.5 V (= 0.75 V per cell) gas conversion was visible with the MS for cell stacks with all types of infiltration.

The infiltrated cell stacks lost some activity with time at each polarisation. For instance when comparing the values for NO removal in table 7.4 and in figure 7.6 for PCS3b infiltrated with ceria and polarised with 4.5 V at 400 °C, then 10 % NO removed is reported in table 7.4, while around 5 % NO is removed according to figure 7.6. The difference is caused by the experiment behind the results in table 7.4 being conducted earlier in the cell stacks lifetime than the experiment, from which the data in figure 7.6 is obtained.

### Electrode material

The PCS1, PCS2 and PCS3 cell stacks, all with 50 wt. % LSM and 50 wt. % doped ceria, was infiltrated with ceria. The percentage of NO removed together with the current efficiency (CE) can be found in table 7.2.

A theoretical amount of reduced NO can be calculated from the current. Assuming that NO is removed according to equation (7.1) one NO molecule is removed for each two electrons used.



The CE can then be calculated as the ratio between the amount of NO removed measured with MS and the theoretical amount removed calculated from the current, see equation (7.2). The CE for the porous cell stacks can be seen in table 7.4.

$$\text{Current efficiency} = \frac{\text{NO removed (measured)}}{\text{NO removed (I/(2F))}} \quad (7.2)$$

Table 7.2: Percentage of NO removed and CE for 13 layer porous cell stacks infiltrated with pure ceria in 0.1 % NO, gas flow of 33 mL/min and  $E = 4.5$  V vs OCV.

Temperature		PCS1	PCS2	PCS3
400 °C	NO removed	8 %	21 %	10 %
	CE	16 %	4 %	4 %
350 °C	NO removed	4 %	8 %	3 %
	CE	22 %	4 %	4 %
300 °C	NO removed	1 %	3 %	0 %
	CE	19	5 %	-

When the PCS1 cell stack was polarised with 4.5 V, it could remove 1 % NO of the NO present with a CE of 2 % in an atmosphere of 0.1 % NO + 5 % O<sub>2</sub> in Ar at 400 °C, but no activity was seen at lower temperature. None of the other cell stacks tested could remove NO in the presence of 5 % O<sub>2</sub>.

### Infiltration

Some of the PCS3b cell stacks were infiltrated with ceria, CGO10 and CPO20. The lowest temperature at which gas conversion was detected was at 300 °C.

According to equation (7.3) about half as much N<sub>2</sub> and O<sub>2</sub> should be formed as NO removed during polarisation.



The formation of N<sub>2</sub> and O<sub>2</sub> compared to removal of NO at steady state can be seen in table 7.3.

Table 7.3: N<sub>2</sub> and O<sub>2</sub> formed and NO removed at steady state for PCS3b cell stacks infiltrated with ceria, CPO20 and CGO10 and polarised with 4.5 V.

Infiltration	Temperature	$\Delta N_2$ /ppm	$\Delta O_2$ /ppm	$\Delta NO$ /ppm
CeO <sub>2</sub>	400 °C	54(2)	47(1)	-106(2)
	350 °C	10(4)	9(1)	-46(4)
CPO20	400 °C	28(2)	24(1)	-76(2)
	350 °C	12(3)	1(1)	-40(2)
	300 °C	4(1)	1(1)	-11(2)
CGO10	400 °C	29(3)	34(1)	-67(2)
	350 °C	12(3)	2(1)	-35(3)

The amounts of N<sub>2</sub> and O<sub>2</sub> formed at 400 °C are close to the anticipated from the amount of NO removed for all the three types of infiltration. But at lower temperatures, not nearly enough N<sub>2</sub> and O<sub>2</sub> are formed, especially some O<sub>2</sub> seems to be

lacking from the mass balance in three cases.

The concentration of NO decreased after start of polarisation and the concentration of  $N_2$  and  $O_2$  increased correspondingly, see figure 7.5 for an example of the change in NO concentration.

The percentage of NO removed when the cell stack was polarised with 4.5 V in an

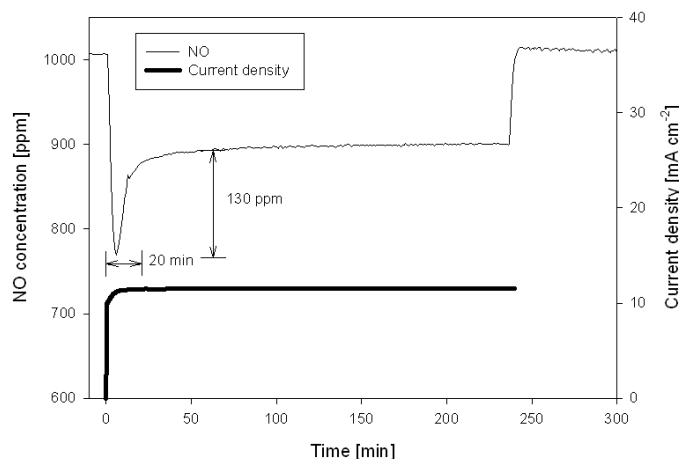


Figure 7.5: Change in NO concentration and current density during polarisation with 4.5 V on a 13 layer PCS3b cell stack infiltrated with CPO20, at 400 °C. The curve for NO concentration has been shifted approximately two minutes to the left on the time scale, corresponding to the time it takes a change in gas composition in the setup to be detected in the MS.

atmosphere of 1000 ppm NO in Ar can be seen in table 7.4 at different temperatures and with different type of infiltration. The cell stacks infiltrated with ceria have the highest activity.

Table 7.4: Percentage of NO removed and CE for PCS3b cell stacks infiltrated with ceria, CPO20 and CGO10 and polarised with 4.5 V.

Temperature		CeO <sub>2</sub>	CPO20	CGO10
400 °C	NO removed	10 %	7 %	8 %
	CE	3.0 %	6.0 %	7.4 %
350 °C	NO removed	5 %	3 %	4 %
	CE	2.9 %	5.4 %	12.2 %
300 °C	NO removed	0 %	1 %	0 %
	CE	0 %	4.0 %	0 %

The electrodes infiltrated with ceria, which removes the largest percentage of NO have the lowest CE. Generally the CE seems to drop with decreasing temperature, except for the cell stack infiltrated with CGO10, which is also the one with

the highest recorded CE of 12.2 % at 350 °C, but with only 35(2) ppm NO removed.

### Infiltration with ceria

The polarisation was varied for PCS3b cell stack infiltrated with ceria at 400 °C. For each step the cell was polarised for 2 h and allowed to wait for 1 hour and then the cycle was repeated. The voltages and corresponding decrease in NO concentration can be seen in figure 7.6.

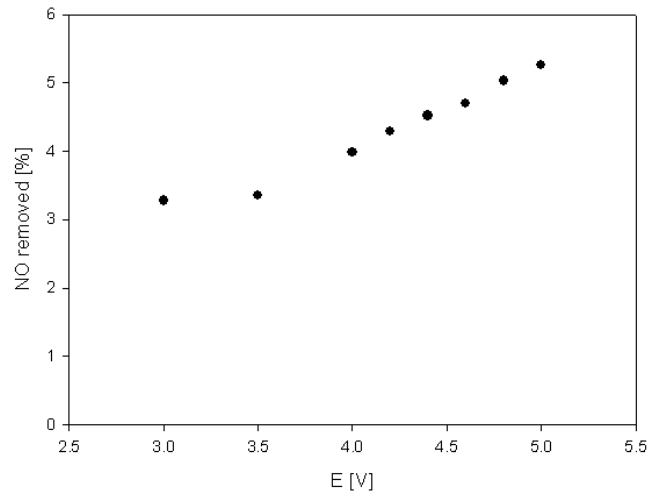


Figure 7.6: Decrease in NO concentration in percentage as a function of polarisation over a PCS3b cell stack infiltrated with ceria at 400 °C.

The decrease in NO concentration starts to show strong dependence on the polarisation, when the cell stack was polarised with 4 V ( $\approx 0.67$  V per cell) or more. But even at 3 V ( $=0.5$  V per cell) 3.3 % of the NO is removed.

The gas flow was varied between 10, 20, 33, and 40 mL/min for PCS3b cell stacks in 1000 ppm NO at 400 °C, and the cell stack was polarised with 4.5 V. The CE and percentage of NO removed as a function of gas flow can be seen in figure 7.7. The flow was 33 mL/min in all other measurements.

### Infiltration with CPO20

A PCS3b cell stack was infiltration 1, 4 and 5 times with CPO20. 7 and 17 % of NO was removed at 350 and 400 °C respectively for the cell stack infiltrated 4 times, more than double as much as for the cell stack only infiltrated once, see table 7.4. The cell stack infiltrated 4 times also showed activity at 250 °C, removing 1 % NO which was not observed with only one infiltration at these temperatures. The cell stack infiltrated five times showed the same activity as the cell stack infiltrated four times.

The effect on CE and removal of NO by increasing the voltage to more than 5 V over the cell stack can be seen in figure 7.8

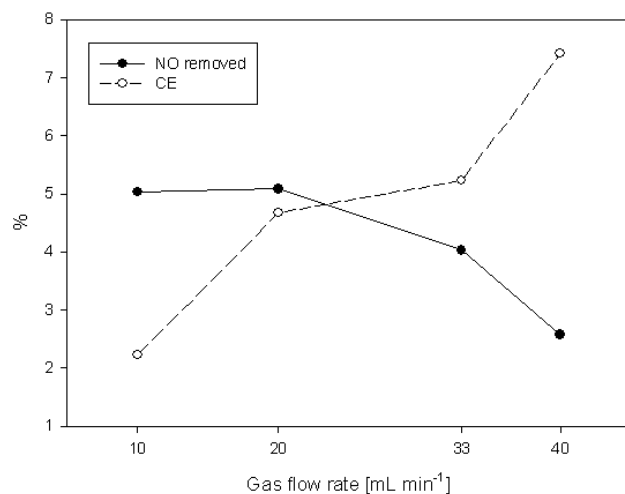


Figure 7.7: Decrease in NO concentration in percentage and CE as a function of gas flow over a PCS3b cell stack infiltrated with ceria at 400 °C.

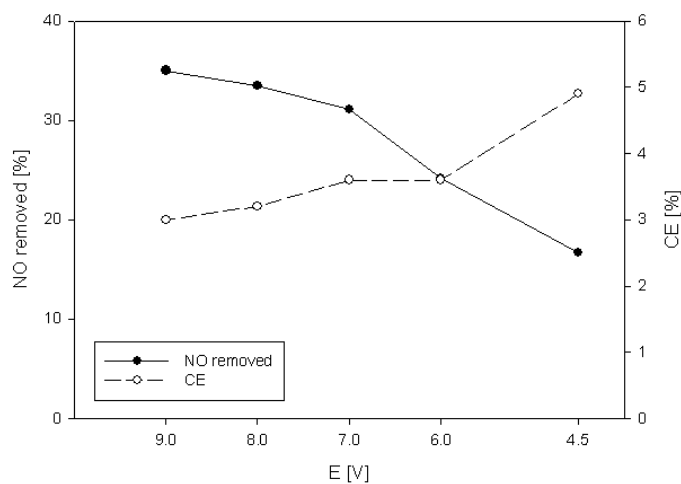


Figure 7.8: Percentage of NO removed and CE as a function of polarisation at 400 °C of a PCS3b cell stack infiltrated with CPO20 five times.

The electrode seems to become activated by polarisation with 9 V. For each polarisation with 9 V, the amount of NO removed increased, as illustrated in figure 7.9

## Deactivation

From the mass spectrometer graphs it is seen that initially right after the voltage was applied the cell stack removes much more NO than when steady state is reached, see figure 7.5. The current consumption shows no peak responding to the high initial activity of the cell, so the CE must be very high in the beginning of the polarisation period. For the measurement with polarisation at 3 V, see figure 7.10, it took much

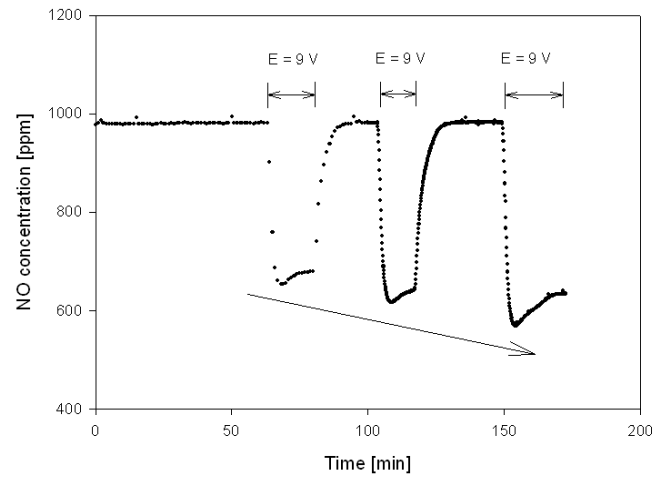


Figure 7.9: NO concentration during three sequential polarisations with 9 V over a PCS3b cell stack infiltrated with CPO20 at 400 °C.

longer time for the electrode to deactivate than for the measurements with higher polarisation.

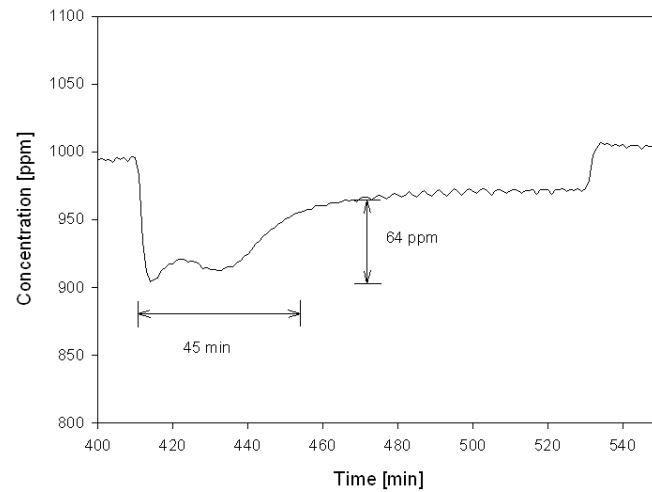


Figure 7.10: Change in NO concentration during polarisation with 3 V on a PCS3b cell stack at 400 °C.

The number of NO molecules converted as a function of time in the time period from the highest activity until steady state is reached forms a decaying function. A decaying exponential function of the type  $f(t) = a \cdot \exp(-b \cdot t)$  was fitted to the decaying function in order to achieve a measure of the time period before steady state is reached. A type of half-life can be calculated from  $b$ , as shown in equation

(7.4).

$$t_{\frac{1}{2}} = \frac{\ln(2)}{b} \quad (7.4)$$

Generally  $t_{\frac{1}{2}}$  seemed to increase with lower temperature, see figure 7.11, also the infiltration had an effect, but mostly at temperatures lower than 400 °C. The type

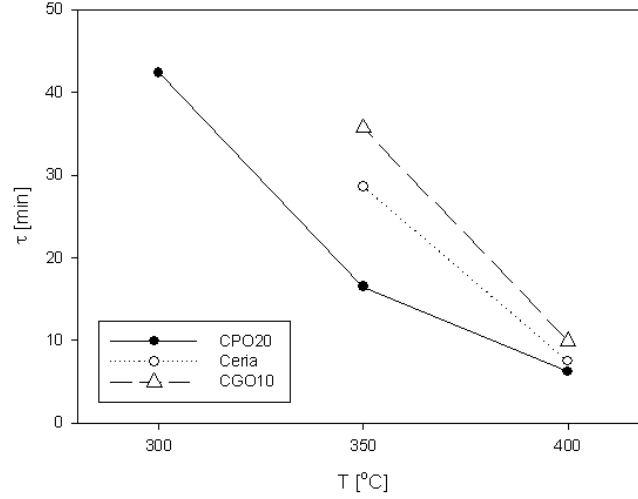


Figure 7.11:  $t_{\frac{1}{2}}$  as a function of temperature for PCS3b cell stack infiltrated with ceria, CPO20 and CGO10.

of electrode also had an effect on  $t_{\frac{1}{2}}$ , but again mostly at temperatures below 400 °C. The porous cell stacks with LSM15/CGO10 had the lowest  $t_{\frac{1}{2}}$  values, i.e. they deactivated very fast, while the PCS3b cell stacks with LSM50/CPO20 electrodes had the longest period before reaching stable level.

The flow rate also affected  $t_{\frac{1}{2}}$ , the higher flow the larger value for  $t_{\frac{1}{2}}$ .

## 7.4 Discussion

The cell in the porous stack is a type of symmetrical cell, and therefore the electrodes, except for the top and bottom ones, all work as both anodes (at one interface) and cathodes (at the other interface). Furthermore the gas stream flows through the porous structure, as both the electrode and electrolyte are porous, and therefore the NO is in contact with both anodes and cathodes, and the O<sub>2</sub> formed from decomposition of NO is also present throughout the system. So it is possible for NO to come into contact with anodes and be oxidised to NO<sub>2</sub>, and with 6 cells in series, NO<sub>2</sub> could be reduced again, to NO or N<sub>2</sub>. This cycle could repeat itself several times, while the gaseous molecules travel through the cell stack. The concentration of O<sub>2</sub> increases through the cell, if NO are decomposed according to equation 7.3, as more and more O<sub>2</sub> is formed, possible deactivating the cells activity towards reduction of NO. It is also likely that the O<sub>2</sub> could be reduced, followed by oxidation of the oxide ions afterwards, and that this cycle will repeat itself several times through the cell



stack. This could lead to considerable loss of power on irrelevant reactions, and in table 7.2 and 7.4 it is seen that the CE is very low for the cells, even though very little  $O_2$  is present.

The porous cell stacks can remove NO when polarised, but in most cases not when 5 %  $O_2$  is present. Only the PCS1 cell stack could remove approximately 1 % NO with 5 %  $O_2$  present, and only at 400 °C. CGO10 is used instead of CPO in the composite electrodes in the PCS1 cell stack, the LSM contains much less Sr, 15 % compared to 50 % for the PCS2 and PCS3 cell stacks and finally 10 times more  $MnO_x$  is present as the third phase.

The electrodes become less active towards removal of NO when the temperature decreases, only the cell stack infiltrated multiple times can remove NO down to 250 °C where the most active of the cell stacks infiltrated once could not remove NO at lower temperatures than 300 °C.

The cell stacks cannot remove NO, if they are not infiltrated. Several explanations can be made concerning the effect of the infiltration. Ceria is often used as an oxygen sink in three way catalysts, but the Ce ions do not change oxidation state as easily as Pr ions, making it an unlikely catalyst, and  $CeO_2$  has no significant electronic conductivity. Furthermore, the cell stacks PCS1, PCS2 and PCS3 have similar micro structure, but as seen in table 7.3 their ability to remove NO depends strongly on the types of electrodes. So the infiltration is causing the electrodes to be active, but the level of activity depends on the electrode material. One explanation could be that the ceria particles in the electrode improve the transport of oxide ions formed in the reduction of NO, see equation (7.3). The electrodes are mixed electrodes so CGO or CPO is already present, but the many small particles of ceria within the electrode could form a more network like structure expanding the triple phase boundary (TPB). Another explanation is that the infiltration modifies the surface chemistry of the electrodes in a way which makes them more active electrochemically [101]. The infiltrated particles could also work as scavengers capturing impurities in the electrodes, which impede the activity of the electrode. Infiltration of the cell stacks multiple times increases the activity and this could support both the theory with modified surface chemistry in the electrode and the scavenger role of ceria.

The PCS3b cell stacks infiltrated with ceria can remove more NO than similar electrodes infiltrated with CPO20 or CGO10, see table 7.4, which could point to the infiltrated particles changing the surface chemistry of the electrode, because CGO10 has a higher ionic conductivity than ceria, and CPO20 is the only one with noticeable electronic conductivity. The order is changed for the CE. The PCS3b porous cell stacks impregnated with ceria has the lowest CE, while the cell stacks impregnated with CGO10 has the highest current efficiency. An explanation could be that the ceria infiltrated electrodes have a low selectivity towards NO compared to  $O_2$ . Infiltration with ceria makes the cell stacks more active electrochemically (higher current density) than infiltration with CGO10 or CPO20, but when more NO is reduced, more  $O_2$  which can also be reduced is produced, leading to lower CE. For the PCS1 cell stack with electrodes of LSM15/CGO10 and infiltrated with pure ceria the highest CE is found - 22 % at 350 °C, with the same level of NO removed

(4 %) as for the PCS3b cell stacks infiltrated with pure ceria. So the cells with the highest CE have either been impregnated with CGO10 or have composite electrodes containing CGO10. Thus CGO10 seems to increase the selectivity of the electrodes. Table 7.2 shows that the PCS2 cell stack with LSM50/CPO10 electrodes have the highest activity among the cell stacks only infiltrated once and removes 21 % NO at 400 °C, but with a CE of 4 % which is considerable lower than the CE of 16 % for the PCS1 cell stack. The microscopy examination also showed the PCS2 cell stack to have thicker electrodes than the other cell stacks. Maybe this could influence the activity, or the presence of CPO10 instead of CPO20 makes the electrodes more active. The PCS2 cell stacks also had lower surface area than all the other cell stacks, see table 7.1. This is surprising as a higher surface area is assumed to be equal to more active sites which in turn would give a more active catalyst. The assumption of the infiltration changing the surface chemistry of the electrodes could, however, explain this.

Previous work with electrodes of LSM15/CGO10, LSM50/CPO10 and LSM50/-CPO20 on symmetrical and three electrode cells showed that the LSM50/CPO20 electrodes had the highest selectivity at low temperatures, and that the LSM15/CGO10 electrodes had the highest activity at 600 °C [99]. The results from this study is in contradiction with the earlier results. The electrodes in the earlier study were not infiltrated, and even though they were porous, the gas did now flow through the electrodes the same way as with the porous cell stacks. Again this indicates that the infiltration modifies the surface chemistry of the electrodes, and this is affecting the electrodes not only with respect to activity but also selectivity. The design of the cell stacks with porous structure also seems to have an effect, as gas conversion was only observed with MS at 600 °C in the earlier studies.

It would be preferable if the NO decomposed, with N<sub>2</sub> and O<sub>2</sub> being the only products, thereby avoiding forming new poisonous nitrogen oxide compounds such as N<sub>2</sub>O and NO<sub>2</sub>. The increase in O<sub>2</sub> and N<sub>2</sub> corresponds to the decrease in NO at 400 °C, but at lower temperature not enough N<sub>2</sub> and O<sub>2</sub> are formed. So another mechanism for NO breakdown is taking place at low temperatures. Especially the increase in concentration of O<sub>2</sub> is too small compared to the decrease in NO concentration. This could indicate that NO<sub>2</sub> might be formed instead at lower temperatures.

Initially all the cell stacks show high activity followed by a drop in activity, where after the rate of NO removal becomes steady. The period before the drop in activity is longer when the cell is polarised with 3 V, than at a potential of 4.5 V. If it was possible to sustain the activity level from 410 to 440 min of approximately 8 % NO removed, see figure 7.10, then the activity with a potential of 3 V is comparable to the activity of 10 % NO removed with a potential of 4.5 V. But the CE would be as high as 20 %. Increasing the voltage also affects the deactivation, as the drop in activity is much smaller at 9 V than at 4.5 V, see figure 7.9 compared to figure 7.5. The deactivation of the cell stacks during polarisation could be caused by formation of some unwanted side product, which blocks the active sites or, alternatively, the reaction depending on an intermediate, which is depleted, so the reaction with this is the limiting step. The measurement with a polarisation of 3 V (= 0.5 V over each cell), where the deactivation was limited, also had a quite high CE of 8 %. This

must mean that less current density is wasted on other reactions than the reduction of NO, possibly supporting the theory with an unwanted side product being formed. When the cell stack is polarised with 9 V (=1.5 V over each cell), not only was the deactivation during the polarisation very small, but the cell stack was also activated afterwards and removed a larger amount of NO in a following polarisation period with 9 V, see figure 7.9. This was only seen for polarisation with 9 V. An explanation could be that the polarisation of 1.5 V for each cell changed the composition of the electrode, and the higher activity was a result of this.

A simple explanation for the deactivation could be the O<sub>2</sub> formed from NO decomposition poisons the NO reduction on the electrodes. The initial period time before deactivation seems to be the same for all electrodes and infiltrations. The time before deactivation is dependent on temperature, the initial period with high activity is longer at lower temperatures, but a lower reaction rate would also be expected at lower temperatures and thereby a slower formation of poisoning O<sub>2</sub>. For the measurements with varying flow rate, see figure 7.7, the initial period varies with flow speed. It takes longer time before deactivation at the high flow rates, indicating that whatever is causing the deactivation is blown away. This could point to the formation of oxygen from NO decomposition being responsible to the deactivation. Some 250 ppm O<sub>2</sub> is, however, present in the atmosphere all the time, and the amount of O<sub>2</sub> formed does not even come close to this amount. It seems unlikely that the small amounts of O<sub>2</sub> formed could deactivate the electrodes, when the 250 ppm O<sub>2</sub> present all the time does not completely stop the activity of the cells. It is however possible that the activity of the cell stacks would be even higher than observed, if the gas stream did not contain any O<sub>2</sub>.

## 7.5 Conclusion

Infiltration of the cell stacks is necessary for NO decomposition to take place. The cell stacks infiltrated with ceria has the highest activity, while infiltration with CGO10 increased the current efficiency and the selectivity. Multiple infiltrations increased the activity drastically, and it is clear that one infiltration (8 mg/cm<sup>2</sup>) is not sufficient.

The cell stacks could remove NO, while polarised, in the temperature range 250 to 400 °C, with highest activity at high temperatures. The increase in concentration of N<sub>2</sub> and O<sub>2</sub> corresponded to the decrease in NO at 400 °C, indicating decomposition of NO without formation of NO<sub>2</sub> or N<sub>2</sub>O. A cell stack with LSM50/CPO20 electrodes impregnated four times with CPO20 could remove 17 % of NO present at 400 °C when polarised with 4.5 V (= 0.75 V for each cell). When polarised with 9 V (= 1.5 V for each cell) the stack with 6 cells could remove up to 35 % of NO present.

The porous cell stack with LSM15/CGO10 electrodes could remove 1 of the % NO with a current efficiency of 2 % when 5 % O<sub>2</sub> was added to the atmosphere at 400 °C. The highest current efficiency was also found for the porous cell stack with LSM15/CGO10 electrodes, 22 % at 350 °C. The fact that the cell stack impregnated with CGO10 shows activity in the presence of 5 % O<sub>2</sub> and the cell stack with

electrodes of LSM15/CGO10 has high CE, indicates that CGO10 is likely increasing the selectivity of the electrodes.

The infiltration of the cell stacks seem to modify the surface chemistry of the electrodes both with respect to activity and selectivity, when the present results are compared to previous work with electrodes of the same materials which had not been infiltrated.

# Chapter 8

## The special LSM15/CGO10 porous cell stack

### 8.1 Introduction

The results presented in this chapter are the results from the first measurements on a porous cell stack. The results were very good, but it was unfortunately not possible to reproduce the results, although several attempts were made. It was not determined why this particular porous cell stack had such high activity. The results are presented here merely as a measure for how well the porous cell stacks actually can perform with further optimisation.

### 8.2 Experimental

An 11 layer porous cell stack was made by laminating layers of electrode and electrolyte tapes.

The electrolyte tape is made of CGO10, which was purchased from Rhodia A/S, while the composite electrode was 50 wt. % CGO10 and 50 wt. % LSM15, from Haldor Topsoe A/S. Slurries for tape casting were made from metal oxide powder, solvent, binder and carbon (pore former). The slurries were ball milled before tape casting.

Alternating layers of dried electrolyte and electrode tapes were laminated together with a MailTech laminating machine. The cell stack had 11 layers, corresponding to 5 cells in a stack. Afterwards a round cell stack was cut and sintered at 1250 °C. The sintered cell stack was grinded on the sides; to avoid short circuit from the LSM powder and to achieve a diameter of 12 mm. Gold paste with 20 wt. % carbon (pore former) was painted on both sides of the porous cell stack. The cell stack was mounted between the two alumina tubes, as shown in figure 8.1, with contact between the gold paste and the two Pt-electrodes. Gold rings and glass was used as sealings, and the setup was inside a glass tube with Ar purge gas. The gas stream went through the porous cell, and not just above the surface of the electrode as with the 3 electrode pellets. A furnace was mounted vertically surrounding the setup, and the cell and sealings were heated to 1000 °C in order to make the sealings air

tight.

A Hitachi TM 1000 SEM was used for examining the micro structure of the porous cell stacks. The gas flow was 25 mL/min and the composition was 1000 ppm NO in

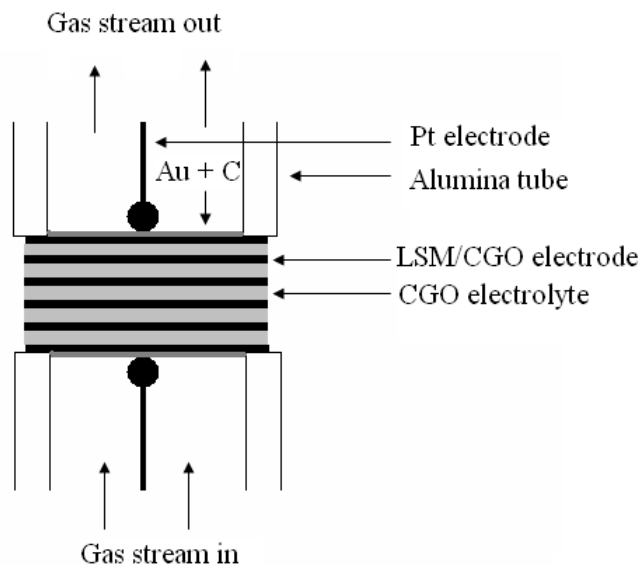


Figure 8.1: Setup of porous cell in 3 electrode rig.

Ar or 1000 ppm NO + 4 % O<sub>2</sub> in Ar. The temperature range for the measurements was 300 to 450 °C.

The cell stack was subjected to CV and chronoamperometry with a Solartron 1287 + 1255B. The outlet gas composition was monitored with an MS from Pfeiffer, the Omnistar GSD 301. It was possible to make the system almost completely airtight, the mass spectrometer only showed very small peaks of N<sub>2</sub> and O<sub>2</sub> which could come from small leaks in the system, or from decomposition of NO over the cell.

## 8.3 Results

### 8.3.1 Microscopy

The SEM examination of the porous cell stacks revealed that both the electrodes and electrolytes had a porous structure, which allows the gas to flow through the cell stack. The thickness of the cell was approximately 350  $\mu\text{m}$ , and the average thickness of the electrode and electrolyte layers were 40  $\mu\text{m}$  and 25  $\mu\text{m}$  respectively. A SEM micrograph of the profile of a porous cell stack similar to the one tested is shown in figure 8.2.

### 8.3.2 Electrochemical results

A cyclic voltammogram with -2.0 V and 2.0 V as limiting potentials at scan rate 5.0 mV/s was recorded. The current density when the voltage was -2.0 V was 130

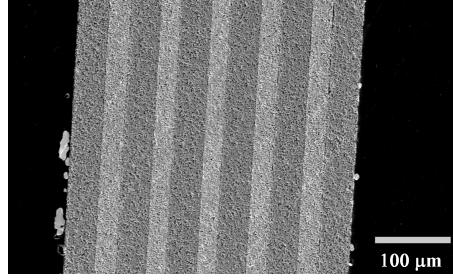


Figure 8.2: SEM micrograph of an 11-layer porous cell stack with remains of gold paste left on the sides.

$\mu\text{A}/\text{cm}^2$ , which, assuming all the current is used for reduction of NO, corresponds to a conversion of only 1.25% of the NO molecules present. Therefore it was assumed that NO conversion could not be seen at 300 °C.

The temperature was raised to 400 °C, where a cyclic voltammogram with -3.5V and 3.5V as limiting potentials was recorded. Now the maximum current density was  $4.4 \text{ mA}/\text{cm}^2$ , which corresponded to a conversion degree of 0.517.

The CV showed some peaks, so cyclic voltammograms were recorded at different scan rates, to see if there were diffusion limitations or reduction/oxidation of species. The result can be seen in figure 8.3. The sweep with the lowest scan rate is the one with the smallest area, so this could point to some diffusion limitations. The two sweeps with scan rate 5 and 10 mV/s each shows peaks, while the one with the highest scan rate has the largest area.

The cell stack was polarised with 3.5 V (=0.7 V for each cell). A drop in the

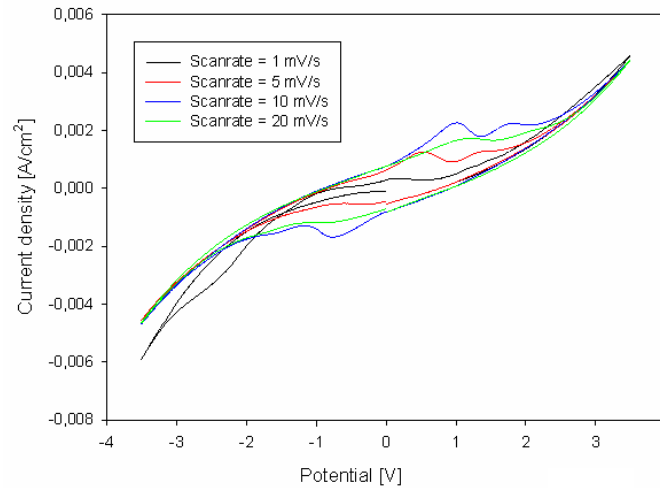


Figure 8.3: Cyclic voltammograms with different scan rates at 400 °C in Ar with 1000 ppm NO.

NO concentration was seen immediately after the start of polarisation, and when the polarisation was stopped, the NO concentration returned to normal level. The percentage of NO removed at stable state along with the corresponding CE can be seen in figure 8.4 the atmosphere was 1000 ppm NO in Ar. All NO present

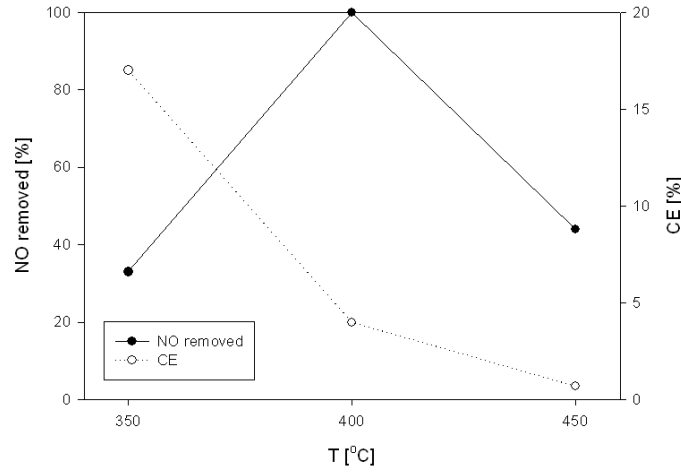


Figure 8.4: Percentage of NO removed and CE for a cell stack polarised with 3.5 V at 400 °C in Ar with 1000 ppm NO.

was removed from the gas stream at 400 °C, even though the calculation from the maximum current density measured during CV estimated only around 50 %. But the current density increased during polarisation, and so did the activity of the cell stack. When the cell stack was polarised at 450 °C, the cell stack had high activity and after 20 minutes of polarisation NO could not be traced in the gas stream. But after 120 minutes of polarisation the activity of the cell stack decreases and the NO removal rate drops to 40 %. This pattern is easily seen in the corresponding current density, see figure 8.5, the current density drops as the activity falls.

The amounts of  $N_2$  and  $O_2$  formed corresponds well with what should be expected, if all NO removed was converted into  $N_2$  and  $O_2$ . 4 %  $O_2$  was added to the gas stream

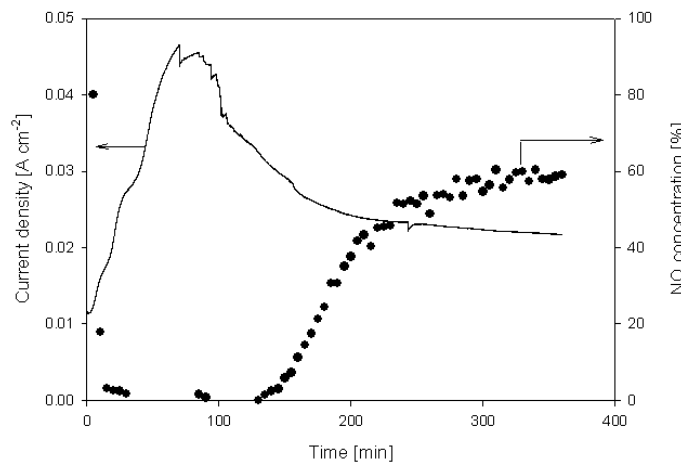


Figure 8.5: Percentage of NO present and current density for a cell stack polarised with 3.5 V at 450 °C in Ar with 1000 ppm NO.

and the polarisation measurements repeated. It was still possible for the cell stack



to remove NO, but the activity was not as high as for the measurements without O<sub>2</sub> in the gas stream, see figure 8.6. Formation of N<sub>2</sub> from NO decomposition was only seen at 350 °C, at the higher temperatures no N<sub>2</sub> formation was seen. For all the

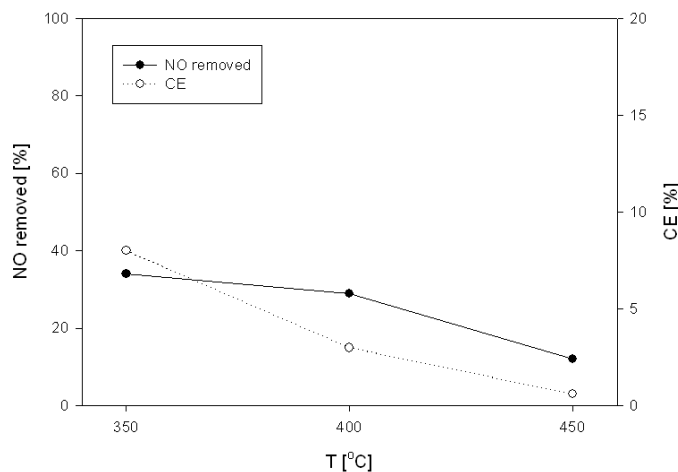


Figure 8.6: Percentage of NO removed and CE for a cell stack polarised with 3.5 V at 400 °C in Ar with 1000 ppm NO and 4 % O<sub>2</sub>.

measurements without O<sub>2</sub> present N<sub>2</sub> was formed in stoichiometric amounts. When 4 % O<sub>2</sub> was added to the gas stream then sufficient N<sub>2</sub> was formed at 350 °C, while some was lacking at higher temperatures.

## 8.4 Discussion

There is a maximum in the conversion of NO with respect to temperature at 400 °C. The CE is highest at low temperatures and decreases with increasing temperature, both for measurements with and without O<sub>2</sub> present. The maximum in conversion could be a simple effect of CE decreasing with temperature combined with electrochemical activity of the cells increasing with temperature, and then 400 °C is the optimum temperature for a combination of the two parameters. The cell stack simply deactivates after a while with 100 % removal of NO for the measurement at 450 °C, and this trend is observed as well in the current density, which also decreases after a while. So the deactivation is not caused by the electrodes reducing something else than NO, like O<sub>2</sub>, but it simply becomes less active electrochemically. This could be due to something blocking the active sites. The activity of the cell stack was not permanently damaged, a succeeding polarisation at 400 °C could still remove all NO present.

### 8.4.1 Comparison with later results

The special cell stack had much better performance than any of the cell stacks tested in chapter 7. Not only could it remove all NO present at 400 °C, but even with

4 %  $O_2$  in the gas stream the cell stack could remove 34 % of the NO present at 350 °C, and the amount of  $N_2$  formed corresponded to reduction of NO and not formation of  $NO_2$ . This cell stack was not even infiltrated and it had been warmed up to around 1000 °C prior to the test, in order to make the Au sealing soft. Thus it is very surprising that the cell stack had as much activity as it had.

The selectivity seemed to decrease with temperature for the series of infiltrated porous cell stacks in chapter 7, only at 400 °C was it possible for the LSM15/CGO10 cell to remove NO with 5 %  $O_2$  present. For the special cell stack the opposite was seen, the selectivity increased when the temperature decreased. But this tendency seen for the special cell stack is in accordance with what should be expected from the CV measurements on three electrode pellets, where the selectivity also increases with decreasing temperature.

Comparing the cyclic voltammograms for the old cell stack, figure 8.3 with some for one of the infiltrated cell stack, figure 7.4 there is a clear difference. There are multiple peaks present in the voltammogram for the old cell stack for the high scan rates, while there are no peaks in figure 7.4. Further the current density is higher for the special cell stack, than for the uninfiltrated new cell stack. Thus the new cell stacks are less electrochemically active than the old one was. Although the infiltrated cell stacks have slightly higher current density than the old, they still cannot remove NO in the presence of  $O_2$ , so the selectivity must also be better for the special cell stack.

The peaks in the voltammogram could be due to nitrates forming, or reduction of NO, with no reference electrode present it is not possible to locate the position of the peak, preventing an identification of the peak.

# Chapter 9

## Discussion

It was found that the electrodes are not electrochemically reactive towards NO around OCV, but the EIS measurements on electrodes under polarisation indicate that the kinetics of the electrode reactions changes when the polarisation of the electrodes is -0.6 V vs Pt/air or lower. The EC of the LF arc increases very sharply for impedance measurements at these low potentials. This indicates that another process, than at OCV, is now the less hindered path. The MS also shows gas conversion for polarisation with -0.6 V vs Pt/air or lower with formation of N<sub>2</sub>. So at potentials of -0.6 V vs Pt/Air or below at 600 °C the electrodes can react directly with NO, which is reduced with formation of N<sub>2</sub>.

Generally the cyclic voltammetry measurements indicate that the selectivity of the electrodes increase, when the temperature decreases. The measurements on the special porous cell stack show selectivity increasing with decreasing temperatures, which corresponds with the predictions from the cyclic voltammetry measurements on three electrode cells. But the infiltrated cell stacks do not show selectivity, and their activity does not correspond to what is predicted from CV measurements on the three electrode cells. The three electrodes cells were not infiltrated like the new cell stacks were. This could have an effect on the selectivity.

Infiltration has a large effect on the activity of porous cell stacks; in fact hardly any activity is seen for the new cell stacks, when not infiltrated. The cells infiltrated with pure ceria have the highest activity, compared to infiltration with CGO10 and CPO20. This is surprising as ceria does not have any significant electronic or ionic conductivity; whereas CGO is a good ionic conductor and CPO also have some electronic conductivity besides the ionic conductivity. Thus the increase in activity for the infiltrated cell stacks is not caused by a larger TPB. Also pure ceria is not supposed to have any catalytic activity, so the higher activity is not due to NO reacting with the ceria. It has been suggested [101] that decreased  $R_p$  for infiltrated electrodes is due to the infiltration changing the surface chemistry of the electrodes. This could explain the observations with infiltration of the porous cell stacks. The activity of the electrodes also does not fit with the predictions from the CV measurements on the three electrodes cells, which were not infiltrated.

The electrode with the lowest area specific resistance (ASR) in air at 600 °C is LSCF40/ CPO20 with a resistance of  $0.44 \pm 0.01 \Omega\text{cm}^2$ , which is far lower than the  $2.9 \pm 0.5 \Omega\text{cm}^2$  achieved for the LSM50/CPO20, which was the best air electrode

among the LSM based electrodes. All the ferrite based electrodes have lower ASR in air than the LSM electrodes in the temperature range of 400 to 600 °C. This is in line with expectations, as LSCF based electrodes have been suggested as replacement for LSM cathodes in IT-SOFC [72], and especially LSCF40 attracts attention [73]. The results from the LSM based electrodes show that composite electrodes with CPO20 have lower ASR than electrodes with CPO10, both in air and in 1 % NO in Ar. Further the LSCF40/CPO20 electrode have lower ASR than the LSCF40/CGO10 composite electrode in both air and 1 % NO in Ar in the temperature range of 500 to 600 °C. Thus addition of CPO20 has a positive effect on the electrodes electrochemical activity, and CPO with the highest level of Pr doping have the largest effect. CPO20 has some electronic conductivity, and the Pr ions can relatively easily change oxidation state between +3 and +4 compared to CGO10 which have good ionic conductivity.

The impedance measurements on the symmetrical cells indicate that the electrodes are not very good air electrodes at low temperatures, as the  $R_p$  for electrodes in 1 % NO or NO<sub>2</sub> in Ar are lower than in air. For the LSM containing electrodes the LF arc cannot be separated from the other arcs in 1 % NO in Ar at 300 °C. This is either due to  $R_{LF}$  being insignificant in size compared to  $R_{MF}$ , which has a higher  $E_a$ , or due to electrodes reacting through another pathway with NO at 300 °C. For the electrodes with LSF and LSCF the LF arc can still be identified at 300 °C, possible because these electrodes are not as good catalysts for the formation of NO<sub>2</sub> from NO than LSM.

The large LF arc dominates the impedance spectra for symmetrical cells in 1 % NO in Ar at high temperatures. This arc resembles a semicircle, and the  $\alpha$  value is typically between 0.9 and 1, it has a high EC value and the  $E_a$  value is very low. All this points to a type of conversion arc, except that the resistance of the LF arc increases with increasing flow rate, the opposite of what would be expected for a conversion arc. It is therefore suggested that the LF arc is a type of conversion arc resulting from low concentration of an intermediate, by which the electrodes react electrochemically instead of NO. NO cannot be the low concentration intermediate, otherwise the resistance of the LF arc should decrease with increasing flow rate.

Thus the electrodes do not react electrochemically with NO, or the reaction with NO has a very high resistance compared to the reaction with the intermediate. The increasing flow rate removes the intermediate from the surface of the electrode faster, before reaction can take place, and thereby lowers the concentration of intermediate at the surface of the electrodes. This can explain why the resistance of the LF arc increases with increasing flow rate. The intermediate must be a species related to NO, as only NO and Ar are present in the atmosphere. A possible candidate could be NO<sub>2</sub>, it has been shown in literature that some perovskites can form NO<sub>2</sub> from NO by heterogen catalysis [71]. The XANES measurements also indicate that CPO is capable of forming NO<sub>2</sub> from NO catalytically. Another possible intermediate could be N<sub>2</sub>O, but this is unlikely as the  $R_p$  for electrodes in 1 % N<sub>2</sub>O are much larger than when the atmosphere is 1 % NO in Ar. The measurements on three electrodes cells show a leak of O<sub>2</sub> into the system. Therefore it should be considered that the LF arc could arise from the electrodes reacting with O<sub>2</sub> in low concentrations from a leak.

This explanation corresponds well with the increasing  $R_{LF}$  with flow rate, as the  $O_2$  leak in the three electrode setup becomes less significant with higher flow rate. These measurements on the three electrode cells are, however, made on an entire different setup, which requires the use of Ag and glass sealings, not rubber O-rings as in the setup for symmetrical cells. Further the symmetrical cell setup was tested for leaks, so there is no reason to assume any leaks there. The results also indicate that leaking  $O_2$  is not responsible for the LF arc, as the LF arc should have been present in the impedance spectra recorded in  $N_2O$ , if leaking  $O_2$  was responsible for the LF arc. The size of the resistance of the LF arc also varied with the electrode material, the electrodes with LSM50 had lower  $R_{LF}$  than the electrodes with LSF and LSCF, which had between 25 or 40 % Sr. This is consistent with the observation by Hansen *et al.* [71] that the electrodes with high Sr content having higher activity for formation of  $NO_2$ . Also some of the tests with symmetrical cells were done with two LSM50/CPO10 electrodes and two LSM50/CPO20 electrodes in the setup with room for four electrodes at a time. In this case all the electrodes should be affected by the same level of  $O_2$  if a leak was present, but the LSM50/CPO20 electrodes still had lower  $R_{LF}$  than the LSM50/CPO10 electrodes.

Further if  $NO_2$  is formed from  $NO$ , in an environment without  $O_2$  present, then the oxygen must come from electrodes and the electrodes should therefore slowly degrade, and this is observed. The OCV measurements in the three electrodes experiments show dependence on the gas flow rate. This can be partly explained by the  $O_2$  leakage also being dependent on the flow rate, but calculations also shows that another reaction must be taking place as well, this is in accordance with formation of  $NO_2$  from  $NO$ .



# Chapter 10

## Conclusion and outlook

### 10.1 Conclusion

All the electrodes tested could reduce NO when polarised, and  $N_2$  was formed. In case of the electrodes on three electrode pellets conversion of NO is only observed at 600 °C. This is due to limited contact between the gas stream and the electrode. Therefore the porous cell stack design is optimal for testing the electrodes for activity at lower temperatures, as they provide very good contact between the gas and the electrode.

It was unfortunate that the results with the special porous cell stack with  $La_{0.85}Sr_{0.15}MnO_3$  (LSM15) and  $Ce_{0.9}Gd_{0.10-\delta}$  (CGO10) electrodes could not be reproduced, but the experiment clearly showed that the design has a high potential with respect to the activity of the cell stack.

The infiltrated porous cell stacks did not show activity without infiltration, and all the three types of infiltration, pure ceria, CGO10 and  $Ce_{0.8}Pr_{0.20-\delta}$  (CPO20), had a strong effect on the electrodes. Infiltrating the cell stacks with ceria gave the largest increase in electrochemical activity, while infiltration with CGO10 had the best effect on the current efficiency (CE). The cell stack with electrodes with LSM15/CGO10 also had the highest CE. The infiltration seemed to change the surface chemistry of the electrodes both with respect to activity and CE, and the results from the infiltrated porous cell stacks did not correspond well with the results from measurements on electrodes, which were not infiltrated. It is important to infiltrate the cell stacks sufficiently; the cell stacks which had an infiltration load of 30 mg/cm<sup>2</sup> or more had higher electrochemical activity than the cell stacks with only 8 mg/cm<sup>2</sup>.

NO decomposition could be observed down to 250 °C for the porous cell stacks, which was in the temperature range of diesel exhaust. The activity and selectivity was very low, but the results from the special cell stack showed that improvement is possible. Further the special cell stack had the highest selectivity and best activity with 4 %  $O_2$  present at 350 °C. The most active infiltrated porous cell stack could remove up to 35 % of the NO present, but this was only without  $O_2$  present.

The CV and impedance measurements on electrodes without infiltration predicted selectivity towards NO compared to  $O_2$  at lower temperatures, but this was not

confirmed by the measurements on porous cell stacks. Only the cell stack with LSM15/CGO10 could remove NO in the presence of 5 % O<sub>2</sub> and the activity and CE was still very low.

The LSM50/CPO20 electrode seemed to be the most selective electrodes in the temperature range of 300 to 400 °C, which was close to the temperature of the diesel exhaust 200-300 °C. The La<sub>1-x</sub>Sr<sub>x</sub>Co<sub>1-y</sub>Fe<sub>y</sub>O<sub>3-δ</sub> (LSCF) and La<sub>1-x</sub>Sr<sub>x</sub>FeO<sub>3-δ</sub> (LSF) based electrodes with CPO20 had lower polarisation resistance ( $R_p$ ) in NO than in air at low temperatures and their activation energies in 1 % NO in Ar were lower than the corresponding electrodes with CGO10. So addition of CPO20 seemed to increase the selectivity of composite electrodes.

The impedance measurements indicated that the composite electrodes did not react electrochemically with NO around OCV. The electrodes reacted instead with an intermediate, which was formed catalytically from NO by the electrode materials, i.e. without any electrochemical reaction. NO<sub>2</sub> was a likely candidate for this intermediate, as perovskites are known to catalyse the oxidation of NO, and also the XANES measurements indicated that CPO could be oxidising NO.

The electrodes had higher selectivity with decreasing temperature. This was indicated by both cyclic voltammetry (CV) and  $R_p$  values from impedance measurements. The activation energy for the  $R_p$  ( $R_p$ ) of the electrodes was strongly dependent on the atmosphere; electrodes in air had much higher activation energy than in 1 % NO in Ar. This was partly due to the fact that impedance spectra for electrodes in 1 % NO in Ar were dominated by a large low frequency arc. The low frequency arc was a type of conversion arc, with very low activation energy. The conversion arc was resulting from low concentration of an intermediate formed catalytically. Therefore the resistance of the arc increased with increasing flow rate, opposite of the expected behaviour of a typical conversion arc.

The composite electrodes based on LSCF and LSF had very low  $R_p$ s in air compared to the electrodes based on LSM. The low frequency conversion arc from the measurements in 1 % NO in Ar was even more dominating than for the LSM electrodes, likely due to the LSCF and LSF electrodes being less catalytically active in producing NO<sub>2</sub>, decreasing the concentration of this intermediate.

The electrodes could react directly with NO when they were polarised about -0.6 V vs Pt/air or more. NO conversion and N<sub>2</sub> formation were detected during polarisation. The impedance measurements under polarisation showed that another process takes place at potentials below -0.6 V vs Pt/Air, the potential below which the electrodes became electrochemically active towards reduction of NO.

## 10.2 Outlook

Infiltration seems to have a significant effect on the activity of the electrodes, and this should be examined further. Measurements on infiltrated electrodes on symmetrical cells and three electrode cells would be vital in the understanding of the processes by which the infiltration affects the electrodes.

The porous cell stacks provide opportunity to test the electrode materials in the



appropriate temperature range and simultaneously observe gas conversion. This is much more reliable than calculating selectivity from current densities, without knowing exactly which processes that contributed to the currents. Furthermore manufacturing a filter from many cell stacks could actually be an applicable solution for cleaning real exhaust. The thoughts behind the cell stack was that they should also be capable of oxidising CO and unburned fuel along side with the reduction of NO, as the exhaust stream come into contact with both the anodes and cathodes on its way through the cell stack. Assuming that one round cell stack with a diameter of 8 mm, like the special cell stack, can clean the 25 mL/min exhaust passing through, then a 0.5 l diesel engine which produces 40 m<sup>3</sup> exhaust per hour would require a filter of porous cell stacks with an area of approximately 3 m<sup>2</sup> in order to remove all NO from an exhaust stream with 1000 ppm NO + 4 % O<sub>2</sub> at a temperature of 350 °C. This could seem like a large area for a unit for exhaust treatment for one small vehicle, but with the proper design of the filter unit and improvement in performance, then it might be feasible.

The initial experiments with the special porous cell stack clearly showed that high activity and selectivity can be obtained with these cell stacks. Naturally effort should be put into reproduction of the initially tested cell stack. Further, the cell stack might be improved with respect to electrode materials and infiltration. Infiltrating the electrodes had a very positive effect on the activity, but the mechanism behind is not established and only ceria based infiltration was tested.



# Bibliography

- [1] Y. Zeldovich, Oxidation of nitrogen in combustion and explosion, Academie des sciences de l'URSS – Comptes Rendus 51 (3) (1946) 217–220.
- [2] S. Roy, M. Hegde, G. Madras, Catalysis for NO<sub>x</sub> abatement, Appl. Energ. 86 (2009) 2283–2297.
- [3] F. Garin, Mechanism of NO<sub>x</sub> decomposition, Appl. Catal. A: Gen. 222 (2001) 183–219.
- [4] H. Glick, J. Klein, W. Squire, Single-pulse shock tube studies of the kinetics of the reaction  $\text{N}_2 + \text{O}_2 \leftrightarrow 2\text{NO}$  between 200–3000 K, J. Chem. Phys. 27 (4) (1957) 850–857.
- [5] H. Bosch, F. Janssen, Formation and control of nitrogen oxides, Catal. Today 2 (1988) 369–379.
- [6] V. Pârvulescu, P. Grange, B. Delmon, Catalytic removal of NO, Catal. Today 46 (1998) 233–316.
- [7] P. Crutzen, C. Brühl, Catalysis by NO<sub>x</sub> as the main cause of the spring to fall stratospheric ozone decline in the northern hemisphere, J. Phys. Chem. 105 (2001) 1579.
- [8] J. Armor, Environmental catalysis, Appl. Catal. B 1 (1992) 221–256.
- [9] F. Klingstedt, K. Arve, K. Eränen, D. Murzin, Toward improved catalytic low-temperature NO<sub>x</sub> removal in diesel-powered vehicles, Acc. Chem. Res. 39 (2006) 273–282.
- [10] A. Fritz, V. Pitchon, The current state of research on automotive lean NO<sub>x</sub> catalysis, Appl. Catal. B: Environ. 13 (1997) 1–25.
- [11] R. Burch, J. Breen, F. Meunier, A review of the selective reduction of NO<sub>x</sub> with hydrocarbons under lean-burn conditions with non-zeolitic oxide and platinum group metal catalysts, Appl. Catal. B: Environ. 39 (2002) 283–303.
- [12] G. Koltsakis, A. Stamatelos, Catalytic automotive exhaust aftertreatment, Prog. Energy Combust. Sci. 23 (1997) 1–39.
- [13] [Http://www.dieselnet.com/standards/eu/ld.php](http://www.dieselnet.com/standards/eu/ld.php) 07-02-2010.

- [14] R. Lanza, E. Eriksson, L. Pettersson, NO<sub>x</sub> selective catalytic reduction over supported metallic catalysts, *Catal. Today* 147S (2009) S279–S284.
- [15] P. Forzatti, I. Nova, L. Castoldi, NO<sub>x</sub> removal catalysis, *Chem. Biochem. Eng. Q.* 19 (4) (2005) 309–323.
- [16] S. Matsumoto, DeNO<sub>x</sub> catalyst for automotive lean-burn engine, *Catal. Today* 29 (1996) 43–45.
- [17] Z. Liu, S. Woo, Recent advances in catalytic deNO<sub>x</sub> science and technology, *Catal. Rev.* 48 (2006) 43–89.
- [18] K. Kammer, Electrochemical deNO<sub>x</sub> in solid electrolyte cells - an overview, *Appl. Catal. B: Environ.* 58 (2005) 33–39.
- [19] S. Pancharatnam, R. Huggins, D. Mason, Catalytic decomposition of nitric oxide on zirconia by electrolytic removal of oxygen, *J. Electrochem. Soc.* 122 (7) (1975) 869–875.
- [20] T. Gür, R. Huggins, Decomposition of nitric oxide on zirconia in a solid-state electrochemical cell, *J. Electrochem. Soc.* 126 (1979) 1067–1074.
- [21] D. Cicero, L. Jarr, Application of ceramic membranes in advanced coal-based power generation systems, *Sep. Sci. Technol.* 25 (13-15).
- [22] G. Reinhardt, H.-D. Wiemhöfer, W. Göpel, Electrode reactions of La<sub>0.8</sub>Sr<sub>0.2</sub>MnO<sub>3±δ</sub>-electrodes on stabilized zirconia with oxygen and the nitrogen oxides NO and NO<sub>2</sub>, *Ionics* 1 (1995) 32–39.
- [23] T. Hibino, Electrochemical removal of both NO and CH<sub>4</sub> under lean-burn conditions, *J. Appl. Electrochem.* 25 (1994) 203–207.
- [24] T. Hibino, K. Ushiki, Y. Kuwahara, M. Mizuno, A. Masegi, H. Iwahara, Medium-temperature electrolysis of NO and CH<sub>4</sub> under lean-burn conditions using yttria-stabilized zirconia as a solid electrolyte, *J. Chem. Soc. Faraday Trans.* 91 (13) (1995) 1955–1959.
- [25] T. Hibino, K. Ushiki, Y. Kuwahara, M. Mizuno, Electrochemical removal of NO in the presence of excess O<sub>2</sub>, H<sub>2</sub>O and CO<sub>2</sub> using Sm<sub>2</sub>O<sub>3</sub>-doped CeO<sub>2</sub> as a solid electrolyte, *Solid State Ionics* 89 (1996) 13–16.
- [26] T. Hibino, K. Ushiki, Y. Kuwahara, Mechanism of NO decomposition in a solid electrolyte reactor by SEP method, *Solid State Ionics* 98 (1997) 185–190.
- [27] E. Wachsman, P. Jayaweera, G. Krishnan, A. Sanjurjo, Electrocatalytic reduction of NO<sub>x</sub> on La<sub>1-x</sub>A<sub>x</sub>B<sub>1-y</sub>B'<sub>y</sub>O<sub>3-δ</sub>: evidence of electrically enhanced activity, *Solid State Ionics* 136-137 (2000) 775–782.
- [28] S. Bredikhin, K. Maeda, M. Awano, Electrochemical cell with two layer cathode for NO decomposition, *Ionics* 7 (2001) 109–115.

- [29] S. Bredikhin, K. Maeda, M. Awano, NO decomposition by an electrochemical cell with mixed oxide working electrode, *Solid State Ionics* 144 (2001) 1–9.
- [30] S. Bredikhin, K. Maeda, M. Awano, Peduliarity of NO decomposition by electrochemical cell with a mixed oxide working electrode, *J. Electrochem. Soc.* 148 (10) (2001) D133–D138.
- [31] S. Bredikhin, K. Matsuda, K. Maeda, M. Awano, Novel low voltage electrochemical cell for NO decomposition, *Solid State Ionics* 149 (2002) 327–333.
- [32] S. Bredikhin, K. Maeda, M. Awano, Low current density electrochemical cell for NO decomposition, *Solid State Ionics* 152–153 (2002) 727–733.
- [33] T. Hiramatsu, S. Bredikhin, S. Katayama, O. Shiono, K. Hamamoto, Y. Fujishiro, M. Awano, High selective deNO<sub>x</sub> electrochemical cell with self-assembled electro-catalytic electrode, *J. Electroceram.* 13 (2004) 865–870.
- [34] K. Iwayama, X. Wang, Selective decomposition of nitrogen monoxide to nitrogen in the presence of oxygen on RuO<sub>2</sub>/Ag(cathode) yttria-stabilized zirconia/Pd(anode), *Appl. Catal. B: Environ.* 19 (1998) 137–142.
- [35] X. Wang, Q. Zhao, T. Cai, Selective decomposition of NO in the presence of excess O<sub>2</sub> in electrochemical cells, *J. Appl. Electrochem.* 34 (2004) 945–952.
- [36] S. Park, H. Song, H. Choi, J. Moon, NO decomposition over the electrochemical cell of lanthanum stannate pyrochlore and YSZ composite electrode, *Solid State Ionics* 175 (2004) 625–629.
- [37] H. Song, J. Moon, H. Hwang, Electrochemical decomposition of NO over composite electrodes on YSZ electrolyte, *J. Eur. Ceram. Soc.* 26 (2005) 981–986.
- [38] K. K. Hansen, H. Christensen, E. Skou, Electrochemical reduction of NO and O<sub>2</sub> on oxide based electrodes, *Ionics* 6 (2000) 340–345.
- [39] K. K. Hansen, H. Christensen, E. Skou, S. Skaarup, Electrochemical reduction of NO and O<sub>2</sub> on Cu/CuO, *J. Appl. Electrochem.* 30 (2000) 193–200.
- [40] K. K. Hansen, E. Skou, H. Christensen, Perovskites as cathodes for nitric oxide reduction, *J. Electrochem. Soc.* 30 (2000) 193–200.
- [41] V. Simonsen, D. Find, M. Lilliedal, R. Petersen, K. K. Hansen, Spinel as cathodes for the electrochemical reduction of O<sub>2</sub> and NO, *Top. Catal.* 45 (2007) 143–148.
- [42] V. Simonsen, L. N. K. K. Hansen, Electrochemical reduction of NO and O<sub>2</sub> on La<sub>2–x</sub>Sr<sub>x</sub>CuO<sub>4</sub> based electrodes, *J. Solid State Electrochem.* 12 (2008) 1573–1577.
- [43] V. Simonsen, L. Nørskov, A. Hagen, K. K. Hansen, Electrochemical reduction of NO on La<sub>2–x</sub>Sr<sub>x</sub>NiO<sub>4</sub> based electrodes, *J. Solid State Electrochem.* 13 (2009) 1529–1534.

- [44] F. Bræstrup, K. Hansen, The  $\text{NiFe}_2\text{O}_4$  -  $\text{MgFe}_2\text{O}_4$  series as electrode materials for electrochemical reduction of  $\text{NO}_x$ , *J. Solid State Electrochem.* 13 (2009) 1241–1250.
- [45] F. Bræstrup, K. Hansen, Characterization of  $\text{MgMn}_x\text{Fe}_{2-x}\text{O}_4$  as a possible cathode material for electrochemical reduction of  $\text{NO}_x$ , *J. Appl. Electrochem.* 39 (2009) 2369–2374.
- [46] K. Hamamoto, Y. Fujishiro, M. Awano, Low-temperature  $\text{NO}_x$  decomposition using an electrochemical reactor, *J. Electrochem. Soc.* 155 (8) (2008) E109–E111.
- [47] P. Smeets, M. Groothaert, R. van Teeffelen, H. Leeman, E. Hensen, R. Schoonheydt, Direct NO and  $\text{N}_2\text{O}$  decomposition and NO-assisted  $\text{N}_2\text{O}$  decomposition over Cu-zeolites: Elucidating the influence of the Cu-Cu distance on oxygen migration, *J. Catal.* 245 (2007) 358–369.
- [48] E. Winter, The catalytic decomposition of nitric oxide by metallic oxides, *J. Catal.* 22 (1971) 158–170.
- [49] M. Haneda, Y. Kintaichi, N. Bion, H. Hamada, Alkali metal doped cobalt oxide catalysts for NO decomposition, *Appl. Catal. B: Environ.* 46 (2003) 473–482.
- [50] S. Xie, M. Rosynek, J. Lunsford, Catalytic reactions of NO over 0-7 mol% Ba/MgO catalysts, *J. Catal.* 188 (1999) 24–31.
- [51] L. Smart, E. Moore, *Solid state chemistry - an introduction*, 3rd Edition, Taylor & Francis, 2005, Ch. 1, p. 43.
- [52] M. Mogensen, D. Lybye, N. Bonanas, P. Hendriksen, F. Poulsen, Factors controlling the oxide ion conductivity of fluorite and perovskite structured oxides, *Solid State Ionics* 174 (2004) 279–286.
- [53] R. Voorhoeve, J. Remeika, J. D.W. Johnson, Rare-earth manganites: Catalysts with low ammonia yield in the reduction of nitrogen oxides, *Science* 180 (1973) 62–64.
- [54] S. Shin, H. Arakawa, Y. Hatakeyama, K. Ogawa, K. Shimomura, Absorption of NO in the lattice of an oxygen-deficient perovskite  $\text{SrFeO}_{3-x}$  and the infrared spectroscopic study of the system  $\text{NO}^{3-x}\text{-SrFeO}_{3-x}$ , *Mat. Res. Bull.* 14 (1979) 633–639.
- [55] Y. Teraoka, T. Harada, S. Kagawa, Reaction mechanism of direct decomposition of nitric oxide over Co- and Mn-based perovskite-type oxides, *J. Chem. Soc., Faraday Trans.* 94 (13) (1998) 1887–1891.
- [56] C. Tofan, D. Klvana, J. Kirchnerova, Direct decomposition of nitric oxide over perovskite-type catalysts part I. activity when no oxygen is added to the feed, *Appl. Catal. A.* 223 (2002) 275–286.

- [57] C. Tofan, D. Klvana, J. Kirchnerova, Direct decomposition of nitric oxide over perovskite-type catalysts part II. effect of oxygen in the feed on the activity of three selected compositions, *Appl. Catal. A.* 226 (2002) 225–240.
- [58] T. Ishihara, M. Ando, K. Sada, K. Takiishi, K. Yamada, H. Nishiguchi, Y. Takita, Direct decomposition of NO into N<sub>2</sub> and O<sub>2</sub> over La(Ba)Mn(In)O<sub>3</sub> perovskite oxide, *J. Catal.* 220 (2003) 104–114.
- [59] D. Fino, N. Russo, G. Saracco, V. Specchia, Catalytic removal of NO<sub>x</sub> and diesel soot over nanostructured spinel-type oxides, *J. Catal.* 242 (2006) 38–47.
- [60] F. Bræstrup, K. Hansen, NiCr<sub>x</sub>Fe<sub>2-x</sub>O<sub>4</sub> as cathode material for electrochemical reduction of NO<sub>x</sub>, *J. Solid State Electrochem.* 14 (2010) 157–166.
- [61] S. Iwamoto, R. Takahashi, M. Inoue, Direct decomposition of nitric oxide over Ba catalysts supported on CeO<sub>2</sub>-based mixed oxides, *Appl. Catal. B: Environ.* 70 (2007) 146–150.
- [62] V. Simonsen, M. Johnsen, K. K. Hansen, Influence of BaO in perovskite electrodes for the electrochemical reduction of NO<sub>x</sub>, *Top. Catal.* 45 (2007) 131–135.
- [63] L. Smart, E. Moore, *Solid state chemistry - an introduction*, Taylor & Francis.
- [64] R. Voorhoeve, J. Remeika, L. Tremble, A. Cooper, F. Disalvo, P. Gallagher, Perovskite-like La<sub>1-x</sub>K<sub>x</sub>MnO<sub>3</sub> and related compounds: solid state chemistry and the catalysis of the reduction of NO by CO and H<sub>2</sub>, *J. Solid State Chem.* 14 (1975) 395–406.
- [65] J. Zhu, D. Xiao, J. Li, X. Yang, Y. Wu, Effect of Ce on NO direct decomposition in the absence/presence of O<sub>2</sub> over La<sub>1-x</sub>Ce<sub>x</sub>SrNiO<sub>4</sub> (0 ≤ x ≤ 0.3), *J. Mol. Catal. A: Chem.* 234 (2005) 99–105.
- [66] M. Mogensen, N. Sammes, G. Tompsett, Physical, chemical and electrochemical properties of pure and doped ceria, *Solid State Ionics* 129 (2000) 63–94.
- [67] D. Fagg, I. Marozau, A. Shaula, V. Kharton, J. Frade, Oxygen permeability, thermal expansion and mixed conductivity of Gd<sub>x</sub>Ce<sub>0.8-x</sub>Pr<sub>0.2</sub>O<sub>2-δ</sub>, *Solid State Ionics* 116 (2006) 217–223.
- [68] M. Nauer, C. Ftikos, B. Steele, An evaluation of Ce-Pr oxides and ce-pr-nb oxides mixed conductors for cathodes of solid oxide fuel cells: structure, thermal expansion and electrical conductivity, *J. Eur. Ceram. Soc.* 14 (1994) 493–499.
- [69] T. Stefanik, H. Tuller, Ceria-based gas sensors, *J. Eur. Ceram. Soc.* 21 (2000) 1967–1970.
- [70] K. Krishna, A. Bueno-López, M. Makkee, J. Moulijn, Potential rare-earth modified CeO<sub>2</sub> catalysts for soot oxidation, *Top. Catal.* 42-43 (2007) 221–228.

- [71] K. K. Hansen, E. Skou, H. Christensen, T. Turek, Perovskites as catalysts for the selective catalytic reduction of nitric oxide with propene: Relationship between solid state properties and catalytic activity, *J. Catal.* 199 (2001) 132–140.
- [72] J. Ralph, C. Rossignol, R. Kumar, Cathode materials for reduced-temperature SOFCs, *J. Electrochem. Soc.* 150 (11) (2003) A1518–A1522.
- [73] A. Esquirol, N. Brandon, J. Kilner, M. Mogensen, Electrochemical characterization of  $\text{La}_{0.6}\text{Sr}_{0.4}\text{Co}_{0.2}\text{Fe}_{0.8}\text{O}_3$  cathodes for intermediate-temperature SOFCs, *J. Electrochem. Soc.* 151 (11) (2004) A1847–A1855.
- [74] Y. Teraoka, H. Zhang, K. Okamoto, N. Yamazoe, Mixed ionic-electronic conductivity of  $\text{La}_{1-x}\text{Sr}_x\text{Co}_y\text{Fe}_{1-y}\text{O}_{3-\delta}$  perovskite-type oxides, *Mat. Res. Bull.* 23 (1988) 51–58.
- [75] L. Tai, M. Nasrallah, H. Anderson, D. Sparlin, S. Sehlin, Structure and electrical properties of  $\text{La}_{1-x}\text{Sr}_x\text{Co}_y\text{Fe}_{1-y}\text{O}_3$ . Part 2. The system  $\text{La}_{1-x}\text{Sr}_x\text{Co}_{0.2}\text{Fe}_{0.8}\text{O}_3$ , *Solid State Ionics* 76 (1995) 273–283.
- [76] H. Hwang, J. Moon, J. Moon, Removal of nitric oxide NO by perovskite-type composite catalytic thick films,  $\text{La}_{0.6}\text{Sr}_{0.4}\text{Co}_{0.2}\text{Fe}_{0.8}\text{O}_{3-\delta}$  and gadolinia-doped ceria electrolyte,  $\text{Gd}_{0.2}\text{Ce}_{0.8}\text{O}_{2-\delta}$ , *J. Am. Ceram. Soc.* 88 (1) (2005) 79–84.
- [77] J. Fleig, Solid oxide fuel cells cathodes: Polarization mechanisms and modeling of the electrochemical performance, *Annu. Rev. Mater. Res.* 33 (2003) 361–382.
- [78] L. Smart, E. Moore, Solid state chemistry - an introduction, 3rd Edition, Taylor & Francis, 2005, Ch. 2.
- [79] E. Barsoukov, J. MacDonald, Impedance spectroscopy - Theory, Experimental and Applications, 2nd Edition, Wiley Interscience, New York, 2005.
- [80] L. Chick, L. Pederson, G. Maupin, J. Bates, L. Thomas, G. Exarhos, Glycine-nitrate combustion synthesis of oxide ceramic powders, *Mater. Lett.* 10 (1,2) (1990) 6–12.
- [81] A. Hagen, K. Schueler, F. Roessner, The performance of the Ti-MCM-41 in aqueous media and after mechanical treatment studied by in situ xanes, uv/vis and test reactions, *Micropor. Mesopor. Mater.* 51 (2002) 23–33.
- [82] P. Fabry, M. Kleitz, Influence of the metal and the electrolyte composition on the characteristics of the oxygen electrode reaction on solid oxide electrolyte, *Electroanal. Chem. Interfac. Electrochem.* 57 (1974) 165–177.
- [83] J. Newman, Resistance for flow of current to a disk, *J. Electrochem. Soc.* 113 (1966) 501–502.



- [84] J. Winkler, P. Hendriksen, N. Bonanos, M. Mogensen, Geometric requirements of solid electrolyte cells with a reference electrode, *J. Electrochem. Soc.* 145 (4) (1998) 1184–1192.
- [85] Z. He, K. Andersen, L. Keel, F. Nygaard, M. Menon, K. Hansen, Processing and characterization of porous electrochemical cells for flue gas purification, *Ionics* 15 (2008) 427–431.
- [86] B. Ravel, M. Newville, ATHENA, ARTEMIS, HEPHAESTUS: Data analysis for X-ray absorption spectroscopy using IFEFFIT, *J. Synchrotron Rad.* 12 (4) (2005) 537–541.
- [87] L. Woo, L. Martin, R. Glass, R. Gorte, Impedance characterization of a model Au/Yttria-stabilized zirconia/Au electrochemical cell in varying oxygen and  $\text{NO}_x$  concentrations, *J. Electrochem. Soc.* 154 (4) (2007) J129–J135.
- [88] M. Stranzenbach, B. Saruhan, Equivalent circuit analysis on  $\text{NO}_x$  impedance-metric gas sensors, *Sens. Actuators B: Chem.* 137 (2009) 154–163.
- [89] T. Hibino, Y. Kuwahara, T. Otsuka, N. Ishida, T. Oshima,  $\text{NO}_x$  detection using the electrolysis of water vapour in a YSZ cell Part I.  $\text{NO}_x$  detection, *Solid State Ionics* 107 (1998) 213–216.
- [90] T. Hibino, Y. Kuwahara, T. Otsuka, N. Ishida, T. Oshima,  $\text{NO}_x$  detection using the electrolysis of water vapour in a YSZ cell Part II. Electrochemical oxygen pump, *Solid State Ionics* 107 (1998) 217–220.
- [91] T. Jacobsen, B. Zachau-Christensen, L. Bay, S. Skaarup, *Proc. 17th risø int. symp. on materials science*, no. 17, Risø National Laboratory, Roskilde, Denmark, 1996, p. 29.
- [92] B. Boukamp, A nonlinear least squares fit procedure for analysis of immitance data of electrochemical systems, *Solid State Ionics* 20 (1986) 31–44.
- [93] M. Jørgensen, M. Mogensen, Impedance of solid oxide fuel cell lsm/ysz composite cathodes, *J. Electrochem. Soc.* 148 (5) (2001) A433–A442.
- [94] S. Primdahl, M. Mogensen, Gas conversion impedance: A test geometry effect in characterization of solid oxide fuel cell anodes, *J. Electrochem. Soc.* 145 (7) (1998) 2431–2438.
- [95] P. Kofstad, *Uorganisk Kjemi*, 2nd Edition, Tano, Oslo, 1987.
- [96] J. Mizusaki, Y. Yonemura, H. Kamata, K. Ohyama, N. Mori, H. Takai, H. Tagawa, M. Dokiya, K. Naraya, T. Sasamoto, H. Inaba, T. Hashimoto, Electronic conductivity, seebeck coefficient, defect and electronic structure of nonstoichiometric  $\text{La}_{1-x}\text{Sr}_x\text{MnO}_3$ , *Solid State Ionics* 132 (2000) 167–180.
- [97] C. Clausen, C. Bagger, J. Bilde-Sørensen, A. Horsewell, Microstructural and microchemical characterization of the interface between  $\text{La}_{0.85}\text{Sr}_{0.15}\text{MnO}_3$  and  $\text{Y}_2\text{O}_3$ -stabilized  $\text{ZrO}_2$ , *Solid State Ionics* 70/71 (1994) 59–64.

- [98] R. Werchmeister, K. Hansen, M. Mogensen, Characterisation of  $\text{La}_{1-x}\text{Sr}_x\text{MnO}_3$  and doped ceria composite electrodes in  $\text{NO}_x$  containing atmosphere with impedance spectroscopy, *J. Electrochem. Soc.* 157 (5) (2010) P35–P45.
- [99] R. Werchmeister, K. Hansen, M. Mogensen, Electrochemical testing of composite electrodes of  $\text{La}_{1-x}\text{Sr}_x\text{MnO}_3$  and doped ceria in NO containing atmosphere, in preparation.
- [100] M. Søgaaard, T. Sholklapper, M. Wandel, L. D. Jonghe, M. Mogensen, Infiltration of SOFC cathodes, in: *Proceedings (on CD-ROM)*, no. 8, European solid oxide fuel cell forum, European solid oxide fuel cell forum, Lucerne, 2008.
- [101] M. Mogensen, M. Søgaaard, P. Blennow, K. Hansen, The action of nanoparticles in SOFC electrodes, in: *Proceedings (on CD-ROM)*. 8. European solid oxide fuel cell forum, no. 8, European solid oxide fuel cell forum, Lucerne, 2008.